



**Observation of Diffractive Bottom Quark
Production
in 1.8-TeV Proton-Antiproton Collisions**

Hirofumi IKEDA

A dissertation submitted to the Doctoral Program
in Physics, the University of Tsukuba
in partial fulfillment of the requirements for the
degree of Doctor of Philosophy (Science)

January, 1999

Abstract

The bottom quark production in the single diffractive dissociation is first observed in $p\bar{p}$ collisions at $\sqrt{s}=1.8$ TeV using the Collider Detector at Fermilab. The absence of an energy flow in the forward rapidity region ('rapidity gap') is used as an evidence of the single diffraction. The high- p_T electron in the E_T range of $9.5 < E_T^{ele} < 20$ GeV and the central rapidity region ($|\eta| < 1.1$) are used to identify the bottom quark decay. The ratio of the diffractive to the non-diffractive bottom quark production is obtained using the model dependent acceptance of the rapidity gap signal for the four kinds of the pomeron model. The ratio $R_{b\bar{b}}$ is measured to be;

$$R_{b\bar{b}}(\xi < 0.1; \text{FG}) = 0.62 \pm 0.19(\text{stat}) \pm 0.14(\text{syst})\%$$

for the flat-gluon pomeron model,

$$R_{b\bar{b}}(\xi < 0.1; \text{FQ}) = 0.93 \pm 0.29(\text{stat}) \pm 0.22(\text{syst})\%$$

for the flat-quark pomeron model,

$$R_{b\bar{b}}(\xi < 0.1; \text{HG}) = 0.71 \pm 0.22(\text{stat}) \pm 0.16(\text{syst})\%$$

for the hard-gluon pomeron model,

$$R_{b\bar{b}}(\xi < 0.1; \text{HQ}) = 1.18 \pm 0.36(\text{stat}) \pm 0.27(\text{syst})\%$$

for the hard-quark pomeron model.

This measured ratio is compared with the results of the diffractive W and the diffractive dijet productions. The ratios measured in these three processes are consistent with each other and significantly lower than the theoretical prediction.

Acknowledgments

I wish to express my deepest gratitude to my research advisor, Professor Shinghong Kim, who continuously encouraged me throughout my graduate years. His guidance in every critical points lead me to the right direction. My special thanks are also due to Professor Kunitaka Kondo for his introduction to the topic of the hard diffraction, especially to the Roman-Pot experiment. It was a beneficial and a unique experience for me to participate in such an independent experiment from the very beginning to the end of the operation.

I am deeply indebted to Dr. Kiyoshi Yasuoka for his patient guidance and helpful discussions from the early stages of my physics analysis. I am also grateful to Professor Mike Albrow for his constant encouragement and patience. He was so kind to take his time for my education. I would like to thank the Rockefeller University group; Professor Dino Goulianos, Dr. Philip Melese, Dr. Anwer Bhatti, Dr. Alexander Akopian, Dr. Suren Bagdasarov and Dr. Kerstin Borrás for their help and useful discussion. I could not finish my thesis without using their pioneered techniques to analyze the single diffraction events observed in the CDF. I also wish to thank to Dr. Fumihiko Ukegawa and Dr. Junichi Suzuki for their valuable advice on the analysis of the b -quark identification.

Although I did not use the data of the Roman Pot experiment in my thesis, I would like to express my gratitude here to all the people who were involved in the experiment. I am grateful to Professor Junsuke Iwai for his leadership and the hard work during the installation process of the Roman-Pot. Without his enthusiasm and deep insights on the experimental physics, the installation was impossible. I also thank my collaborators from Japan: Mr. Housai Nakada, Dr. Tesuo Arisawa, Mr. Koji Terashi, Mr. Shin Uesaka, Mr. Yasuhiro Yoda and Mr. Kenichi Hatakeyama for their hard work, helpful

discussions on the particle physics and their friendship. I am deeply indebted to Dr. Craig Moore and many people in the Fermilab Accelerator Division for their professional help.

I owe thanks to all staffs of Univ. of Tsukuba; Professors Koji Takikawa, Shigeyuki Miyashita, Itsuo Nakano, Dr. Yoshihiro Seiya, Dr. Kazuhiko Hara for their support and helpful comments. It was good opportunity for me to share good time with so many friends from University of Tsukuba, Osaka-City University, Hiroshima University and Geneve University during my stay at Fermilab. In particular, I thank to my fellow graduate students Dr. Shin Aota and Mr. Hiroyoki Minato for their friendship and kindness. Mrs. Kyoko Kunori, Dr. Shuichi Kunori, Dr. Nobuaki Oshima and Mrs. Kiyoko Oshima also made my life enjoyable. I also thanks to Mrs. Mutsumi Uenishi and Mrs. Kazuko Kumashiro for their secretary work in Japan.

Finally I thank my family for their endless support and encouragements.

This work was supported by the Ministry of Education, Science and Culture of Japan; the U.S. Department of Energy and National Science Foundation; the Italian Istituto Nazionale di Fisica Nucleare; the Natural Sciences and Engineering Research Council of Canada; the National Science Council of the Republic of China; and the A.P.Sloan Foundation.

Contents

Chapter 1	Introduction	6
1.1	Kinematics of the single diffraction	9
1.2	Single diffraction in the Regge pole picture	12
1.3	Diffractive $b\bar{b}$ production	14
1.4	Outline of analysis procedure	15
Chapter 2	The CDF detector	16
2.1	Coordinate system	16
2.2	Tracking detectors	20
2.3	Calorimeters	24
2.4	Central Preshower chamber: CPR	29
2.5	Beam-Beam Counter: BBC	29
2.6	Trigger	31
Chapter 3	Event selection	34
3.1	$b\bar{b}$ candidate selection	34
3.1.1	Central electron trigger	34
3.1.2	Electron identification	35
3.1.3	Additional requirements	38
3.2	Diffractive candidate selection: Rapidity gap tagging	42
Chapter 4	Background from non-heavy flavors	49
4.1	Hadrons faking electrons	49

4.1.1	Control sample for CPR templates	50
4.1.2	Results of CPR fit	51
4.2	Photon conversion electrons	51
4.2.1	Conversion finding efficiency	55
4.2.2	Residual conversions	57
Chapter 5	Determination of $b\bar{b}$ event fraction	64
5.1	Control samples for p_T^{rel} and impact parameter fit	64
5.2	Results of p_T^{rel} fit	67
5.3	Results of impact parameter fit	73
5.4	Combined results	80
Chapter 6	Ratio of the diffractive to the non-diffractive $b\bar{b}$ production	83
6.1	Acceptance for the rapidity gap tagging	83
6.1.1	Acceptance for single interaction events	83
6.1.2	Lifetime efficiency of the BBC and the forward calorimeter	84
6.1.3	Gap acceptance for diffractive events	85
6.2	Ratio of the diffractive to the non-diffractive $b\bar{b}$ production . .	88
6.3	Systematic uncertainties	92
Chapter 7	Comparison with the theoretical prediction	95
Chapter 8	Conclusion	100
Appendix A	Regge pole phenomenology	102
A.1	Regge pole	102
A.2	Pomeron	105
Appendix B	CPR charge correction	108

Appendix C	Simulation of the forward calorimeter	115
Appendix D	Likelihood function	122
D.1	Likelihood function for binned fit	122
D.2	Likelihood function for unbinned fit	123
Appendix E	The CDF Collaboration	125

Chapter 1

Introduction

Quantum Chromodynamics (QCD) is widely accepted as a fundamental theory which describes the strong interactions because of its remarkable success in the high precision tests of the high energy experiments. Although we believe QCD is the fundamental theory, it is difficult to study a scattering process with a small momentum transfer in the framework of the QCD since the renormalized coupling constant is not small enough in such a low energy scale to use a perturbative technique.

The single diffractive dissociation [1] (or single diffraction) is one of such processes that we cannot fully describe in the framework of QCD. The single diffraction is experimentally defined as a process where one of the two oppositely incoming hadrons keeps its quantum numbers unchanged after the collision. This leading hadron usually go off in the beam pipe without decreasing its initial momentum. In the view point of the quantum field theory, any process should be explained by the exchange of field(s) between the two hadrons. The exchanged field(s) in the single diffraction should not carry a color in total so as to keep the hadrons as a color singlet. This exchanged color-less object is a *pomeron* named in the old *Regge pole phenomenology* [2, 3].

The Regge pole phenomenology is based on the observed hadron spectroscopy and some general postulates such as the unitarity and the analytic-

ity of the S -matrix. The validity of the Regge pole phenomenology is limited in the soft (small momentum transfer) process. In the Regge picture, a scattering process is described as an exchange of “pole”, which lives in the complex angular momentum space. The pomeron is introduced as one of such poles which give a dominant contribution to soft collisions of hadrons with high energy. At least in the soft process, pomeron behaves as if it is a virtual particle state although it has not been observed in the hadron spectroscopy. The Regge pole phenomenology is briefly described in Appendix A.

The uniqueness of the *hard* single diffraction is an existence of the two different scales in a single interaction. Regarding to the leading hadron, a momentum transfer via the pomeron is too small to use the perturbative QCD but it is small enough to use the Regge pole picture. On the other hand, the interaction between the constitutions of the pomeron and the dissociating hadron take place in a hard scale where we could use the perturbative QCD. It is thus possible to probe the “contents” of the pomeron by studying the hard single diffraction using a combination of the Regge phenomenology and the perturbative QCD. The pomeron is treated as an effective particle state in the above picture called Ingelman-Schlein model (IS model) [4].

Experimental study of the partonic nature of the pomeron was pioneered by UA8 experiments [5, 6] by observing dijet production in the single diffraction events at CERN $S\bar{p}pS$ collider operated at $\sqrt{s}=630$ GeV. They reported that the pomeron exhibits a “hard structure” like $zf(z) \sim 1 - z$ basically, where z is a parton momentum fraction in the pomeron. More recently, both ZEUS and H1 collaboration measured the structure function of the pomeron by the deep inelastic scattering experiment at the HERA e - p collider. The measured pomeron structure function is mostly “flat” like $zf_{q,g/\mathbb{P}}(z) \sim 1$ and depends on Q^2 slightly. The H1 [7] performed a NLO QCD fit for the observed pomeron structure function at different Q^2 scales

and concluded approximately 90%(80%) of the momentum is carried by gluons at $Q^2=4.5\text{GeV}^2(75\text{ GeV}^2)$ under such model. The ZEUS [8] measured both the pomeron structure function and the differential cross section of the diffractive dijet photoproduction. They also reported that a substantial part of the pomeron momentum is carried by gluons if the pomeron is assumed to have a hadron-like partonic structure in the form of parton densities which evolve according to the DGLAP equations [9].

At the Tevatron collider, the dijet production [10] and the W -boson production [11] were observed in the diffractive $p\bar{p}$ scattering at $\sqrt{s}=1800\text{ GeV}$. The combined analysis of the diffractive dijet and the diffractive W productions support a dominantly gluonic picture of the pomeron. The measured rates of these processes show significantly lower values than the IS model prediction with the Donnachie-Landshoff flux (see Sec. 1.2). This result suggest that there is a problem in the hypothesis of the factorization of the pomeron flux at the Tevatron energy although the hypothesis successfully described the data at the HERA [42].

The study of the diffractive heavy flavor production can also allow us to test the IS model [12]. The diffractive heavy flavor production rate is sensitive to the contribution of the gluon in the pomeron because the heavy flavors are mainly produced through a gluon-gluon fusion. The experimental study of the diffractive heavy flavor production was first reported by the UA1 collaboration at CERN $Spp\bar{p}S$ collider [13]. They searched for the diffractively produced μ +jet events and estimated the heavy flavor contribution in the data by subtracting non-heavy flavor backgrounds. Assuming the hard structure function to the pomeron they found an upper limit of the diffractive $b\bar{b}$ production cross section $\sigma_{b\bar{b}}(p_T > 8\text{GeV}) < 50\text{ nb}$ (95% C.L.) at $\sqrt{s}=630\text{ GeV}$.

In this thesis we present the first observation of the diffractive bottom

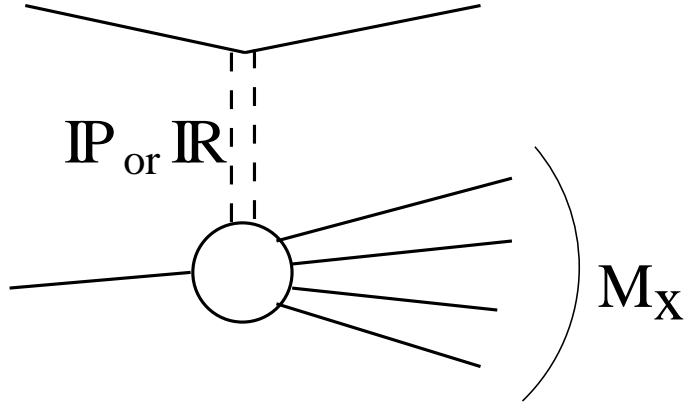


Figure 1.1: Single diffraction.

quark (b -quark) production in $p\bar{p}$ collisions at $\sqrt{s}=1.8$ TeV using the Collider Detector at Fermilab (CDF). The production of the b -quark is identified with both the large transverse momentum of the decaying electron relative to the associating jet axis and the large impact parameter of the electron track. The ratio of the diffractive b -quark production to the non-diffractive b -quark production is measured. The ratio is compared to the theoretical prediction of the Ingelman-Schlein model using the Donnachie-Landshoff flux.

1.1 Kinematics of the single diffraction

The single diffraction dissociation process, $p + \bar{p} \rightarrow p + X$ is schematically shown in Fig. 1.1. Some kinematical variables are frequently used to describe the single diffraction process. Using the four momentum of the initial beam particles ($P^{pin}, P^{\bar{pin}}$) and the final systems, (P^{pout}, P^X), the following three independent variables are defined;

$$s \equiv (P^{pin} + P^{\bar{pin}})^2 = (P^{pout} + P^X)^2 \quad (1.1)$$

$$t \equiv (P^{pout} - P^{pin})^2 = (P^X - P^{\bar{pin}})^2 \quad (1.2)$$

$$M_X \equiv (P^X)^2 = (P^{pin} + P^{\bar{pin}} - P^{pout})^2 \quad (1.3)$$

where s is a center of mass energy, t is a momentum transfer and M_X is a mass of diffractive system X . Equation 1.2 can be expressed by the energy of the system X (E_X),

$$\begin{aligned} s &= (P^{p\text{out}} + P^X)^2 \\ &= P^X \cdot (P^{p\text{out}} + P^X) + P^{p\text{out}} \cdot (P^{p\text{out}} + P^X) \\ &= E_X \sqrt{s} + \frac{1}{2}(s - M_X^2 + m_p^2), \end{aligned}$$

where m_p is the mass of the proton. This formulae yields the following expression for the energy of the system X ,

$$E_X = \frac{s + M_X^2 - m_p^2}{2\sqrt{s}}. \quad (1.4)$$

The 3-momentum of the leading proton $\vec{P}^{p\text{out}}$ can be expressed with s and M_X using Eq. 1.4,

$$\begin{aligned} \left| \vec{P}^{p\text{out}} \right|^2 &= \left| \vec{P}^X \right|^2 \\ &= E_X^2 - M_X^2 \\ &= \frac{[s - (m_p + M_X)^2][s - (m_p - M_X)^2]}{4s} \\ &\xrightarrow{s, M_X \gg m_p} \frac{(s - M_X^2)^2}{4s} \\ \therefore \left| \vec{P}^{p\text{out}} \right| &\approx \frac{s - M_X^2}{2\sqrt{s}} \end{aligned} \quad (1.5)$$

Now we introduce the another frequently used variable, the Feynman variable x_F ,

$$x_F = \frac{P_z^{p\text{out}}}{P_z^{p\text{in}}}. \quad (1.6)$$

Since $P_z^{p\text{out}} \approx \left| \vec{P}^{p\text{out}} \right|$, we arrive at,

$$x_F \approx \frac{\left| \vec{P}^{p\text{out}} \right|}{P_z^{p\text{in}}} = \frac{2 \left| \vec{P}^{p\text{out}} \right|}{\sqrt{s}} \approx 1 - \frac{M_X^2}{s}. \quad (1.7)$$

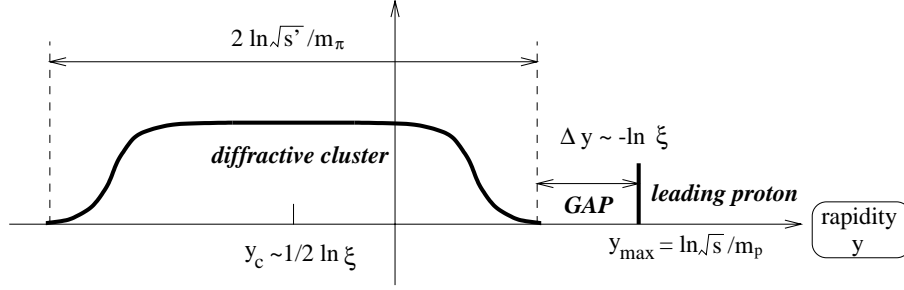


Figure 1.2: The kinematics of the single diffraction.

Instead of the x_F , the ξ variable is also used frequently,

$$\xi = \frac{M_X^2}{s} = 1 - x_F. \quad (1.8)$$

The rapidity distribution of the final states is schematically shown in Fig. 1.2. In the general $p\bar{p}$ collisions, the maximum rapidity bound of the generated particle is calculated from the definition,

$$\begin{aligned} y_{max} &= \frac{1}{2} \ln \frac{E + p_Z}{E - p_Z} \Big|_{max} = \frac{1}{2} \ln \frac{(E + p_Z)^2}{E^2 - p_Z^2} \Big|_{max} \\ &\approx \frac{1}{2} \ln \frac{(2E_{beam})^2}{m_p^2} = \ln \frac{\sqrt{s}}{m_p} \end{aligned} \quad (1.9)$$

Thus the rapidity of the leading proton is $\ln \sqrt{s}/m_p$. The width of the diffractive system X can be calculated by using Eq. 1.9 at the center of mass frame of the system X ,

$$y_{width}^X \approx 2 \ln \frac{\sqrt{s'}}{m_\pi} = 2 \ln \frac{M_X}{m_\pi} \quad (1.10)$$

The center of the rapidity for the diffractive system X is similarly obtained using Eqs. 1.4 and 1.5,

$$\begin{aligned} y_c^X &\approx -\frac{1}{2} \ln \frac{(E_X + |\vec{P}^X|)^2}{M_X^2} \approx -\frac{1}{2} \ln \frac{s^2}{s M_X^2} \\ &= -\frac{1}{2} \ln \frac{1}{\xi} \end{aligned} \quad (1.11)$$

Thus, the size of the rapidity gap between the cluster and the leading proton is obtained using Eq. 1.8,

$$\begin{aligned}
\Delta y &= y_{max}^p - y_c^X - \frac{1}{2} y_{width}^X \\
&\approx \ln \frac{\sqrt{s}}{m_p} + \frac{1}{2} \ln \frac{1}{\xi} - \ln \frac{M_X}{m_\pi} \\
&= \ln \left(\frac{\sqrt{s}}{M_X} \frac{1}{\sqrt{\xi}} \frac{m_p}{m_\pi} \right) \\
&= - \ln \left(\xi \frac{m_\pi}{m_p} \right). \tag{1.12}
\end{aligned}$$

The signature of the single diffraction is characterized with this forward rapidity gap.

1.2 Single diffraction in the Regge pole picture

A detailed analysis of the Regge pole phenomenology shows that the total cross section and the differential elastic cross section can be *factorized* into the Pomeron-hadron couplings and the universal contribution from the Pomeron exchange,

$$\sigma_T^{p\bar{p}} = \beta_{\mathbb{P}}^{pp}(0) \beta_{\mathbb{P}}^{\bar{p}\bar{p}}(0) \left(\frac{s}{s_0} \right)^{[\alpha_{\mathbb{P}}(0)-1]} \tag{1.13}$$

$$\frac{d\sigma_{el}^{p\bar{p}}}{dt} = \frac{1}{16\pi} [\beta_{\mathbb{P}}^{pp}(t) \beta_{\mathbb{P}}^{\bar{p}\bar{p}}(t)]^2 \left(\frac{s}{s_0} \right)^{2[\alpha_{\mathbb{P}}(t)-1]} \tag{1.14}$$

where $\beta_{\mathbb{P}}^{pp}(\beta_{\mathbb{P}}^{\bar{p}\bar{p}})$ is a coupling of the pomeron to the proton(anti-proton) and the s_0 is a scale parameter introduced for dimensional convenience. The single diffraction dissociation can also be described in the framework of the Regge pole phenomenology using the triple Regge diagram. In the particular range of the kinematical region ($\xi \equiv M^2/s < 0.1$ [1]), the contribution from the pomeron exchange is dominant.

$$\frac{d\sigma_{sd}^{p\bar{p}}}{dt d\xi} = \frac{1}{16\pi} \beta_{\mathbb{P}}^{pp}(t)^2 \xi^{1-2\alpha_{\mathbb{P}}(t)} \left[\beta_{\mathbb{P}}^{\bar{p}\bar{p}}(0) g(t) \left(\frac{s'}{s'_0} \right)^{\alpha_{\mathbb{P}}(0)-1} \right] \tag{1.15}$$

where $g(t)$ is a triple-pomeron coupling, $s' \equiv M^2$ is the square of the mass of the dissociating system, ξ is the fractional momentum of the pomeron carrying to the proton and s'_0 is the energy scale parameter. The triple-pomeron coupling $g(t)$ is experimentally found not to depend on t [1], thus $g(t) = g(0)$. The term in the brackets in Eq.1.15 can be identified as the pomeron-proton total cross section σ_T^{pP} in analogy with Eq.1.14. Then Eq.1.15 is expressed as,

$$\frac{d\sigma_{sd}^{p\bar{p}}}{dt d\xi} = f_{\mathbb{P}/p}(\xi, t) \sigma_T^{pP}(s') \quad (1.16)$$

where $f_{\mathbb{P}/p}(\xi, t)$ is called the *flux factor* of the pomeron and $\sigma_T^{pP}(s')$ is the total cross section of the pomeron-proton scattering. The pomeron flux factor is defined as

$$f_{\mathbb{P}/p}(\xi, t) \equiv \frac{1}{16\pi} \beta_{\mathbb{P}}^{pp}(t)^2 \xi^{1-2\alpha_{\mathbb{P}}(t)} \quad (1.17)$$

$$\equiv \frac{1}{16\pi} \{\beta_{\mathbb{P}}^{pp}(0) F(t)\}^2 \xi^{1-2\alpha_{\mathbb{P}}(t)}, \quad (1.18)$$

where the t dependence of the $\beta_{\mathbb{P}}^{pp}$ is replaced by the proton form factor $F(t)$ probed with the pomeron. The form factor $F(t)$ cannot be determined by the Regge theory. A hypothesis that a pomeron mainly couples to the quark in the hadron like a photon can reproduce the data well [14]. This hypothesis results in that the $F(t)$ is proportional to the electromagnetic-like form factor,

$$F_1(t) = \frac{4m_p^2 - 2.8t}{4m_p^2 - t} \left(\frac{1}{1 - t/0.71} \right)^2 \quad (1.19)$$

where m_p is a mass of the proton. The flux factor using this hypothesis is called Donnachie-Landshoff flux and is expressed as,

$$f_{\mathbb{P}/p}(\xi, t) = \frac{9}{4\pi^2} \beta_0^2 F_1(t)^2 \xi^{1-2\alpha_{\mathbb{P}}(t)} \quad (1.20)$$

where $\beta_0^2 = 3.202 \text{ GeV}^{-2}$ is the effective pomeron-quark coupling.

1.3 Diffractive $b\bar{b}$ production

The factorization property of the pomeron is supported by the elastic and the diffractive scattering experiments and implies that a pomeron can be treated as an ordinary particle virtually emitted from a hadron. Ingelman and Schlein proposed to extend the formalism obtained in the soft diffraction into the region of the hard diffractive scattering [4]. According to their idea, we describe our model used to calculate the diffractive $b\bar{b}$ production cross section in the thesis. Assuming that the factorization property is kept in this scale, the cross section of the diffractive $b\bar{b}$ production can be expressed as,

$$\frac{d\sigma(p\bar{p} \rightarrow p + b\bar{b}X)}{dt d\xi dp_T^2} = f_{\mathbb{P}/p}(\xi, t) \frac{d\sigma(\bar{p}\mathbb{P} \rightarrow b\bar{b}X)}{dp_T^2}, \quad (1.21)$$

where,

$$\frac{d\sigma(\bar{p}\mathbb{P} \rightarrow b\bar{b}X)}{dp_T^2} = \sum_{i,j} \int dx_1 f_{a_i/\bar{p}}(x_1, p_T^2) \int dx_2 f_{b_j/\mathbb{P}}(x_2, p_T^2) \frac{d\sigma(a_i b_j \rightarrow b\bar{b}X')}{dp_T^2}, \quad (1.22)$$

and the p_T is the transverse momentum of the b -quarks. The $f_{a_i/\bar{p}}(x_1, p_T^2)$ and the $f_{b_j/\mathbb{P}}(x_2, p_T^2)$ are the structure function for anti-proton and pomeron, respectively. The sum is performed over all parton types. As stated in the previous section, the pomeron flux factor $f_{\mathbb{P}/p}(\xi, t)$ is not uniquely defined by the Regge phenomenology. We used the Donnachie-Landshoff flux (Eq.1.20) to calculate the theoretical prediction. (Ingelman and Schlein used a different flux parameterization in their original analysis [4].)

The pomeron structure function $f_{b_j/\mathbb{P}}(x_2, p_T^2)$ was recently measured by H1 [7] and ZEUS [8] using deep inelastic scattering processes. The extracted parton distribution turned out to be nearly flat. According to this result, we used a simple model for a pomeron structure function expressed as;

$$z f_{g,q/\mathbb{P}}(z) \sim 1. \quad (1.23)$$

Another frequently used structure function is a hard structure function,

$$z f_{g,q/\mathbb{P}}(z) \sim z(1-z) \quad (1.24)$$

which is derived from the assumption that two partons share the pomeron momentum. We also used the hard structure function in the analysis.

1.4 Outline of analysis procedure

One of the characteristic signature of the single diffraction is an absence of a beam jet in one side of the forward rapidity region where particles are usually observed in the non-diffractive $p\bar{p}$ collisions. This signature is owing to the color-less nature of the exchanged object and is called the forward *rapidity gap*. In order to tag the rapidity gap events, we used two forward detectors, the forward calorimeters and the BBC which partially overlap with each other. The rapidity gap signal in the single diffraction is sometimes killed because particles generated from the dissociating system give the signal in the detector. We have corrected this rate of inefficiency using results of the Monte Carlo study.

The b -quark production candidates are tagged using an electron in the central rapidity region. We select events with such an electron to make up an electron sample. The impact parameter distribution and the transverse momentum spectrum relative to the jet axis are used to estimate the $b\bar{b}$ event fraction in the electron sample. The diffractive b -quark production candidates are selected from the electron sample using the rapidity gap signal. The fraction of b -quark events are individually estimated for both diffractive and non-diffractive sample. After correcting the efficiency and acceptance for the rapidity gap tagging, the ratio of the diffractive to the non-diffractive b -quark production is measured. The results are finally compared to the theoretical prediction.

Chapter 2

The CDF detector

This study is performed using the data collected by the Collider Detector at Fermilab (CDF) during 1994–1995 (RUN1B). The CDF is a multi-purpose detector built at the B0 collision point of the Tevatron Collider which gives a head-on collision of the proton and the anti-proton with the center of mass energy of 1800 GeV. Figure 2.1 shows a schematic view of the CDF. The main component of the CDF detector is categorized into two sub-systems, a tracking system (SVX,VTX,CTC and the superconducting solenoidal magnet) and a calorimeter system (Forward,Plug,Wall,Central). Each of those sub-systems is arranged to be symmetric in the cylindrical direction. In this chapter each sub-system of the CDF detector is briefly described with emphasis on what we used in our analysis. The full description of the CDF detector is found in the reference [15].

2.1 Coordinate system

Overall CDF coordinate $(x, y, z, r, \phi, \theta)$

We describe the coordinate system and the notation used in the thesis. Figure 2.2 shows the overall CDF coordinate system. In the CDF coordinate system, the origin is at the center of the central tracking chamber (CTC). The beam axis is taken as the z axis and positive in the proton direction.

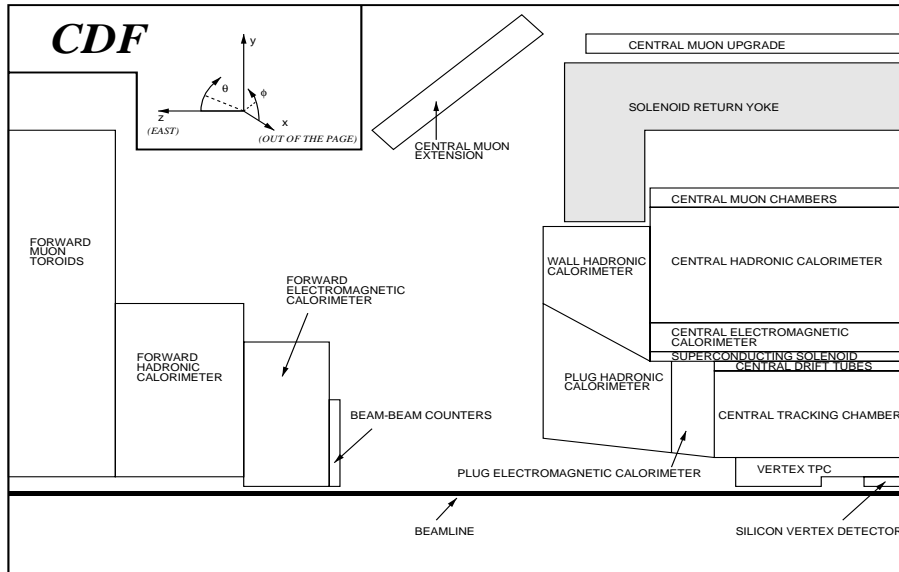


Figure 2.1: A quarter view of the CDF detector.

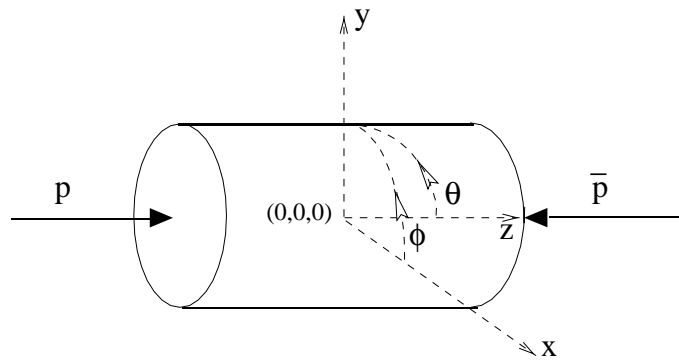


Figure 2.2: The CDF coordinate system.

The y axis is vertical and positive in upward. The x axis is horizontal and the direction is defined by the right-handed coordinate system.

The cylindrical coordinate system is also used. The r indicates the radial distance from the z -axis. The azimuthal angle about z -axis is represented by the ϕ , and defined 0 at x -axis. The polar angle relative to z -axis is represented by the θ , and defined 0 at z -axis.

Track parameterization $(\cot \theta, C, z_0, d, \phi_0)$

The CDF has a solenoidal magnet which functions as a spectrometer magnet in the central region of the CDF. Under this magnetic field, a trajectory of charged particle become a helix, the axis of which is parallel to the magnetic field. At the CDF the following 5 parameters are used to describe the helix of a track [16]:

$$\vec{\alpha} = (\cot \theta, C, z_0, d, \phi_0)$$

where:

- $\cot \theta$: cotangent of the polar angle at minimum approach.
- C : half curvature
- z_0 : z position at point of minimum approach to origin of helix.
- d : signed impact parameter distance between helix and origin at minimum approach.
- ϕ_0 : azimuthal angle of track at point of minimum approach.

Pseudorapidity (η) , **Transverse energy** (E_T)

In a hadron-hadron collision, interacting system is variously boosted along z -direction in event by event. It is thus convenient to use an invariant form under Lorentz boost to describe the physical quantity, such as a cross section. Consider the invariant volume element in the momentum space,

$$\frac{dp_x dp_y dp_z}{E}$$

This form is invariant to any Lorentz transformation. Since the CDF is a symmetric detector in ϕ direction, this form can be transformed into the following expression in the cylindrical coordinate,

$$\frac{\pi p_T dp_T dp_z}{E}.$$

where p_T is defined as $p_T \equiv p \sin \theta$. Against the Lorentz boost along the z -direction, p_T and dp_T are obviously invariant. Since the overall expression is an invariant form, the rest term, dp_z/E is an invariant quantity for z -boost. It is thus useful to introduce the new variable y by the following differential equation,

$$dy \equiv \frac{dp_z}{E} = \frac{dp_z}{\sqrt{m^2 + p_T^2 + p_z^2}}.$$

Solving this equation, y is defined as,

$$y \equiv \frac{1}{2} \ln \left(\frac{E + p_z}{E - p_z} \right).$$

This value is called *rapidity* of the particle. The shape of rapidity distribution dN/dy is invariant under z -boost.

For $p \gg m$, the rapidity may be approximated by the *pseudorapidity*,

$$\eta \equiv \frac{1}{2} \ln \left(\frac{p + p_z}{p - p_z} \right) = -\ln \left(\tan \frac{\theta}{2} \right).$$

The pseudorapidity distribution $dN/d\eta$ is also approximately invariant when $p \gg m$ and $\theta \gg 1/\gamma$. The advantage of the pseudorapidity to the rapidity is that it can be measured even the mass of the particle is unknown.

In the CDF, transverse energy E_T is frequently used since it is also invariant under z -boost. E_T is defined as,

$$E_T \equiv E \sin \theta$$

where E is the energy cluster observed in the calorimeter and the θ is a polar angle of a vector to the center of the energy cluster from an actual interaction point.

2.2 Tracking detectors

Tracking is important for identification of charged leptons. Since both electrons and photons leave similar signals in the calorimeter, the existence of particle track which matches to the energy cluster is an important evidence for the electron signal.

Tracking information also gives a momentum of a charged particle under the magnetic field. The CDF has a superconducting solenoidal magnet which produces 1.4 T magnetic field in the central rapidity region. This strong magnetic field enables the central tracking chamber to provide a precise momentum determination for charged particles.

Another important information provided by the tracking is an decay point of the long lived particle produced by the $p\bar{p}$ collision. This information plays a crucial role to identify those long-lived particles such as b -hadrons, which is a subject of the analysis in the thesis.

The CDF has four separate tracking detectors within the magnetic field as shown in Fig. 2.1. The outline of each detector is briefly described in the following sections.

Silicon Vertex detector: SVX

The SVX [17, 18] is a r - ϕ tracking device placed very close to the beam pipe. The main purpose of the SVX is to measure trajectories of charged particle precisely enough to distinguish b hadron decays using their relatively long decay length ($c\tau \sim 430\mu m$).

The SVX is divided into two modules at the $z = 0$ and each of half are called ‘barrel’. An SVX barrel is shown in Fig. 2.3. Each barrel consists of four concentric layers of silicon micro strip sensors. The inner and outer layers of the SVX are at radii of 2.86 cm and 7.87 cm, respectively. Total length of the SVX along z axis is 51 cm (25.5cm for a barrel) and this

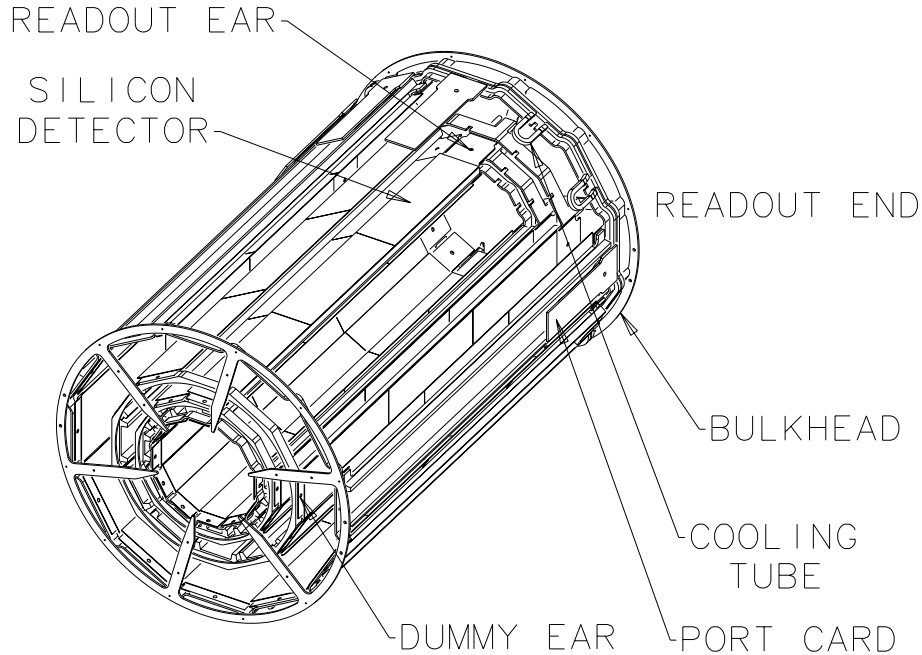


Figure 2.3: An isometric view of the SVX detector. $r = 7.9 \text{ cm}$, $l = \pm 25.5 \text{ cm}$.

length covers about 60% of $p\bar{p}$ interactions observed at the CDF.

Each of silicon sensors in a barrel have $60\mu\text{m}$ strips ($55\mu\text{m}$ for the fourth layer) along z axis on the one side. Signals from those strips are read out through 200 nm layer of SiO_2 to prevent saturation of the input amplifier from leakage currents in the detector. The individual hit resolution is obtained by fitting the charge distribution of neighboring strips, and the resolution is about $10\mu\text{m}$.

In the thesis, SVX plays a key role to extract b -quark events from inclusive electron sample. The SVX provides a precise measurement of the impact parameter which reflects the lifetime of the parent particle.

Vertex Time Projection Chambers: VTX

The VTX consists of 28 time projection chambers which are mounted end-to-end along the z -axis. Each of the chambers have a central high voltage grid in r - ϕ plane that make the chamber to have two drift region with 4 cm

long. Drift electrons move along z -axis toward multiple sense wires arranged in r - ϕ plane, concentric to the beam axis. Those wires provide r - z view of the track by measuring the arrival times of drift electrons using Time-to-Digital Converter (TDC). The r - ϕ tracking is also provided by cathode pads behind those wires.

The VTX has a very wide acceptance in polar angles ($3.6^\circ < \theta < 176.4^\circ$) and this enables us to determine z positions where hard $p\bar{p}$ collisions occurred. Knowledge of the location of the event vertex gives the first order correction in the calculation of physics quantities such as the transverse energy and also gives separation of multiple events in a single bunch crossing.

Central Tracking Chamber: CTC

The Central Tracking Chamber (CTC) [19] is a 1.3 m radius 3.2 m long cylindrical drift chamber which gives precise momentum measurements ($\delta p_T/p_T \sim 0.002 p_T$) in the angular region, $40^\circ < \theta < 140^\circ$ ($-1 < \eta < 1$).

The CTC has 84 layers of sense wires, which are basically strung along z -axis. Those layers are grouped into 9 *super-layers*. A superlayer consists of a single layer of drift cells (*super-cells*) that surround the z -axis. Each super-cell has multiple wires to form the electric field inside. The CTC has two kinds of superlayers which alternatively surround the z -axis as shown in Fig. 2.4. The first ones which start from the innermost layer are called *axial superlayers* and whose wires are strung exactly along z -axis. The axial superlayers provide r - ϕ view of the track. The CTC has 5 such axial superlayers. The rest superlayers (4 layers) are called *stereo superlayers* and whose wires are strung with an angle of $\pm 3^\circ$ relative to z -axis. The combined analysis of the information from the stereo superlayers and the axial superlayers provide r - z view of the track.

In each superlayer, super-cells are not arranged in parallel to the radial

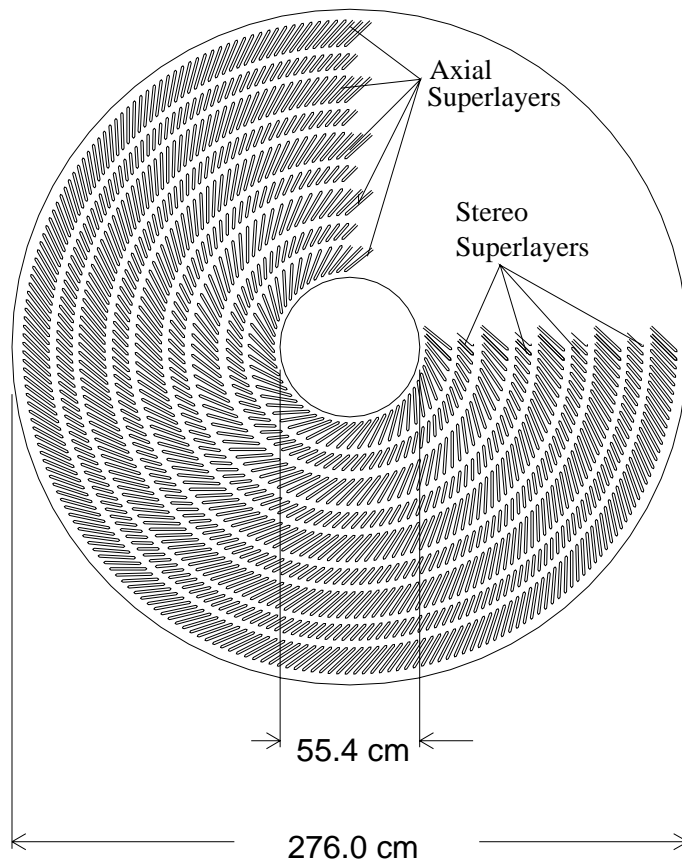


Figure 2.4: The CTC end-plate showing the wire slots.

Number of layers	84
Number of superlayers	9
Stereo angle	$0^\circ +3^\circ 0^\circ -3^\circ 0^\circ +3^\circ 0^\circ -3^\circ 0^\circ$
Number of cells/layer	30 42 48 60 72 84 96 108 120
Number of sense wires/layer	12 6 12 6 12 6 12 6 12
Sense wire spacing	10 mm in plane of wires
Tilt angle(center of plane)	45°

Table 2.1: Mechanical parameters of the CTC

direction. They are tilted 45° respect to the radial direction so that the drift trajectories of electrons are approximately azimuthal under the crossed magnetic and electric field. Without this tilt angle, dead space would emerge at the ends of the cells because of a large Lorentz angle. The tilt angle of the cells has an extra advantages of resolving tracks. Since the cells do not have a mirror symmetry respect to the radial plane, the track coming from the center of the CTC can be uniquely resolved.

The CTC wire gives an extra information for the particle identification aside from the track information. The pulse height of the wire signal reflects a magnitude of the energy deposition in the drift chamber. Since the energy deposition is a function of a velocity rather than the momentum, it is possible to extract the mass of the particle by combining the observed momentum and energy deposition. In the thesis, energy deposition (=charge deposition) in the CTC is represented by Q_{CTC} and used to help separating an electron in the analysis.

2.3 Calorimeters

The main purpose of the calorimeter is to measure the magnitude and the direction of all energy flow ¹ from an interaction point. One of the advantage of the calorimeter is its ability to identify the particular type of particles, i.e.

¹Except for neutrinos and muons since they deposit no or very small part of their energy in a dense material. The muon is detected with a muon chamber.

electrons and photons, using their characteristic signature of electromagnetic cascade in a dense material. An electromagnetic cascade is caused by a chain reaction of an electron-positron pair creation by a photon which is created by a bremsstrahlung of electrons(positrons). The calorimeter to measure the energy of the electromagnetic shower is called the electromagnetic (EM) calorimeter.

The energy of the hadron can also be measured using a shower in a dense material but a strong interaction take a important part of the developing process in this case. The shower development by a strong interaction is much slower than electromagnetic shower as a function of material depth. For this reason, the calorimeters to measure hadronic energies need to have a larger depth than the EM calorimeter and it is located behind the EM calorimeters.

The CDF calorimeters use projective tower geometry, which points back to the nominal interaction point. Those towers cover the pseudo-rapidity range from -4.2 to 4.2, and cover full range in the azimuthal angle as shown in Fig. 2.5.

We use the central electromagnetic calorimeter (CEM) to tag the electron from b -hadron decay, and the forward calorimeter (FCAL) to detect the rapidity gap signature of pomeron exchange events.

Central Electromagnetic Calorimeter: CEM

The central electromagnetic calorimeter (CEM) [20] and the central electromagnetic shower max counter (CES) are the important tools to identify the electron production in the central rapidity region. They also provide the ‘central electron’ trigger.

The CEM covers the pseudorapidity range from -1.1 to 1.1 and has the full coverage in ϕ using 478 projective towers. The size of a tower is $0.1(\eta) \times$

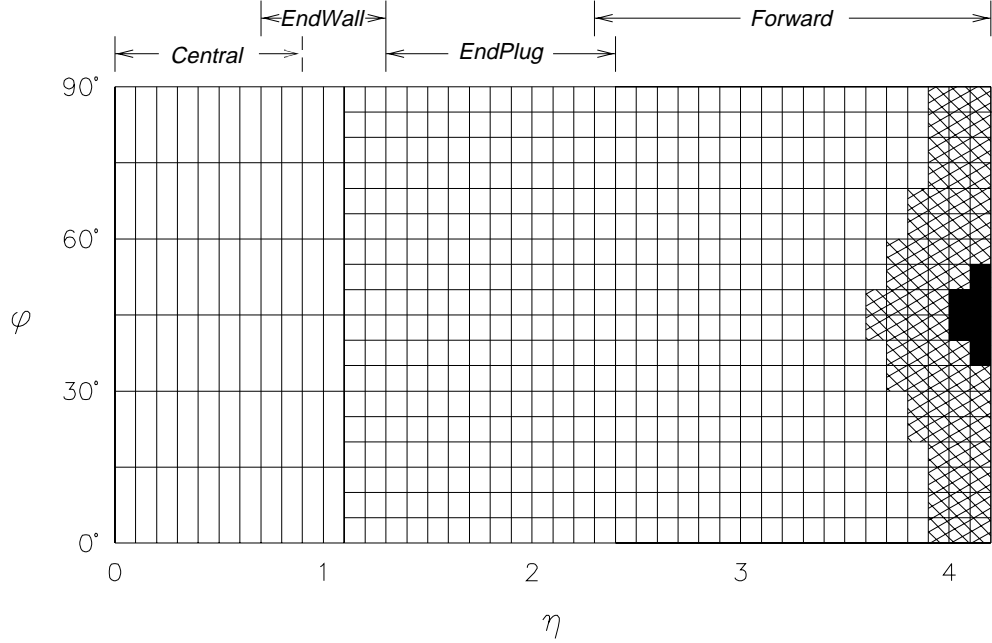


Figure 2.5: The CDF calorimeter segments shown in $\eta - \phi$ plane. Hatched area shows partial depth coverage only due to cut for low beta quadrupoles. Black area shows no coverage.

$15^\circ(\phi)$ ($24.1\text{cm} \times 46.2\text{cm}$) and this size is large enough to cover a typical electromagnetic shower development of a few cm in lateral size. The depth of a tower is 18 radiation length (0.6 absorption length). The CEM uses lead sheets interspersed with scintillator as the active detector medium. The scintillation light from the scintillators in a tower is collected and piped into the photomultiplier (PMT) through the wavelength-shifter. The CEM have an electron energy resolution of $\sigma/E = 13.5\%/\sqrt{E_T} \oplus 2\%$ (the symbol \oplus signifies that the constant term is added in quadrature in the resolution and E_T is in GeV).

The CES is embedded at the depth of 5.9 radiation length in the CEM measured from the solenoidal coil. The longitudinal shower development becomes maximum at this depth in average. The CES is a proportional gas chamber to measure the position and the lateral shape of the electromagnetic shower at the maximum development. The CES is made up with strips

	CES chamber		CPR chamber
	Wires (r - ϕ view)	Strips (z view)	Wires (r - ϕ view)
Number of channels	32	69 ^a , 59 ^b	16
Spacing (cm)	1.45	1.67 ^a , 2.07 ^b	2.2
Spatial resolution (cm)	0.2	0.2	-
Saturation energy (GeV)	150	150	>150
Chamber length in z (cm)	234		103
Chamber width in ϕ ($^\circ$)	14.0		12.1

^aFor CES segment between $6 \text{ cm} < z < 115 \text{ cm}$.

^bFor CES segment between $115 \text{ cm} < z < 240 \text{ cm}$.

Table 2.2: Description of the shower max detector (CES) and preshower detector (CPR).

perpendicular to the beam axis and wires along the beam axis. It measures the shower position in twodimensions with the resolution of $2 \text{ mm}(r\text{-}\phi\text{:wire}) \times 2 \text{ mm}(z\text{:strip})$.

Central and Endwall Hadron Calorimeters: CHA, WHA

The central hadronic calorimeter (CHA) [21] lays after CEM, covering $|\eta|$ up to 0.9. It is mounted around the solenoid consisting of steel plates and acrylic scintillator. Because the CHA is placed in outer radius, it covers the pseudorapidity range $|\eta| < 0.9$, with the end-wall hadron calorimeter (WHA) extending this coverage out to $|\eta| < 1.3$. The CHA consists of 32 layers of 1 cm thick scintillator interleaved with layers of 2.5 cm thick steel. The WHA is made up of 15 layers of 5 cm thick steel followed by 1 cm thick scintillator. It presents 4.5 absorption lengths of material and has an energy resolution of $75\%/\sqrt{E} \oplus 3\%$.

Forward Electromagnetic Calorimeter: FEM

The forward electromagnetic calorimeter (FEM) [22] is placed at $\sim 6\text{m}$ away from the nominal interaction point in the z -direction to provide the informa-

tion of electromagnetic energy flow in the small angle region near the beam line. Two FEM are placed in the forward and the backward of the CDF. The FEM covers the pseudorapidity range from 2.3 to 4.2 ($11^\circ > \theta, \pi - \theta > 2^\circ$) and has the full coverage in azimuthal angle.

The FEM is a sandwich calorimeter of 30 lead (96% P_b ,6% S_b) sheets and 30 proportional gas chambers. The depth of the detector is $25.5 X_0$. The FEM is physically divided into quadrants at the x - z and y - z plane. The cathode pads of the chamber layers are ganged in the longitudinal direction in order to form the projective tower geometry of the unit of $0.1(\eta) \times 5^\circ(\phi)$. The tower has two depth segmentations both of which are 15 layers thick. The anode wires of chamber do not form a tower as pads, but they are ganged in each layer to form the sectors. The quadrant has 5 sectors per layers, and those sectors are read out independently for each layer.

The anode information of individual layers is not used for energy measurement itself, but used to reject the hit of slow neutron which mimic the unexpectedly high energy signal in a tower [23]. The slow neutron can kick out a slow proton in a detector, and the ionization energy loss of a slow proton is extremely larger than the one for the relativistic proton. Since a slow proton cannot go through the lead radiator layer, the high dE/dx signal is observed only in a single anode layer.

Forward Hadron Calorimeter: FHA

The forward hadron calorimeter (FHA) [24] measures the hadronic energy flow in the small angle region. It is placed behind the FEM and those two calorimeters provide a comprehensive energy measurements for this rapidity region, $2.2 < |\eta| < 4.2$. The structure of the FHA is similar to the FEM. It is a sandwich calorimeter of 27 steel plates and 27 ionization chambers. The FHA is also divided into quadrants, and the cathode pads in the chamber form

the projective tower geometry with the unit of $0.1(\Delta\eta) \times 5^\circ(\Delta\phi)$. The anode wires in each chamber layer form six sectors. The signal from those wires can be used to independently monitor the performance of the calorimeter and to provide information on the longitudinal development of showers in the detector.

In the analysis of the thesis, FEM and FHA are used to tag the rapidity gap signal in this forward rapidity region.

2.4 Central Preshower chamber: CPR

The central preshower chamber (CPR) is a multi-wire proportional chamber placed between the the CEM and the solenoid magnet coil. It samples the electromagnetic showers that started in the solenoid magnet material ($1.075X_0$). It has 2.22 cm cells segmented in r - ϕ and are positioned at a radius of 168 cm from the beam line. It consists of four chamber divisions spanning ± 1.1 units of pseudo rapidity η .

In the electron identification, the CPR provides the useful information to separate the real electrons from the hadrons which mimic the electron signal in the CEM. An electron tends to start making a shower in the solenoid and thus leave a large pulse in the CPR, while a hadron tends to leave only a minimum-ionizing pulse.

2.5 Beam-Beam Counter: BBC

The beam-beam counter (BBC) consist of a set of scintillator hodoscopes mounted around the beam pipe at ~ 6 m from the nominal interaction point. The east and west BBCs cover the pseudorapidity range $3.24 < |\eta| < 5.89$ ($0.317^\circ < \theta < 4.47^\circ$, $0.317^\circ < \pi - \theta < 4.47^\circ$). The east BBC covers the positive η range, and the west BBC covers the negative. The BBC is used as the primary luminosity monitor. It also provides a relatively unbiased

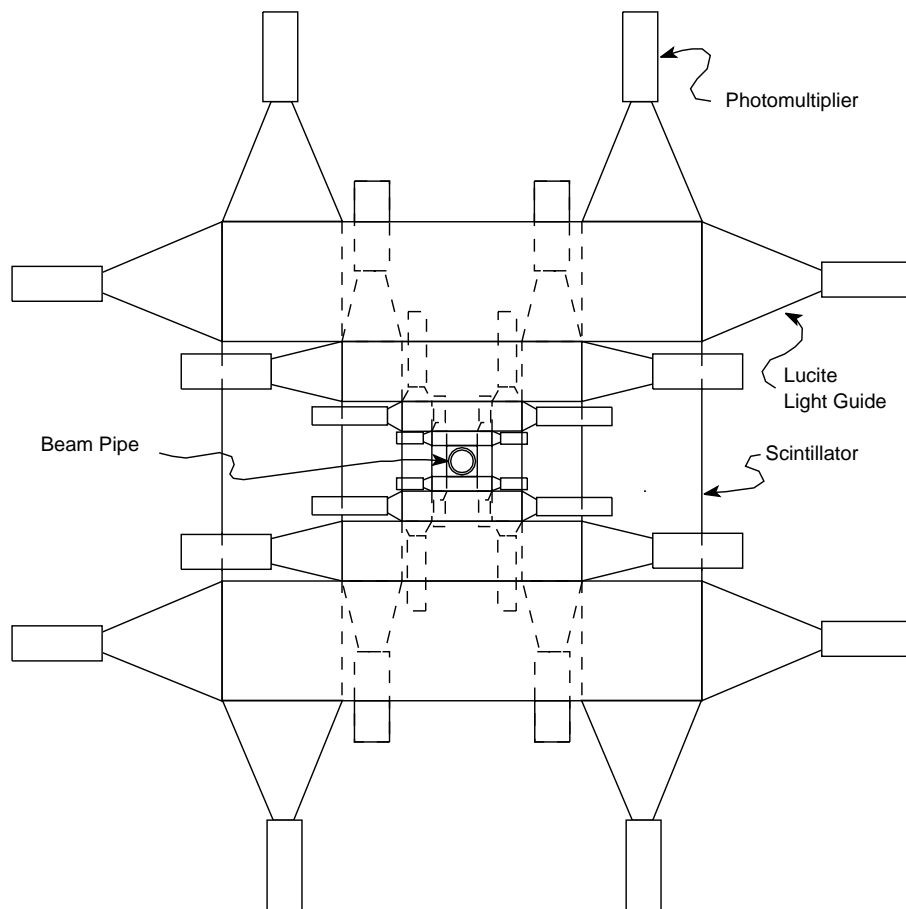


Figure 2.6: BBC counter.

“minimum-bias” trigger.

The arrangement for the BBCs is shown in Fig. 2.6. Each set of counters consists of 2 layers of scintillators; the layer closest to $z=0$ being mounted horizontally and the other layer being mounted vertically. Their sizes are adjusted so that they subtend roughly equal amounts of rapidity ($\Delta\eta \sim 0.67$). Each scintillator is viewed by a phototube at each end.

In the thesis, the BBC is used as an important tool to tag the rapidity gap signal in addition to the forward calorimeters.

2.6 Trigger

In the CDF, the cross section for the inelastic events which at least hit the BBC in both sides is **50mb**. On the other hand, the cross section for more interesting events, for example $W \rightarrow e\nu$ is only $2 \times 10^{-6}\text{mb}$. It is thus crucial for the experiment to implement the sophisticated trigger into the detector complex.

The CDF employs a three-level trigger system [25, 26]. The idea behind the multi-level trigger structure is to minimize the deadtime and to give a flexibility for the system. Several kinds of triggers are implemented in each level and the event is selected if it passes at least on of those triggers in each level. The only those relevant to the analysis are described below.

Level-1

The Level-1 decision is made within the $3.5\mu\text{sec}$ between beam crossings and it therefore incurs no deadtime. In this level, the decision is made with the simple information such as energy deposition in the calorimeter, the coincidence of east and west BBCs and the existence of the stiff track in the chamber (but no their positions). Neither no energy clustering nor no tracking is made.

The central calorimeter consists of projective towers of $0.1(\eta) \times 15^\circ(\phi)$. In order to reduce the number of signals, the logical trigger tower of $0.2(\eta) \times 15^\circ(\phi)$ is produced by summing the analog outputs from adjacent two towers. The electromagnetic and the hadronic towers are individually treated in the trigger. The analog signal from the trigger tower is corrected for a bias level and a gain variation, and then converted into a transverse energy by giving a $\sin\theta$ weight according to the tower position. All those correction are made in the analog stage. The trigger tower E_T is compared with certain threshold levels provided by programmable Digital-to-Analog Converter. The main Level-1 trigger which accepts the central electrons is the one using E_T threshold of 8.0 GeV for the EM energy. When a particular analog signal is over this threshold, the event is passed into the Level-2 stage.

Level-1 delivers a rate of a few kHz to the next level.

Level-2

In this stage, topological features, such as energy clusters and tracks, are reconstructed and used for the event selection. This process needs $\sim 20\mu\text{sec}$ and incurs about 5~10% downtime.

The hardware energy clustering in the calorimeter is performed using the analog signals from trigger towers. A list of the cluster properties, including position, width, and transverse energy is compiled. The hardware track reconstruction is also performed using the CTC outputs but only for r - ϕ plane [27]. Results of those reconstruction are analyzed by fast computation modules specialized to select each subjects; jets, electrons, muons and so on. The “electron” events are selected based on the cluster width, the ratio of electromagnetic to hadronic energy deposition and the presence of a high p_T track. In RUN1B, the new hardware trigger which implements the CES information was also used for electron selection [28].

Level-3

When the event passes the level-2 trigger, the entire information from the CDF detector is digitized and readout by the front end scanners. After finishing readout, the level-1 and the level-2 systems are released to evaluate the next events again. The readout data are reformed into a standard format for the offline analysis and then pushed into one of the buffers in the level-3 trigger system. The Level-3 trigger is a software trigger running on UNIX machines. The system consists of 96 buffers and 48 nodes which process the events in parallel. The electron selection in this stage is based on almost the same information as used in the offline analysis. We will describe this event selection criteria in the next chapter. The event which passes Level-3 trigger is recorded on the 8 mm tape at a rate of about 10 Hz.

Chapter 3

Event selection

In this chapter the b -quark event selection is described. We started with the events that satisfy the “electron” requirement in the CDF trigger system during the run time. However, substantial amount of the non-electron background still remains in this stage. We apply tighter electron identification criteria to remove the non-electron background events. Additional requirements on the remaining events are made to enrich the b -quark event fraction. It also ensure the good measurements of some variables (Impact parameter, p_T^{rel}) used to estimate the b -quark event fraction. Finally the diffractive candidates are selected from the b -quark candidates by the rapidity gap tagging.

3.1 $b\bar{b}$ candidate selection

3.1.1 Central electron trigger

We start from the data sets which includes electron candidates observed in the CEM. In this data sets, the following selection criteria have been applied at the level-3 trigger. The terms used in this lists are described later.

- $E_T(\text{ele})^1 > 7.5 \text{ GeV}$
- $P_T(\text{ele}) > 6.0 \text{ GeV}/c$

¹The transverse energy is calculated using the nominal interaction point

- $L_{SHR} < 0.2$
- $HAD/EM < 0.125$
- cluster-track matching at the CES: $r\Delta\phi < 3.0$ cm
- cluster-track matching at the CES: $\Delta z < 5.0$ cm
- $\chi_{strip}^2 < 10$

In order to avoid the trigger bias which kill the rapidity gap events, we ensure that the events are not collected by the level-1 trigger of the west and east BBC coincidence. We selected the events taken by the central electron triggers (CEM_8_CFT_7_5_V* or CEM_8_CFT_7_5_XCES*) in order to compare the physics results to the Monte Carlo simulation which models this trigger.

3.1.2 Electron identification

We first define the electron energy cluster in the central EM calorimeter. Since the lateral size of electromagnetic shower is smaller than the size of single tower, the maximum size of the electron cluster is restricted to the 3 towers in the η direction and only one tower in the ϕ direction $[0.3(\eta) \times 15^\circ(\phi)]$. The E_T threshold used for the clustering is 0.1 GeV. The “electron track” is defined as the highest momentum track which points to the electron energy cluster.

Electron identification at the CDF is basically performed using a signature of electromagnetic shower development in the EM calorimeter and the presence of the track in the CTC.

However, a charged hadron which leaves a track in the CTC can mimic the electron signature in the calorimeter by the energy deposition through the π^0 s production in the material. The produced π^0 immediately decays into two photons that start an electromagnetic shower. This background

(“hadron faking electron”) is difficult to separate since the shower shape is basically identical to the electron.

Another source of event which mimics the electron signature is an overlap hit of a charged hadron and photons on the same calorimeter cluster. In the Tevatron, most of photons are produced by $\pi^0 \rightarrow \gamma\gamma$ decays in the QCD jet. Those two photons from the π^0 decay tend to point to the single electron energy cluster since the two photon system is highly boosted toward the calorimeter comparing to the pion mass. The lateral shape of such electromagnetic shower caused by two photons is different from the single electron’s one and this property is used to reject those events.

In order to suppress the above non-electron backgrounds we applied the following electron identification cuts:

Hadronic energy fraction: HAD/EM

A ratio of hadronic to electromagnetic cluster energy HAD/EM is used to identify the isolated electromagnetic shower signature. We use the upper bound of the HAD/EM of 0.04 when a single CTC track is pointing to the calorimeter energy cluster. When multiple tracks are pointing to the cluster, we loosen the upper bound of the HAD/EM to 0.10.

Energy momentum ratio: E/p

The energy and momentum match is required since we selected isolated energy cluster for an electron candidate. This cut is useful to reject the accidental overlap of charged hadrons and photons. We used the allowable E/p range from 0.75 to 1.4.

Lateral shower shape adjacent towers: L_{SHR}

The energy sharing in adjacent towers for electrons is very different from that for an overlap of photon and hadron. Most electrons deposit the energy on a

single CEM tower since the typical lateral size of electromagnetic shower is smaller than the tower size. On the other hand, an overlap event of charged hadron and multiple photons could leave extra energies in towers adjacent to a seed tower by multi-photon hit. So this type of background can be suppressed by requiring a tower energy profile in a three-tower sum cluster.

The lateral shower profile L_{SHR} [29] is defined by comparing the measured energy sharing to the test beam data.

$$L_{SHR} = 0.14 \times \sum_i \frac{E_i^{adj} - E_i^{prob}}{\sqrt{0.14^2 E + (\Delta E_i^{prob})^2}}.$$

Here, E_i^{adj} is the measured energy in the tower adjacent to the seed tower; E_i^{prob} is the expected energy in that tower calculated from the seed energy of the cluster, the impact point from the strip chamber, and the event vertex using a shower profile parameterization from test beam data; E is the EM energy in the cluster; and ΔE_i^{prob} is the error in E_i^{prob} associated with a 1-cm error in the impact point measurement. The sum is over the two towers adjacent to the seed tower in the same azimuthal wedge. We required L_{shr} to be less than 0.2 for an electron candidate.

Lateral shower shape in a seed tower: CES χ^2

A finer profile of a lateral shower shape in the seed tower is measured using strip and wire information of the CES. This profile is also used to reject the overlapping background.

In the CES, 11 strips (18~23cm) around the peak channel is used to sample the shower shape perpendicular to the beam line. The shower shape along the beam line is also sampled by the CES wires in the same way.

The measured energy distribution in strip and wire channels are compared with those of test beam data to calculate a χ^2 . We require the χ^2 to be less than 10.0 for electron candidates in both strip and wire views.

Position matching: $r\Delta\phi, \Delta z \sin\theta$

The position matching of the shower centroid and the electron trajectory is required to reject the overlapping background. The shower centroid of the electron candidate is obtained by fitting the measured lateral profile with the CES to that expected from the test beam profile, as described in the previous section. The position in the local CES coordinate system is represented with (X_{ces}, Z_{ces}) , corresponding to $r \times \phi$ and z in the CDF coordinate system. The CTC track of the electron candidates is extrapolated to the detector radius where the CES is placed to calculate the deviation of this extrapolated track from the shower centroid. We require the deviation in the r - ϕ view $\Delta X_{ces}(= r\Delta\phi)$ to be less than 1.4 cm. We also require the deviation in the polar angle view $\Delta Z_{ces} \sin\theta(= \Delta z \sin\theta)$ to be less than 2.0 cm.

CPR charge

The CPR charge deposition is useful to reject the hadron faking electrons. Since a hadron hardly starts a shower before the CPR layer, it deposits less charge in the CPR than real electrons.

The charge deposition in three CPR wires (6.6 cm) around an ‘electron’ trajectory are summed and then corrected depending on both the angle and the momentum of the track (see Appendix B).

The CPR charge distribution for real electrons is significantly different from for the hadron rich sample. We used a lower bound of the CPR charge of 2.0 for electron identification, where the selection efficiency for real electron(hadron) is 93%(46%).

3.1.3 Additional requirements

There are several other processes to produce real electrons aside from the b -hadron decay.

One of the main source of the electron is a photon conversion process in the detector material ($\gamma N \rightarrow e^+e^-N$). The Dalitz $\pi^0 \rightarrow e^+e^-\gamma$ decay also produces the real electron. Those events are characterized by the pair production of the two oppositely charged particles (e^+e^-).

The weak boson decay ($W \rightarrow e\nu, Z \rightarrow e^+e^-$) is another source of the real electron. The electron from this process is characterized by a large transverse momentum because of a large mass of the weak boson, $\sim 80 \text{ GeV}/c^2$.

The most difficult source of the electron to separate is a semi-leptonic decay of a charm quark. In order to achieve the separation of b -hadron from c -hadron decay, we require a good reconstructed track for the electron in the SVX and an associating jet around the electron track.

The additional requirements for the b -quark candidate selection is described here. Some fundamental quality cuts to ensure the good measurements of the electron energy are also listed.

Photon conversion rejection

The opening angle between the electron-positron pair produced by the photon conversion process is very small since the mass of the parent particle is zero. This is also the case with the electron-positron pair which is produced through a Dalitz decay $\pi^0 \rightarrow e^+e^-\gamma$ because the mass of the parent is much smaller than its kinetic energy.

To identify those events, a conversion partner track of the electron candidate is searched from all CTC tracks (“conversion finding method”). The following cut are applied to an oppositely charged track to the electron candidate:

- $|\delta S| < 0.2(\text{cm})$
- $|\delta \cot \theta| < 0.06$

The $|\delta S|$ is a distance between two trajectories when they become parallel in the $r-\phi$ plane. The $|\delta \cot \theta|$ represents a parallelism of two trajectories in the $r-z$ plane defined by the difference between $\cot \theta$ of two trajectories. If there exists a track which satisfies the above requirements, we reject the candidate as a conversion electron.

The another method to identify a conversion electron is to look a continuity of the drift chamber tracks. When a photon conversion take place in the material between the two chambers, an ionization track is observed in the outer chamber but not in the inner chamber. We use the hit occupancy of the VTX (VTX_{occ}) to reject the conversions occurring outside the VTX. The VTX_{occ} is defined as a ratio of the number of VTX wire hits to the number of wires which are expected to be fired by a particle.

- $VTX_{occ} > 0$

Ideally, we should not have such “outside” conversions in the sample because we require a hit in the SVX placed inside the VTX. However, it is possible to link the hits in the SVX to the wrong CTC track in the actual track reconstruction.

Weak boson rejection

W decay events ($W \rightarrow e\nu$) is characterized by a large missing E_T and a large electron E_T . The missing E_T , denoted by \cancel{E}_T is defined to be the vector sum of transverse energy in calorimeter towers over the pseudorapidity range $|\eta| < 3.6$;

$$\cancel{E}_T = \left| - \sum_{|\eta| < 3.6} \vec{E}_T \right|.$$

We use the following cuts to reject W decays:

- $E_T(\text{ele}) < 20\text{GeV}$

- $\cancel{E}_T < 20\text{GeV}$

The electron from $Z \rightarrow e^+e^-$ decay also has a large E_T . This event is also rejected by the above electron E_T cut.

electron E_T

We require the electron to have an E_T above 9.5 GeV in order to minimize a bias on the E_T spectrum due to a trigger inefficiency. The trigger efficiency depends on both E_T and P_T .

- $E_T(\text{ele}) > 9.5\text{GeV}$

Track quality

For the high precision measurement of the impact parameter, we require the electron to have a good reconstructed track in the SVX. We require the track to have the hits in at least three SVX layers. The χ^2 of the reconstructed track divided by the number of hit SVX layers is required to be less than 6.

- $N_{svx} \geq 3$
- $\chi_{svx}^2/N_{svx} < 6$

In the CTC, reconstructed electron track was required to have at least 2 axial layers with at least 5 hits each and at least 2 stereo layers with at least 2 hits each.

Vertex position

To ensure the good energy measurement in the projected tower geometry of the calorimeter, we require z_0 of the electron track to be within 60 cm of the nominal interaction point. However, this cut is somewhat too deliberate because we require the electron to have a hit in the SVX which is ± 26 long in z direction.

- $|z_0(\text{ele})| < 60\text{cm}$

Associating jet requirement

In order to measure the p_T^{rel} (see Sec. 5.2), the associating jet is required for the electron track. Jets are reconstructed by clustering tracks in the CTC, using the following algorithm [30]: all ‘good’ tracks with $p_T > 1.0$ GeV/ c are found and placed into an array of ‘seed’ tracks; the seed tracks are looped over and if another seed track lies within the cone $R=0.4$, where $R^2 = \Delta\eta^2 + \Delta\phi^2$, then the two seeds are merged into one by summing their momenta vectorally; this process is iterated until no new merging occur; the final phase of clustering consists of merging ‘good’ tracks with $p_T > 0.4$ GeV/ c that lie within the seed cones. Once the jets have been clustered, p_T^{rel} is calculated using the jet that is closest to the electron in R .

In this clustering algorithm, the ‘good’ track is defined by the following conditions: the good track is reconstructed as a 3D track; the track have at least 2 axial layers with at least 5 hits each and at least 2 stereo layers with at least 2 hits each; the track has a common origin to the electron track, $|z_0 - z_0(\text{ele})| < 5\text{cm}$; the impact parameter of the track is within 5.0 cm.

The associating jet to the electron is required to have at least 3 tracks including the electron track.

Summary of the selection criteria

All selection criteria listed above are summarized in Table 3.1. We obtain 161,775 electron candidates using the above selection criteria.

3.2 Diffractive candidate selection: Rapidity gap tagging

The diffractive b -quark production events in the about 160k electron candidates are extracted using a rapidity gap method [10, 11].

We used two kinds of forward detectors in the rapidity gap analysis: the

$9.5 < E_T(\text{ele}) < 20.0 \text{ GeV}$
HAD/EM < 0.04 for 1 track
HAD/EM < 0.10 for multiple tracks
$0.75 < E/p < 1.4$
$L_{SHR} < 0.2$
$\chi^2_{strip} < 10.0$
$\chi^2_{wire} < 10.0$
$\Delta X_{ces} < 1.4 \text{ (cm)}$
$\Delta Z_{ces} \sin\theta < 2.0 \text{ (cm)}$
Good fiducial hit in the tower
CPR charge > 2.0
Conversion rejection
$\cancel{E}_T < 20 \text{ GeV}$
Good SVX track: $N_{svx} \geq 3, \chi^2/N_{svx} < 6$
Good CTC track
Associating jet must be reconstructed for the electron track
$ z_0(\text{ele}) < 60 \text{ cm}$

Table 3.1: Summary of the event selection cuts.

BBC ($5.9 > |\eta| > 3.2$) and the forward calorimeter ($4.2 > |\eta| > 2.4$). The analysis is based on the BBC multiplicity and the number of calorimeter clusters with energy above 1.5 GeV, in the same rapidity side. The cluster energy threshold of 1.5 GeV is used to suppress the calorimeter noise. We make the tower clusters as follows: We pick up the towers with E_T above 0.1 GeV. For the towers with E_T below 0.1 GeV, we apply the additional requirements of $E(\text{EM}) > 0.5 \text{ GeV}$ and $E(\text{HAD}) > 0.8 \text{ GeV}$. After this cut, all survived towers neighboring to each other are clustered within the cone size of $\sqrt{(\Delta\eta)^2 + (\Delta\phi)^2} = 0.25$.

The correlation plot of the BBC multiplicity N_{BBC} and the cluster multiplicity N_C is shown in Fig. 3.1. The $+\eta$ and $-\eta$ sides are plotted in the same figure. The distinct peak at the zero multiplicity bin ($N_{BBC} = N_C = 0$) is observed in this plot. This is a rapidity gap signature of single diffractive events. This gap is caused by an exchange of colorless object between two incoming beam particles. We define the diffractive signal region to this zero

multiplicity bin. In this diffractive signal region, 100 events are observed. Figure 3.2(a) shows the electron E_T spectrum for the diffractive candidates compared that for the whole electron sample. Those two spectra do not show any significant difference. Figure 3.2(b) shows the pseudorapidity distribution of the electrons. Diffractive candidates tagged with positive rapidity side are plotted after changing the sign of the electron η so that rapidity gap is always come to left side of the plot. The diffractive candidates show a small shift toward the opposite side of the rapidity gap.

The background fit of the non-diffractive events in the signal region is performed using the one-dimensional multiplicity plot (Fig. 3.1(b)) obtained by picking up the diagonal bins in Fig. 3.1(a). We fit the high multiplicity region using a straight line and then extrapolate it to the diffractive signal region. The background fit yields 24.4 ± 5.5 non-diffractive events in the diffractive signal region.

We have checked a possible difference between two rapidity sides. The number of diffractive candidates in each rapidity side is analyzed individually as shown in Fig. 3.3 and Fig. 3.4. The number of diffractive candidates is 38.1 ± 7.7 in the $+\eta$ side and 37.9 ± 8.4 events in the $-\eta$ side. We thus conclude that the difference between two forward detectors is negligibly small.

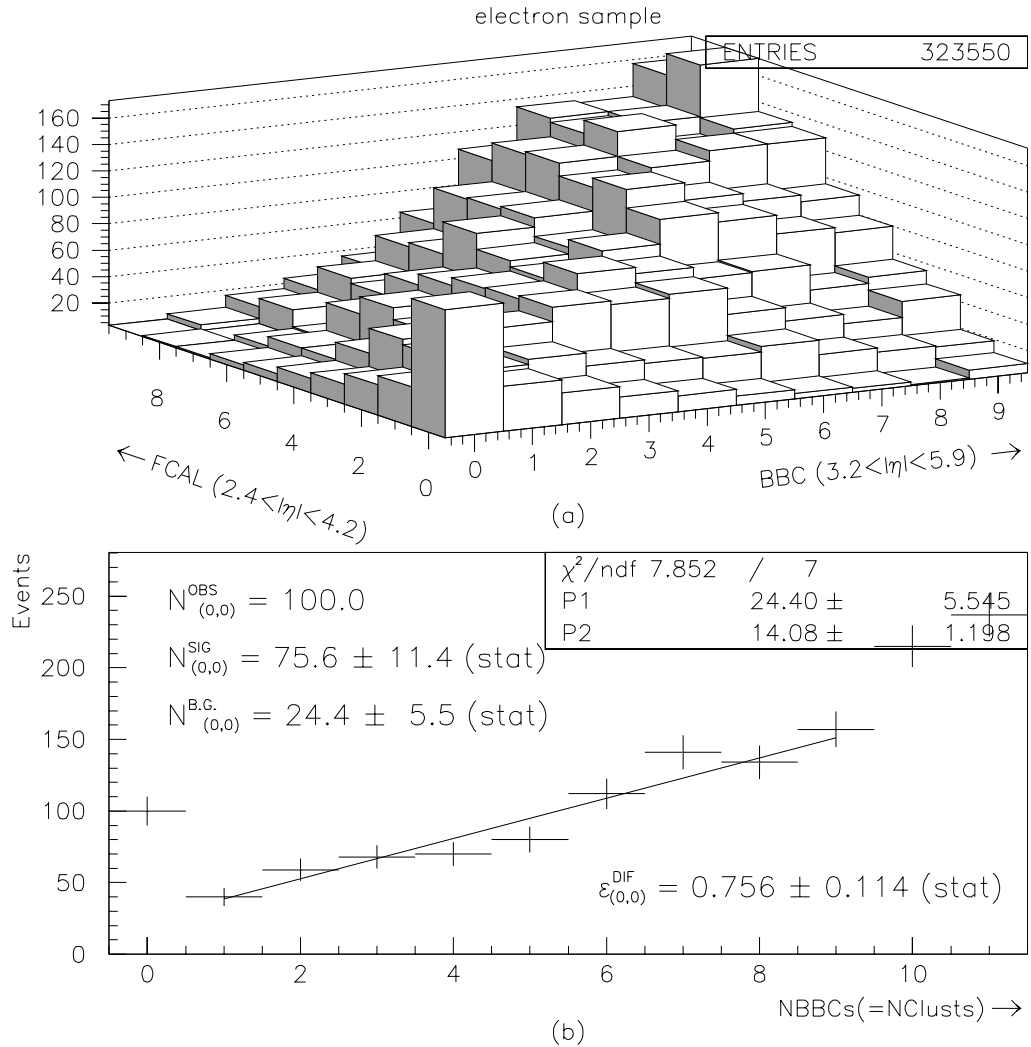


Figure 3.1: (a) BBC multiplicity versus adjacent forward calorimeter cluster multiplicity (two entries per events). (b) Multiplicity along the diagonal axis in the above plot. Non-diffractive background in the zero multiplicity bin is estimated by a streight line fit.

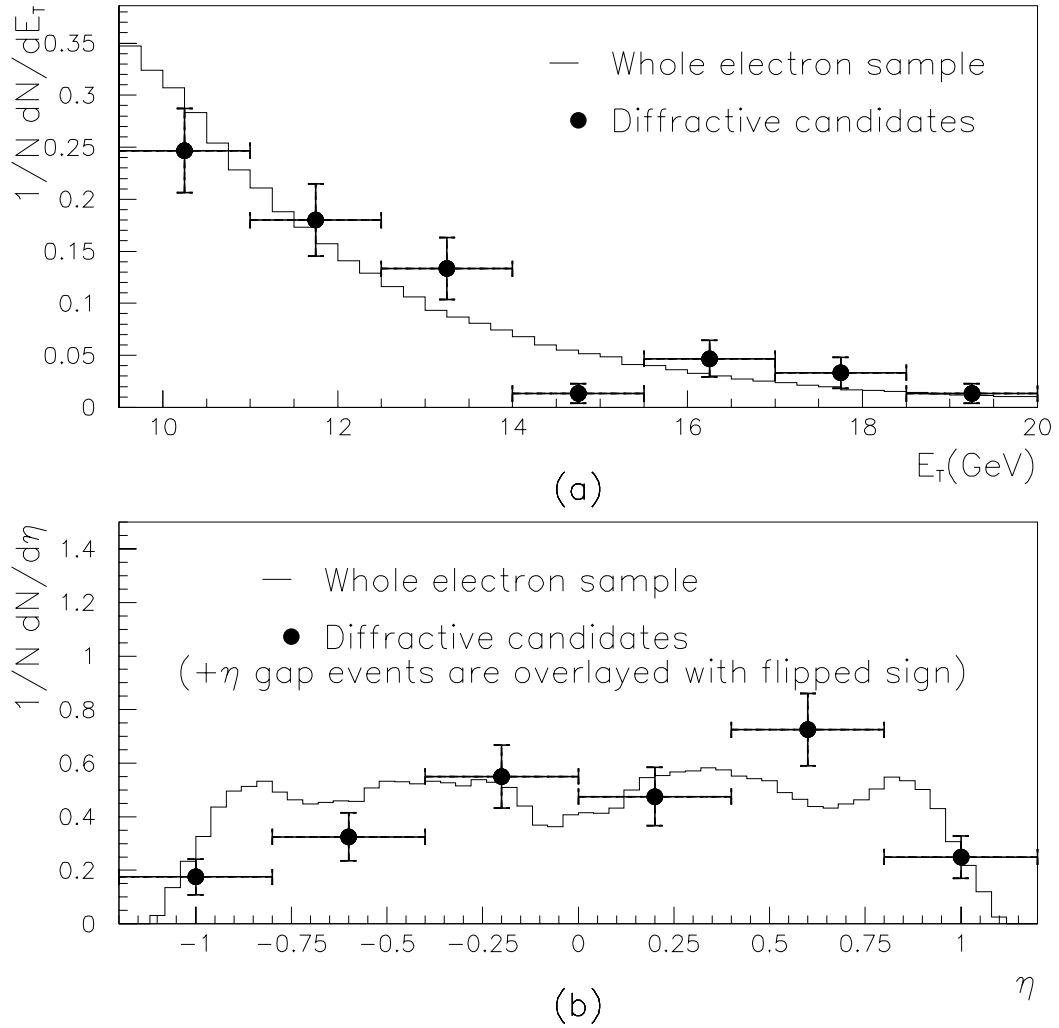


Figure 3.2: (a) Transverse energy spectrum of electrons. The solid histogram shows whole electron sample and solid circles show the diffractive candidates. (b) Pseudorapidity distribution of electrons. The solid histogram shows whole electron sample and black circles show the diffractive candidates. The diffractive candidates tagged by the $+\eta$ side gap are plotted with an inverted sign of its electron pseudorapidity.

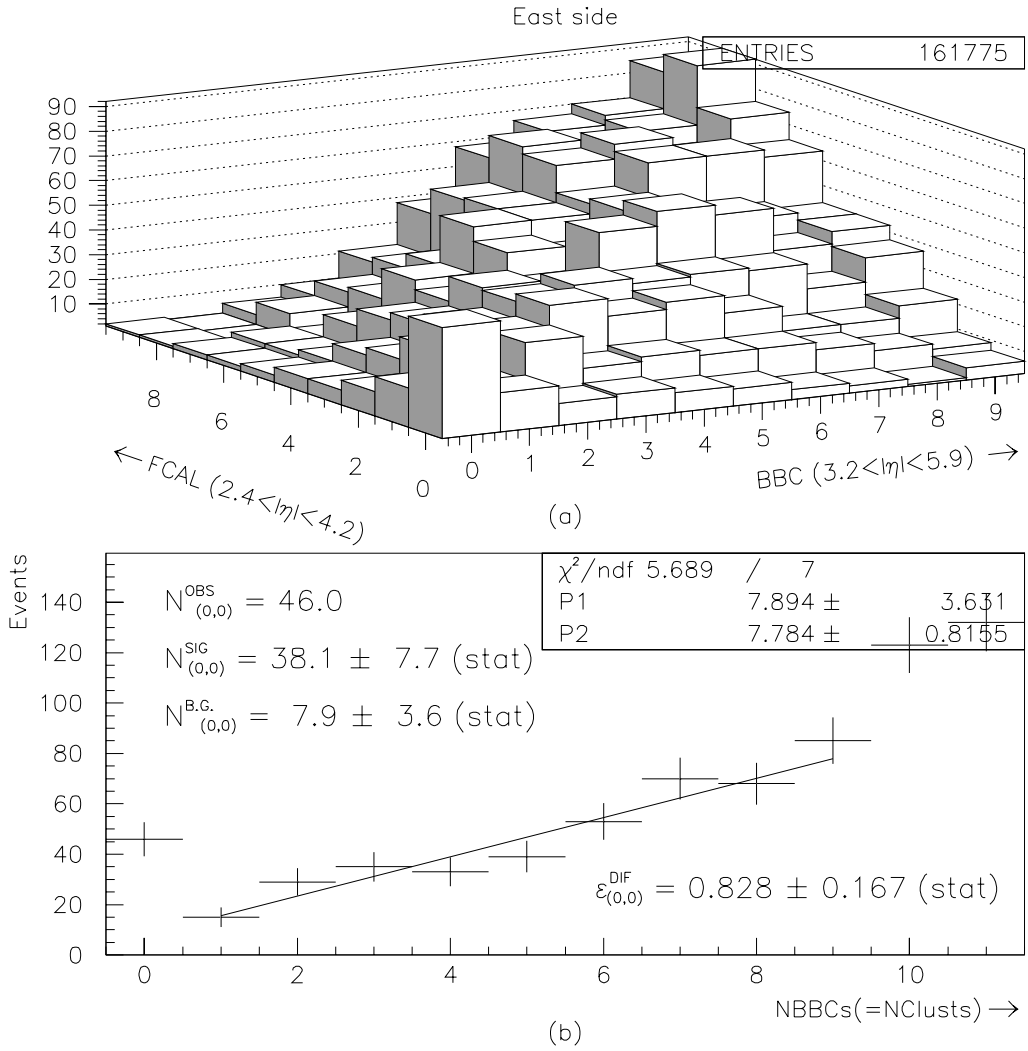


Figure 3.3: (a) BBC multiplicity versus cluster multiplicity in $+\eta$ side (two entries per events). (b) Multiplicity along the diagonal axis in the above plot.

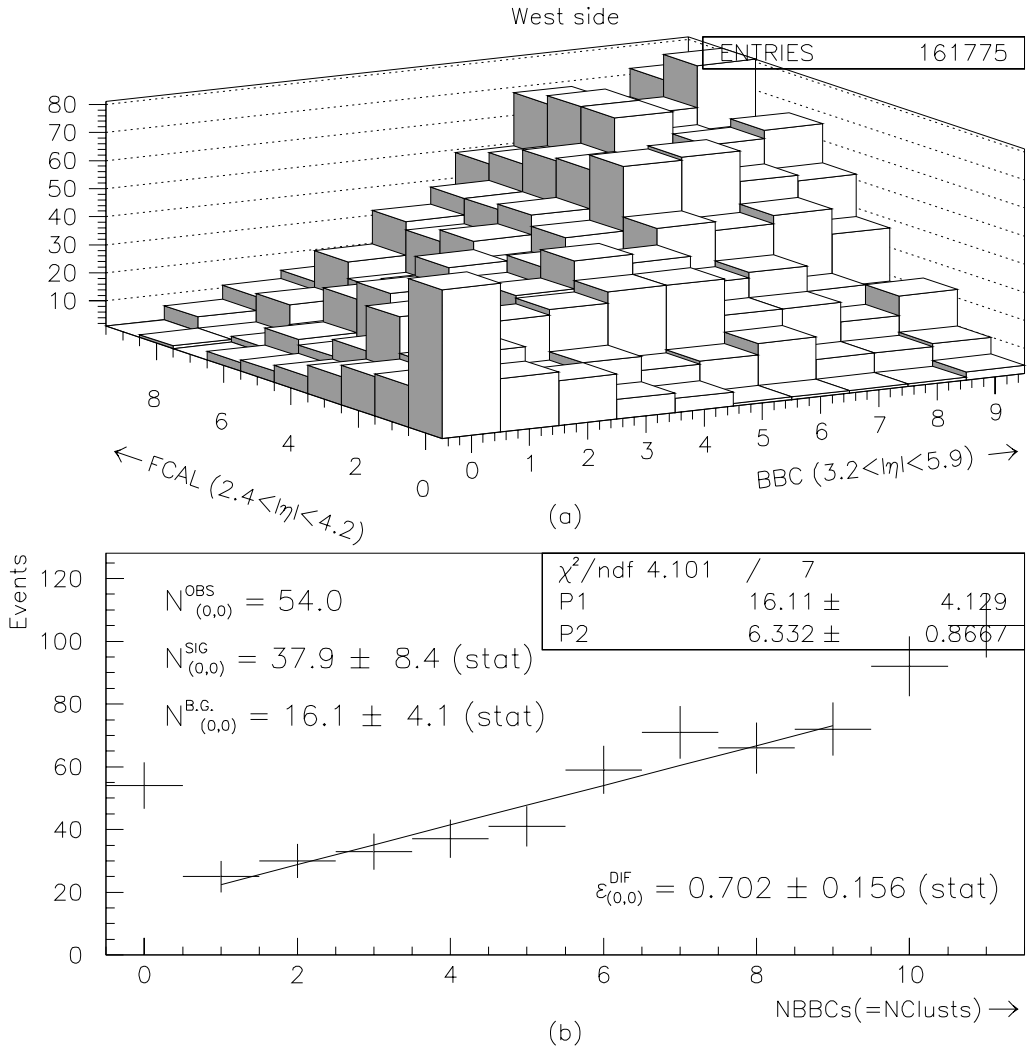


Figure 3.4: (a) BBC multiplicity versus cluster multiplicity in $-\eta$ side (two entries per events). (b) Multiplicity along the diagonal axis in the above plot.

Chapter 4

Background from non-heavy flavors

In the previous chapter we described the selection criteria to make the sample of the $b\bar{b}$ production candidates. We will call this sample as a “whole electron sample”. Although we have applied tight electron cuts, we still have three types of backgrounds in the whole electron sample: (i) charged hadrons faking electron, (ii) electrons from photon conversions and (iii) electrons from c -quarks. In the latter two backgrounds, we have real electrons. We estimate the residual number of photon conversions using the efficiency of the method used to reject conversions. The third background, electron from c -quarks, are difficult to estimate. The method to estimate this background is described in the next chapter.

In this chapter, we describe how to estimate the non-heavy quark backgrounds, hadrons faking electrons and photon conversions.

4.1 Hadrons faking electrons

The electron quality cuts which we have applied to the data mainly use the shower shape of the electrons and thus it is effective for removing the events with multi-photon and hadron overlapping. However, this method has a difficulty to remove the hadrons faking electrons because the shower shape

of those hadrons is similar to that of the real electrons. In order to estimate the fraction of those hadrons, we use the CPR charge distribution. At first we make the templates for real electrons and hadrons using the control samples as described below.

4.1.1 Control sample for CPR templates

Real electron sample

A real electron sample is made from a sample of events with photon conversion identified using the conversion finding method as described in Sec. 3.1.3. We apply the following selection criteria to make this sample:

- Apply all electron identification cuts shown in Table 3.1, except for the requirements of CPR, conversion rejection and SVX hit
- Identify a conversion using the conversion finding method: $|\delta S| < 0.2(\text{cm})$ and $|\delta \cot \theta| < 0.06$
- Require the conversion to occur in the CTC inner wall: $30 > R_{e^+e^-} > 20 \text{ cm}$
- Require the measured Q_{CTC} (see Sec. 2.2) for the conversion partner track to be larger than the predicted value for an electron track by one sigma
- $VTX_{occ} < 0.2$

The CPR distribution for this “pure” electrons are shown in Fig. 4.1(a). In order to parameterize the distribution, we fit this distribution to the following empirical function:

$$f(x) = P_1 x^{P_2} \exp [P_3 x^{P_4}] + \frac{P_5}{P_7} \exp \left[-\frac{1}{2} \left(\frac{x - P_6}{P_7} \right)^2 \right].$$

The obtained fit function is used as a template for the real electrons.

Hadron-rich sample

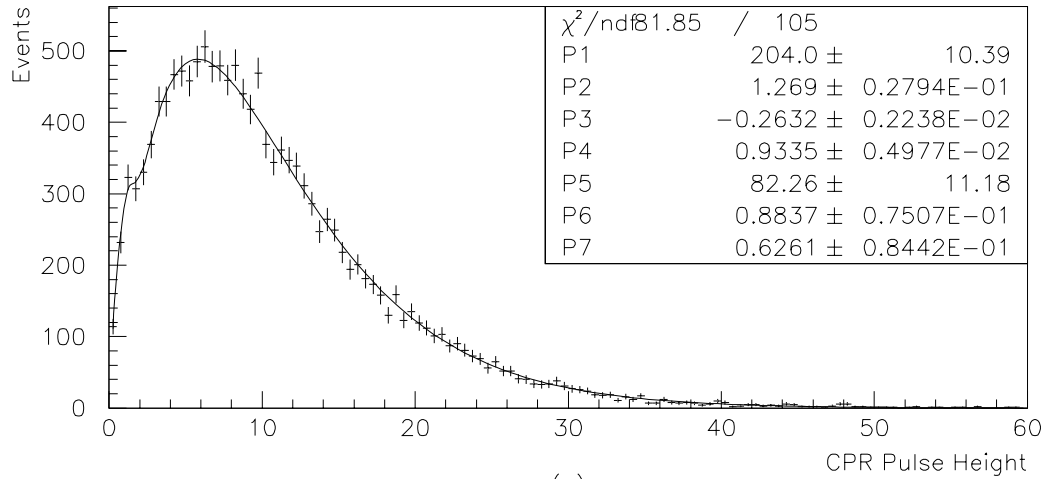
A hadron-rich sample is selected by removing the events satisfying the HAD/EM requirement for electron selection in Table 3.1. We assume that the energy deposition of hadrons in the CPR can be fitted to a Landau distribution since the CPR is a gas proportional chamber. We fit the hadron-rich sample to a Landau distributions plus the electron template. We practically use a sum of two Landau distributions to make a better fit. The fit results are shown in Fig. 4.1(b). The sum of two Landau distribution is used as a template for the hadrons faking electrons.

4.1.2 Results of CPR fit

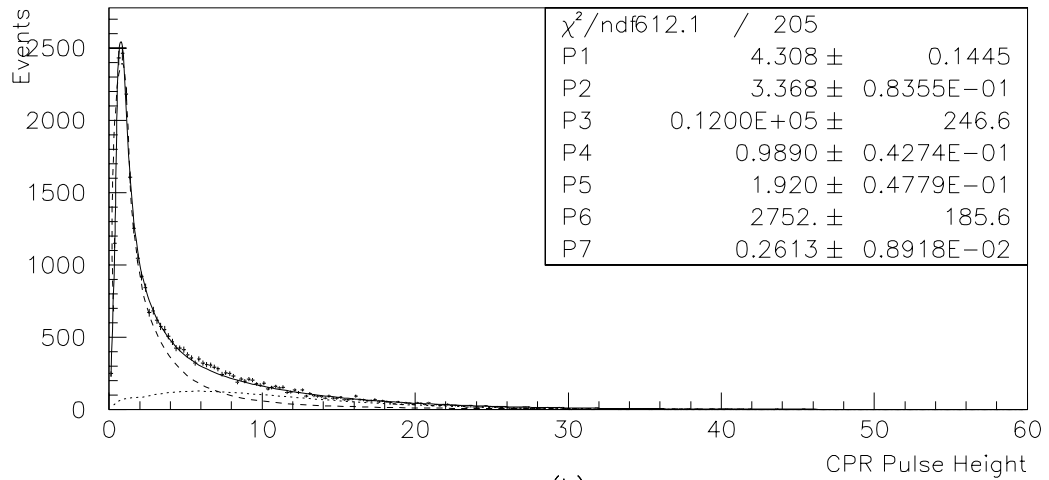
The amount of the hadrons faking electrons in the whole electron sample is estimated by fitting the CPR charge distribution to the sum of electron and hadron templates. The CPR charge cut listed in Table 3.1 is not applied to this sample. The fit results for the whole electron sample and the diffractive candidates are shown in Fig. 4.2 and Fig. 4.3, respectively. The hadron fraction of the sample after applying the CPR charge cut is calculated using the cut efficiency for hadrons and electrons, 46% and 93%. We obtain the hadron fraction of $25.8 \pm 0.2(\text{stat}) \pm 0.6(\text{syst})\%$ for the whole electron sample, and $30.4 \pm 5.1(\text{stat}) \pm 0.8(\text{syst})\%$ for the diffractive candidates. The systematic uncertainty is estimated by changing the template shapes according to their uncertainties.

4.2 Photon conversion electrons

The method to reject the photon conversion events is based on finding the partner track of the trigger electron. Once the conversion finding efficiency



(a)



(b)

Figure 4.1: (a) The CPR charge distribution of the control sample for the real electrons. (b) The CPR charge distribution of the control sample for the hadron-rich events.

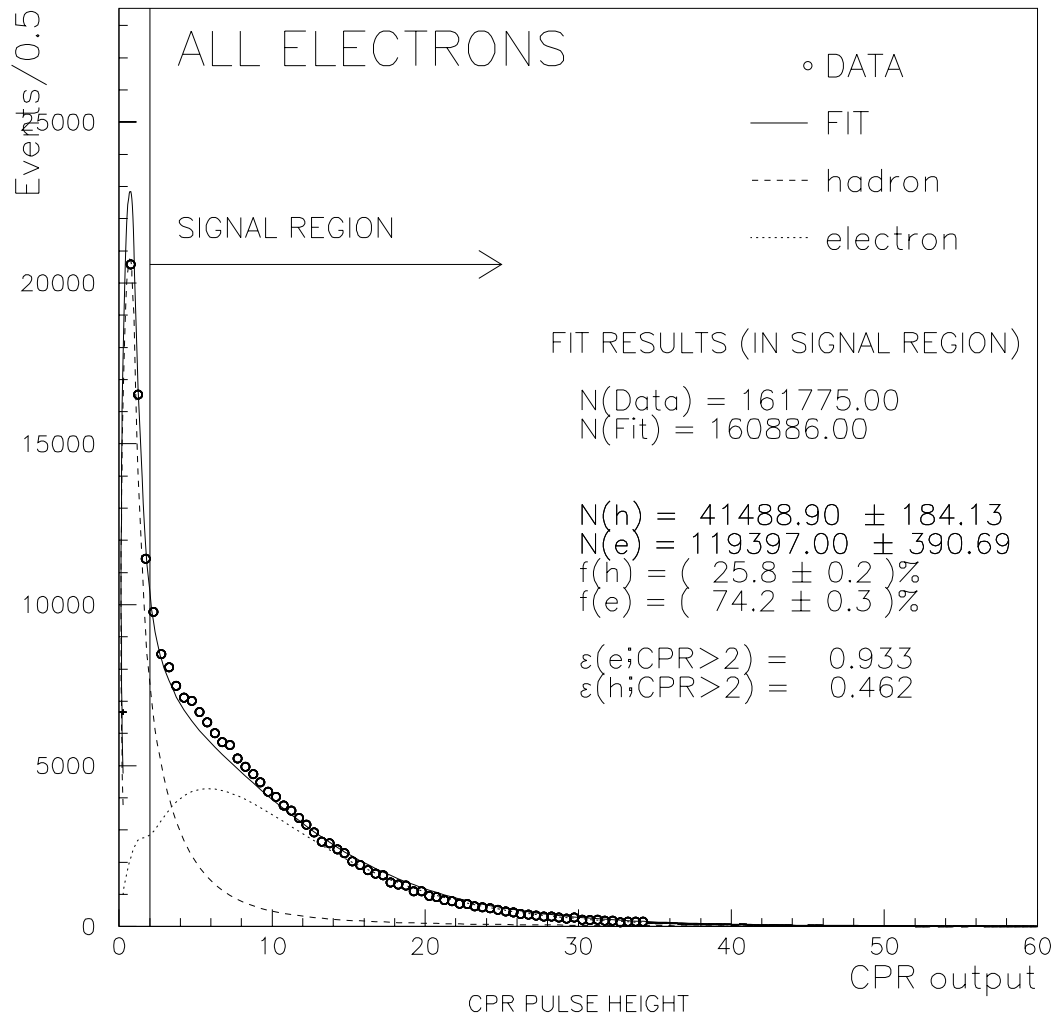


Figure 4.2: The CPR charge distribution for the whole electron sample. Open circle represents the CDF data. The solid curve shows the fit to a sum of the two templates, the electron (dotted) and the hadron (dashed).

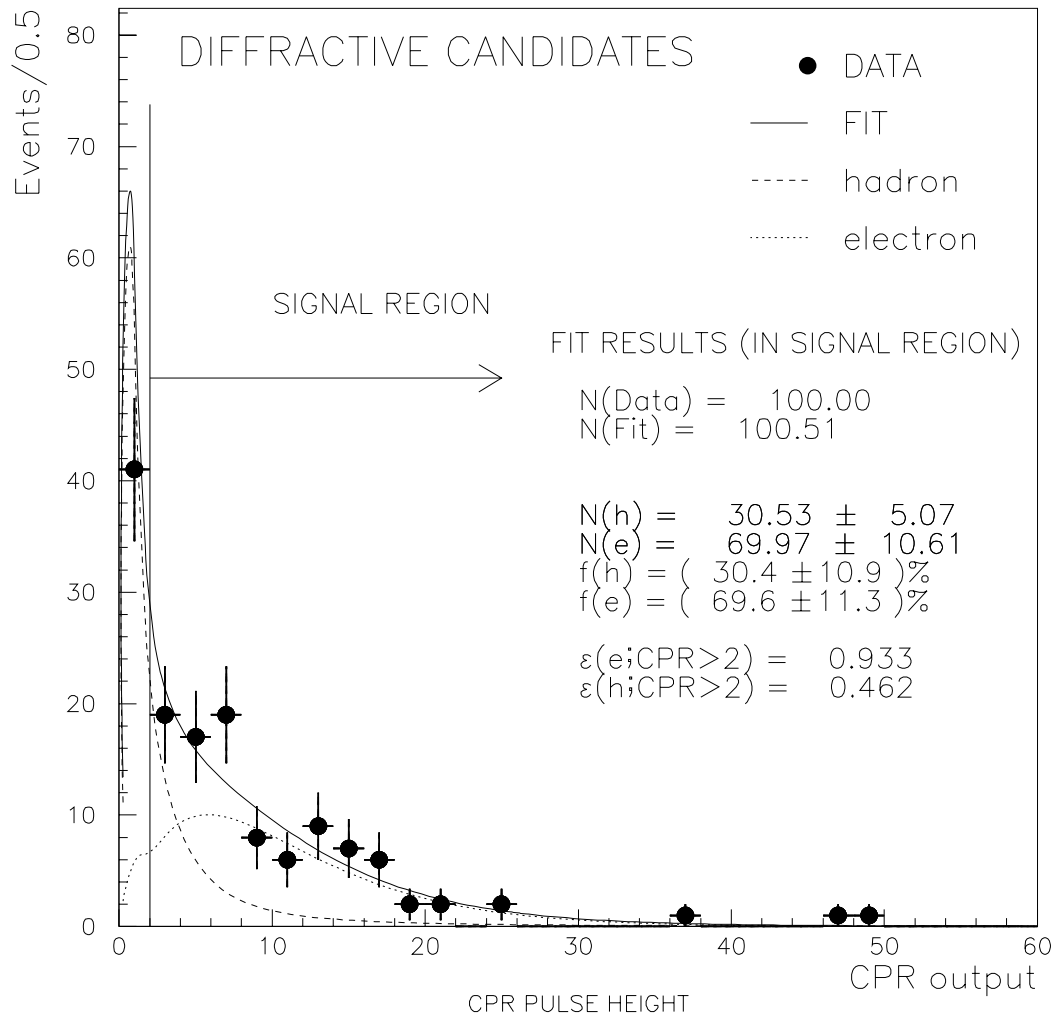


Figure 4.3: The CPR charge distribution for the diffractive candidates. The solid circle represents the CDF data. The solid curve shows the fit to a sum of the two templates, the electron (dotted) and the hadron (dashed).

is known, the residual number of the conversions is calculated by,

$$N_{conv}^{resid} = (1 - \varepsilon_{conv}) \times \frac{P \times N_{conv}^{tag}}{\varepsilon_{conv}} \quad (4.1)$$

where ε_{conv} is the conversion finding efficiency, N_{conv}^{tag} is the number of conversions tagged by the method and P is a fraction of the conversions.

In the following sections, we describe the conversion finding efficiency and the estimation of the residual conversion in the sample.

4.2.1 Conversion finding efficiency

The conversion finding efficiency is studied using the control sample obtained by the VTX occupancy method. The VTX occupancy method identify conversion electrons created outside the VTX (“outside-conversion”). So this method is independent of the conversion finding method described in the preceding section. The “outside-conversion” leaves no tracks in the VTX and thus the VTX_{occ} become low. We select those kind of conversions by requiring the VTX_{occ} to be less than 0.2 and also required no SVX hit for the track to ensure the outside-conversion.

The conversion fraction in this sample is measured using the CPR charge distribution. The CPR distribution for the VTX conversion sample is shown in Fig. 4.4. We categorize this sample into two components: (i) outside-conversions correctly tagged with the VTX and (ii) any events accidentally tagged with the VTX. Assuming that a probability of the accidental tagging is independent of a physical process which produces a trigger electron, we use the CPR distribution for the VTX-untagged events as the accidental tagging component. In order to estimate the fraction of correctly tagged conversions, we fit the CPR distribution with a sum of the two templates, real electron and untagged events. The fit results are also shown in Fig. 4.4. The CPR fit yields that the fraction of real conversion in this sample is 93%. We further

apply a tighter CPR requirement ($\text{CPR} > 6.0$) to this sample and obtain the control sample of outside-conversions with 95% purity.

Estimation from tagging rate

The conversion finding method tags $79.5 \pm 1.0\%$ of the conversions in the control sample. Thus the conversion finding efficiency is found as $\varepsilon^{\text{conv}} = 79.5 \pm 1.0(\text{stat})\%$. The starting point of the conversion pair is obtained with the conversion finding method as shown in Fig. 4.5 in the radial coordinate. A peak around the radius of 20~30 cm corresponds to conversions occurring in the wall between the CTC and the VTX as expected from the method to make this sample.

Estimation from ε^{trk} and ε^{cut}

The efficiency of the conversion finding method is also estimated with a different approach using the same control sample. We divide the efficiency into two factors, the efficiency of the CTC to accept the partner track ($=\varepsilon^{\text{trk}}$) and the efficiency of the topological cut used in the algorithm ($=\varepsilon^{\text{cut}}$).

In order to estimate the tracking efficiency ε^{trk} , we plot the p_T spectrum of the partner track as shown in Fig. 4.6. We further require the radial conversion point to be in the CTC wall ($20 < R_{e+e-} < 30\text{cm}$) to increase a purity. A lack of events in a low momentum region below $\sim 400 \text{ MeV}/c$ is due to the limited acceptance of the CTC for low momentum particles. We fit the distribution to an exponential function in the p_T range of $0.5 < p_T < 3.0 \text{ GeV}/c$ to determine the number of events lack in the p_T region below $0.5 \text{ GeV}/c$. The tracking efficiency obtained by the fit is $\varepsilon^{\text{trk}} = 81.0 \pm 0.7\%$.

In order to estimate the topological cut efficiency ε^{cut} , we select conversion partner tracks with sufficiently high p_T for the reconstruction in the CTC ($p_T > 0.5 \text{ GeV}/c$). The distributions of δS and $\delta \cot \theta$ used in the conversion finding method are shown in Figs. 4.7(a) and (b). The topological

cut efficiency is $\varepsilon^{cut}=94.7\pm 0.9\%$. By multiplying the above two efficiencies, ε^{trk} and ε^{cut} , the total efficiency of the conversion finding method is found as $\varepsilon^{conv} = 76.7\pm 1.0(\text{stat})\%$.

Combined results

The agreement between the two estimations are fairly well. However, in the second estimation we assumed that the partner track p_T distribution has an exponential for without any proof. Therefore we used the first estimation and take the difference between the two estimations for the systematic uncertainty. The conversion finding efficiency is $\varepsilon^{conv} = 79.5 \pm 1.0(\text{stat}) \pm 2.7(\text{syst}) \%$.

4.2.2 Residual conversions

Purity of the conversion-tagged sample

We have 161775 electrons in the whole electron sample after rejecting 25630 electrons as conversions using the conversion finding method. In order to estimate the residual conversions, we study the purity of the conversions tagged by the conversion finding method. The CPR distribution is used to estimate the purity of the conversions in the same way as described in the previous section by assuming that the accidental tagging probability is independent of the physical process. We thus fit the CPR distribution for the conversion-tagged sample with a sum of the two templates: (i) electrons as correctly tagged conversions and (ii) conversion-untagged sample as accidentally tagged events. The CPR distribution is shown together with a fit curve in Fig. 4.8. The fit yields 19092 ± 284 conversions in the 25630 tagged events. The purity of the conversion tagged sample is $74.5\pm 1.2\%$.

```

MINUIT  $\chi^2$  Fit to Plot    10109&0
CPR (low VTX )
File: conv_tes_hipt.hbk
Plot Area Total/Fit  36617. / 36617.
Func Area Total/Fit 36550. / 36550.
8-OCT-98 21:50
Fit Status 3
E.D.M. 7.115E-08
 $\chi^2 = 92.5$  for 120 - 2 d.o.f.,
C.L. = 96.0%
Errors
Parabolic
Minos
Function 1: Histogram  100  0 Normal errors
NORM          33995.     $\pm 354.3$     - 353.6    + 355.0
Function 2: Histogram  200  0 Normal errors
NORM          2555.2     $\pm 291.1$     - 291.4    + 290.8

```

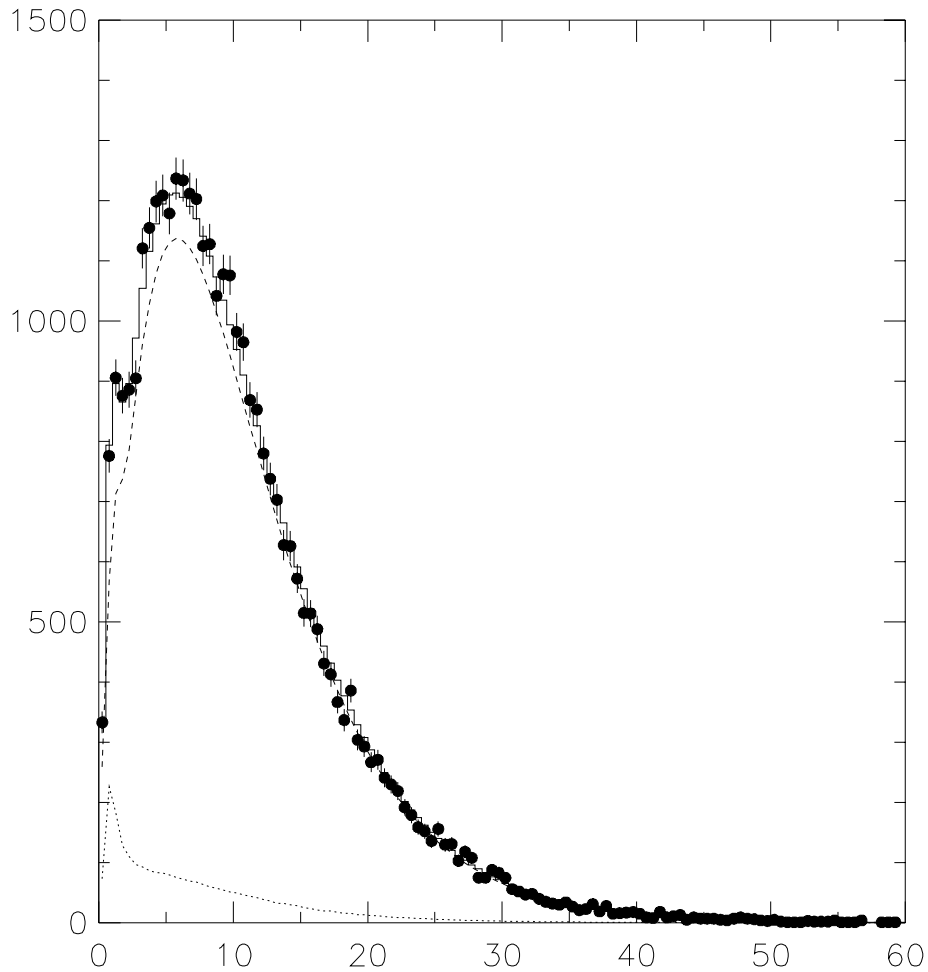


Figure 4.4: The CPR charge distribution for the VTX tagged conversion sample overlaid with the fit result. The dashed curve shows the contribution of pure conversion events. The dotted curve shows the contribution of accidentally tagged events.

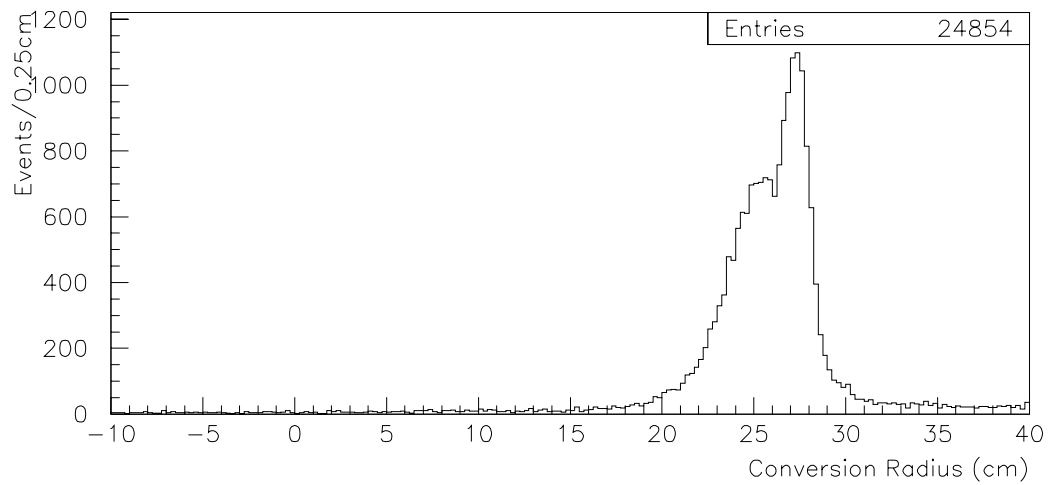


Figure 4.5: The radius where the conversion occurs in the detector. A peak corresponds to the thick material which forms the wall of the VTX and the CTC.

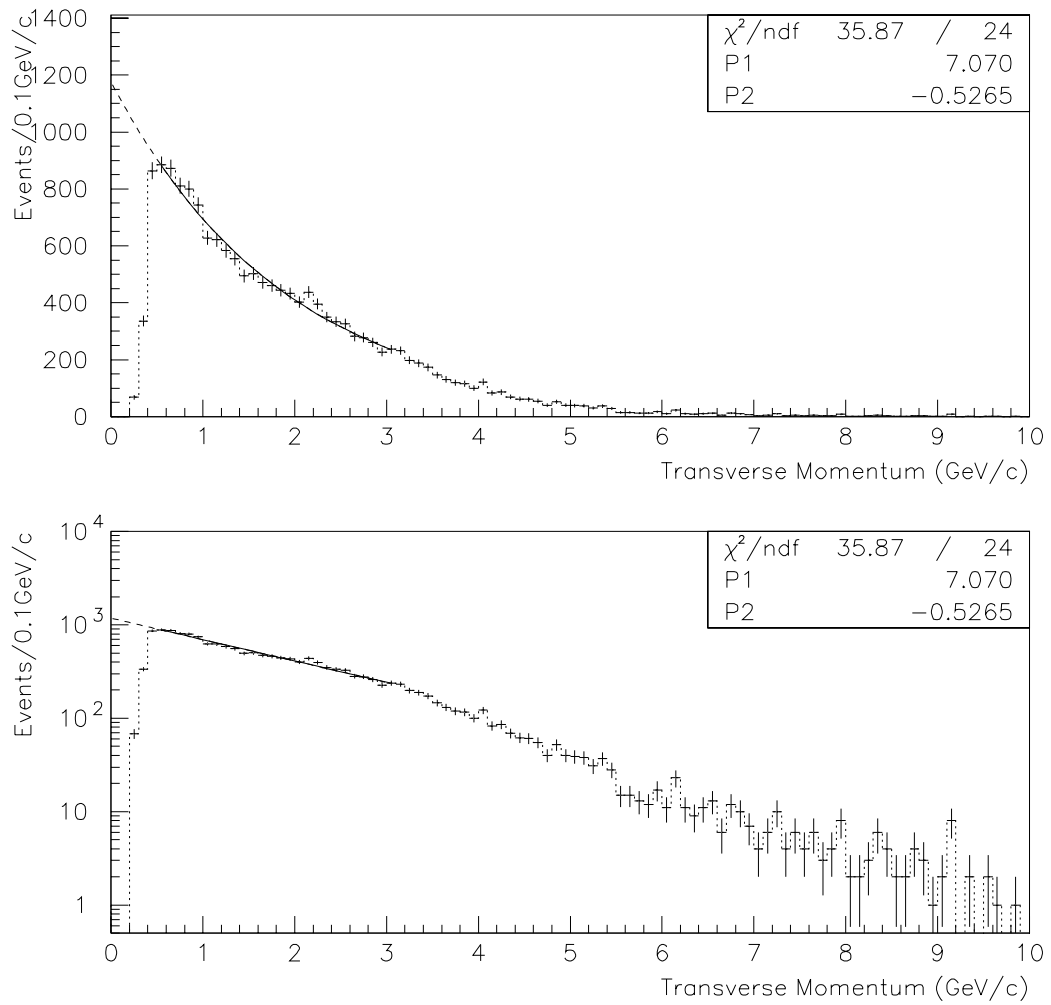


Figure 4.6: Transverse momentum of the conversion partner track.

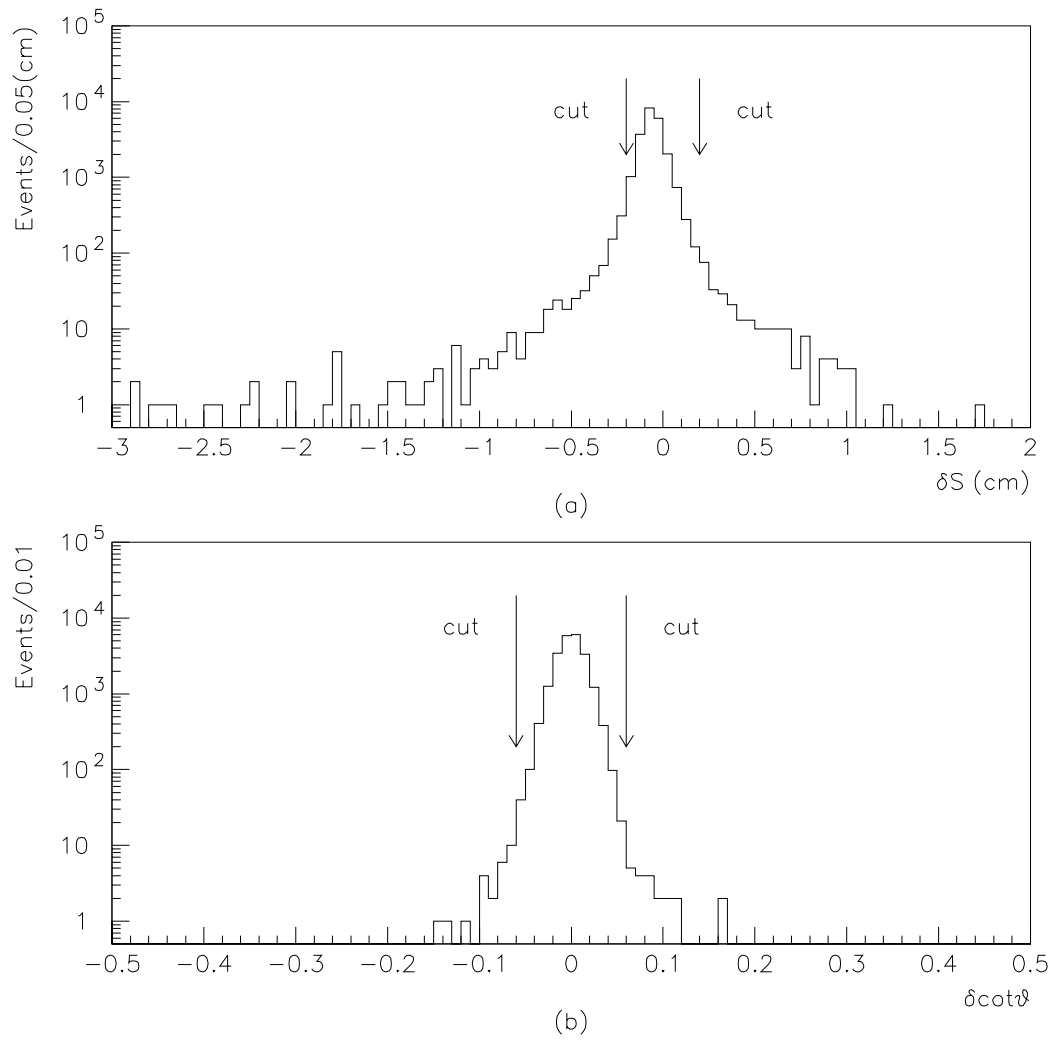


Figure 4.7: Distribution of the cut variable for conversion rejection. (a) separation of the two trajectory in the r - ϕ plane. (b) $\delta \cot \theta$ of the two track.

Residual conversions in the whole electron sample

The number of residual conversions are calculated with Eq. 4.1.

$$\begin{aligned} N_{conv}^{resid}(all) &= (1 - \varepsilon_{conv}) \times \frac{P \times N_{conv}^{tag}(all)}{\varepsilon_{conv}} \\ &= (1 - (0.795 \pm 0.029)) \times \frac{(0.745 \pm 0.012) \times 25630}{0.795 \pm 0.029} \\ &= 4924 \pm 172 \text{ events.} \end{aligned}$$

This results in a fraction of residual conversions of $3.0 \pm 0.1(\text{stat} + \text{syst})\%$.

Residual conversions in the diffractive candidates

We have 100 electrons in the diffractive candidates, after rejecting 11 electrons as conversions using the conversion finding method. In order to calculate the number of residual conversions in the diffractive candidates, we use the same conversion efficiency and purity as in the whole electron sample. The number of residual conversions in the diffractive candidates is $2.1 \pm 0.7(\text{syst} + \text{stat})$ events. The corresponding fraction in the diffractive candidates is $2.1 \pm 0.7(\text{syst} + \text{stat})\%$.

```

MINUIT  $\chi^2$  Fit to Plot    10309&0
CPR ( $\gamma$ w/oCPR)
File: tes_hipt.hbk
Plot Area Total/Fit  29163. / 29163.
Func Area Total/Fit  29088. / 29088.
 $\chi^2 = 93.5$  for 120 - 2 d.o.f.,
Errors      Parabolic      Minos
Function 1: Histogram  100  0 Normal errors
NORM      20463.         $\pm 304.6$    - 304.4   + 304.8
Function 2: Histogram  200  0 Normal errors
NORM      8624.4        $\pm 278.9$    - 278.9   + 279.0
7-OCT-98 21:02
Fit Status 3
E.D.M. 2.460E-07
C.L. = 95.3%

```

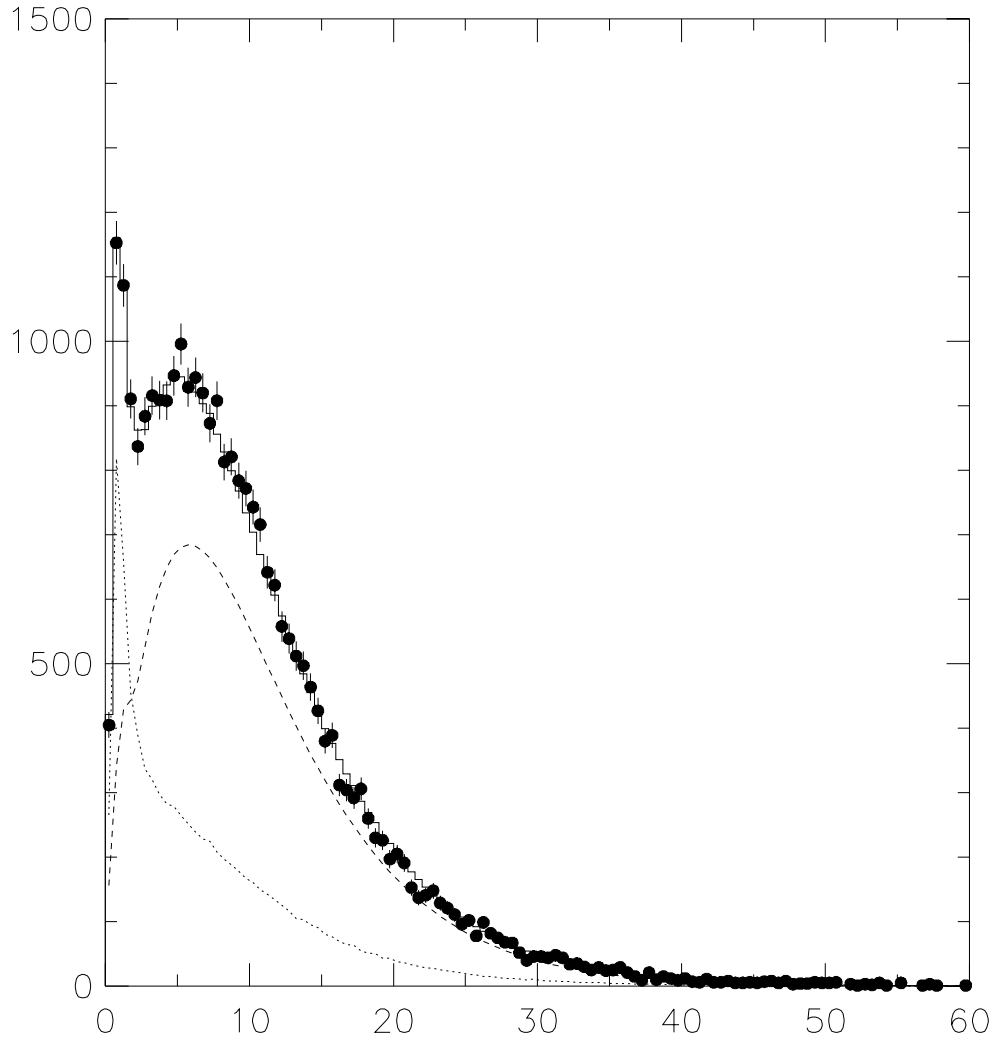


Figure 4.8: The CPR charge distribution for the conversions rejected from the whole electron sample. The fit result is overlaid. The dashed curve shows a contribution of correctly tagged conversions. The dotted curve shows a contribution of accidentally tagged events.

Chapter 5

Determination of $b\bar{b}$ event fraction

The amount of $b\bar{b}$ events in the data sample is estimated using the p_T^{rel} and the impact parameter distributions. Both distributions are fitted to a four components sum of the hadron, the conversion, the $c\bar{c}$ and the $b\bar{b}$ templates. The results described the previous chapter are used as constraints on non-heavy flavor background fraction when we make this fit.

In this chapter, we started with the control samples to obtain the templates for the fit of the p_T^{rel} and the impact parameter distributions.

5.1 Control samples for p_T^{rel} and impact parameter fit

Monte Carlo sample for $b\bar{b}$ and $c\bar{c}$

In order to obtain the templates for the $b\bar{b}$ and $c\bar{c}$ events, we use the PYTHIA 5.7 Monte Carlo simulator. We use the tuned PYTHIA 5.7 which was modeled to reproduce the underlying multiplicity of $l + D^0$ sample [31]. The b -quarks and c -quarks are generated with p_T above 12 GeV/ c so as to produce a high p_T electron through its decay. In order to reduce the CPU time for the event generation, both b and c quarks are forced to decay into an electron plus anything with the QQ Monte Carlo program which deal with b and c hadron

decays developed by the CLEO group [32]. The \bar{b} and \bar{c} quarks generated at the same time are not forced so as to keep the right branching ratio of their decay. A generator-level filter simulates the effect of the Level-2 trigger. The following p_T dependent trigger efficiency is used in the trigger simulation,

$$\epsilon(p_T) = 0.927 \times F\left(\frac{p_T - 6.18}{4.20}\right) \times F\left(\frac{p_T - 7.48}{0.504}\right).$$

where F represents the normal frequency function,

$$F(x) = \frac{1}{\sqrt{2\pi}} \int_{-\infty}^x e^{-\frac{1}{2}t^2} dt.$$

The kinematical cuts of $p_T > 8$ GeV/ c and $|\eta| < 1.2$ are also applied to the electron in the generator-level filter. The events satisfying the generator level selection are processed by the fast CDF detector simulation (QFL). After the detector simulation, the Monte Carlo events are treated as if they were real data. Finally the events passing the selection criteria composes the samples for the $b\bar{b}$ and the $c\bar{c}$ events.

Sequential $b \rightarrow c \rightarrow e$ decay

The real data contains not only the electrons from direct $b \rightarrow e$ decays but also the electrons from sequential $b \rightarrow c \rightarrow e$ decays. The fraction of sequential $b \rightarrow c \rightarrow e$ decays in the electron sample is studied using the Monte Carlo simulation without forcing to the semi-leptonic decay. Table 5.1 gives the fractions of electrons from the direct $b \rightarrow e$ decay and the sequential $b \rightarrow c \rightarrow e$ decays.

The fraction of sequential $b \rightarrow c \rightarrow e$ decays in all $b\bar{b}$ events is found to be $4.5 \pm 0.4\%$ (*stat*). We use this event fraction to make the more precise template for the $b\bar{b}$ events than with only the direct $b \rightarrow e$ decays.

In order to generate the sequential $b \rightarrow c \rightarrow e$ decay events, we force all c hadrons with the parent of the b hadrons to decay semileptonically. The event sample of this sequential $b \rightarrow c \rightarrow e$ decay is obtained in the same way as stated above.

<i>b</i> -hadrons	B^\pm	B^0	B_s	Λ_b	—
$95.5 \pm 0.2(\%)$	38.0 ± 1.3	40.4 ± 1.3	8.8 ± 0.6	8.4 ± 0.5	—
<i>c</i> -hadrons	D^\pm	D^0	J/ψ	D_s	Λ_c
$4.5 \pm 0.4(\%)$	1.5 ± 0.2	1.3 ± 0.2	1.1 ± 0.2	0.5 ± 0.1	0.1 ± 0.1

Table 5.1: Sources of the trigger electron in the $b\bar{b}$ Monte Carlo simulation data.

Hadron sample with a SVX track

A hadron sample with a SVX track is selected with the following selection criteria:

- Apply all electron identification cuts shown in Table 3.1 except for the requirements of the HAD/EM and the CPR
- HAD/EM > 0.04 for one track or HAD/EM > 0.10 for more than one track
- CPR charge < 2.0
- (Energy measured in the CES strip)/p < 0.5
- Require the measured Q_{CTC} for the track to be smaller than the predicted value for electron

Photon conversion sample with a SVX track

A photon conversion sample with a SVX track is selected with the following selection criteria:

- Apply all electron identification cuts shown in Table 3.1 except for the requirements of the conversion rejection
- Identify a conversion using the conversion finding method: $|\delta S| < 0.2(\text{cm})$ and $|\delta \cot \theta| < 0.06$

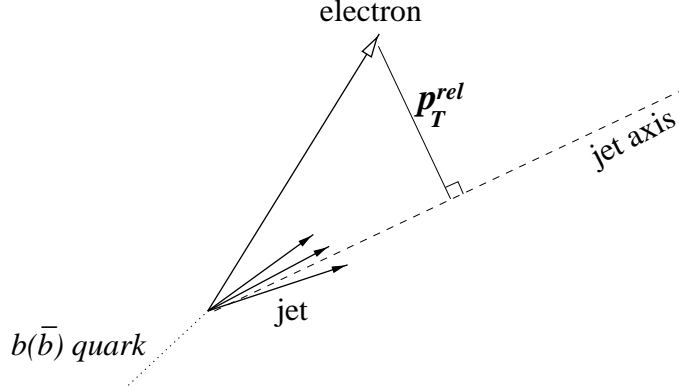


Figure 5.1: Definition of the p_T^{rel} .

- Require the measured Q_{CTC} for the conversion partner track to be larger than the predicted value for electron by one sigma

5.2 Results of p_T^{rel} fit

The p_T^{rel} is the transverse momentum of the electron relative to the associating jet axis as shown in Fig. 5.1. It clearly reflects the mass of the parent particle. The jet is reconstructed using the track information with the CTC using the algorithm described in Sec. 3.1.1. In the p_T^{rel} calculation, the associating jet axis is determined by subtracting the electron momentum vector from the jet momentum vector so as to define the jet excluding the electron.

The p_T^{rel} templates of $b\bar{b}$, $c\bar{c}$, hadron fakes and conversions are made using the samples described in the previous section. Figures 5.2(a)-(d) show the p_T^{rel} distributions for the samples. The templates are obtained by fitting the distributions to the following empirical function [33],

$$f(x) = P_1 x^{P_2} \exp [P_3 x^{P_4}] + \frac{P_5}{P_7} \exp \left[-\frac{1}{2} \left(\frac{x - P_6}{P_7} \right)^2 \right].$$

The templates for the $b\bar{b}$ events shown in Fig. 5.2(d) are obtained by studying the two kinds of the b -quark decay modes, the direct $b \rightarrow e$ decay and the sequential $b \rightarrow c \rightarrow e$ decay. The p_T^{rel} distributions of the direct $b \rightarrow e$

decay and the sequential $b \rightarrow c \rightarrow e$ decay are shown in Figs. 5.3(a) and (b). The distribution for the sequential $b \rightarrow c \rightarrow e$ decay shows softer spectrum than for the direct $b \rightarrow e$ decay. We mix both templates for the direct and sequential decays with a ratio of 95.5:4.5 to obtain the whole $b\bar{b}$ event templates as shown in Fig 5.2(d).

We fit the p_T^{rel} distribution for the whole electron sample to a sum of the templates for the $b\bar{b}$, $c\bar{c}$, conversion and hadron with the maximum binned likelihood method described in Appendix D.1. In the likelihood function, Gaussian terms are introduced to constrain the contribution of the conversions and hadron faking electrons according to the results of the independent analysis described in the previous chapter. The p_T^{rel} distribution for the whole electron sample is shown in Fig. 5.4 together with a fitted curve. The fit yields the $b\bar{b}$ fraction of $42.9 \pm 0.4(\text{stat})\%$ for the whole electron sample.

The p_T^{rel} distribution for the diffractive candidates is also fitted to a sum of the four templates with the maximum likelihood method (Appendix D.2). The Gaussian terms are also introduced to constrain the contribution of the conversions and hadron faking electrons. The p_T^{rel} distribution for the diffractive candidates is shown in Fig. 5.5 together with a fitted curve. We obtain $38.1 \pm 13.5(\text{stat}) b\bar{b}$ events in 100 diffractive candidates by this fit.

The fit results of the p_T^{rel} distribution are summarized in Tables 5.2 and 5.3.

	hadron	conversion	$c\bar{c}$	$b\bar{b}$
input from CPR and ε_{conv}	41489±1063 (25.6±0.7)%	4924±172 (3.0±0.1)%	— —	— —
outputs	43554±931* (27.0±0.6)%*	5000±168* (3.1±0.1)%*	43668±726 (27.1±0.4)%	69165±724 (42.9±0.4)%

Table 5.2: The number of hadron faking electrons, photon conversion, $c\bar{c}$ and $b\bar{b}$ events in the **whole electron sample** obtained with the p_T^{rel} distribution fit. *Fit is constrained to the inputs.

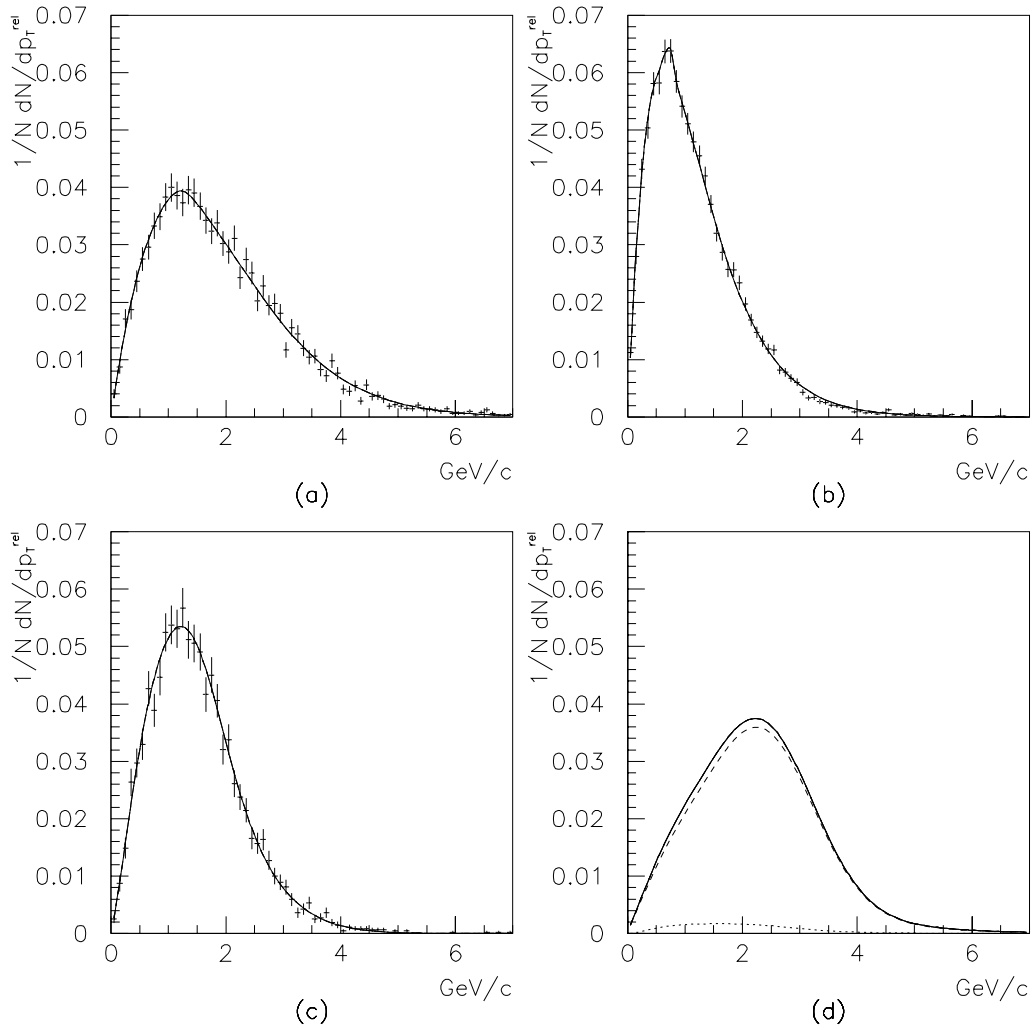
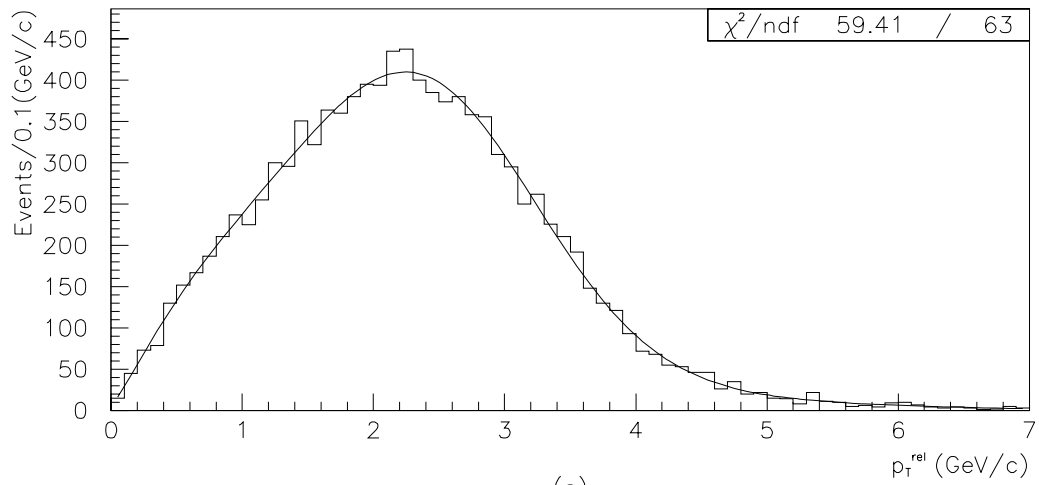
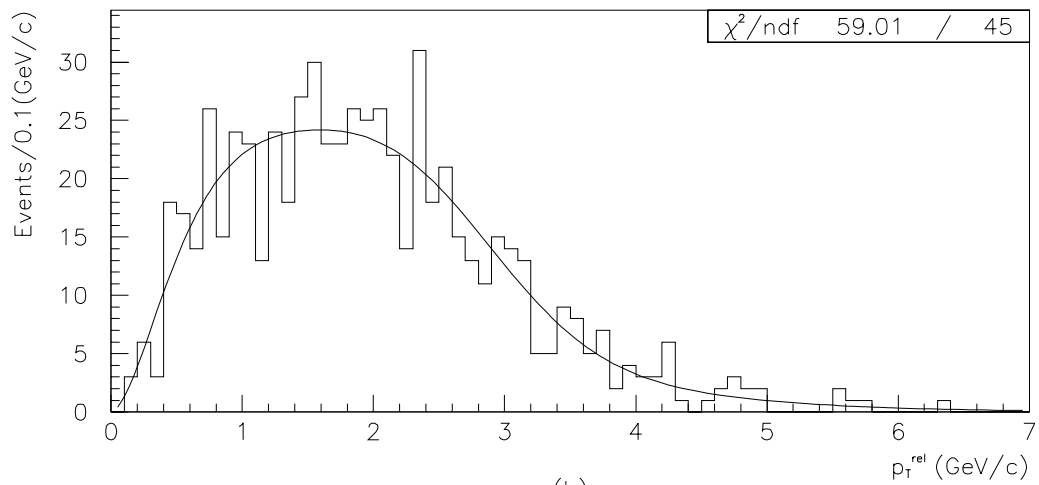


Figure 5.2: The p_T^{*el} distribution for (a) hadron faking electrons, (b) photon conversions, (c) $c\bar{c}$ Monte Carlo, and (d) $b\bar{b}$ Monte Carlo (dashed curve:direct $b \rightarrow e$ decays, dotted curve:sequential $b \rightarrow c \rightarrow e$ decays).



(a)



(b)

Figure 5.3: The p_T^{rel} distribution for the Monte Carlo samples. (a) Direct $b \rightarrow e$ decays (b) Sequential $b \rightarrow c \rightarrow e$ decays

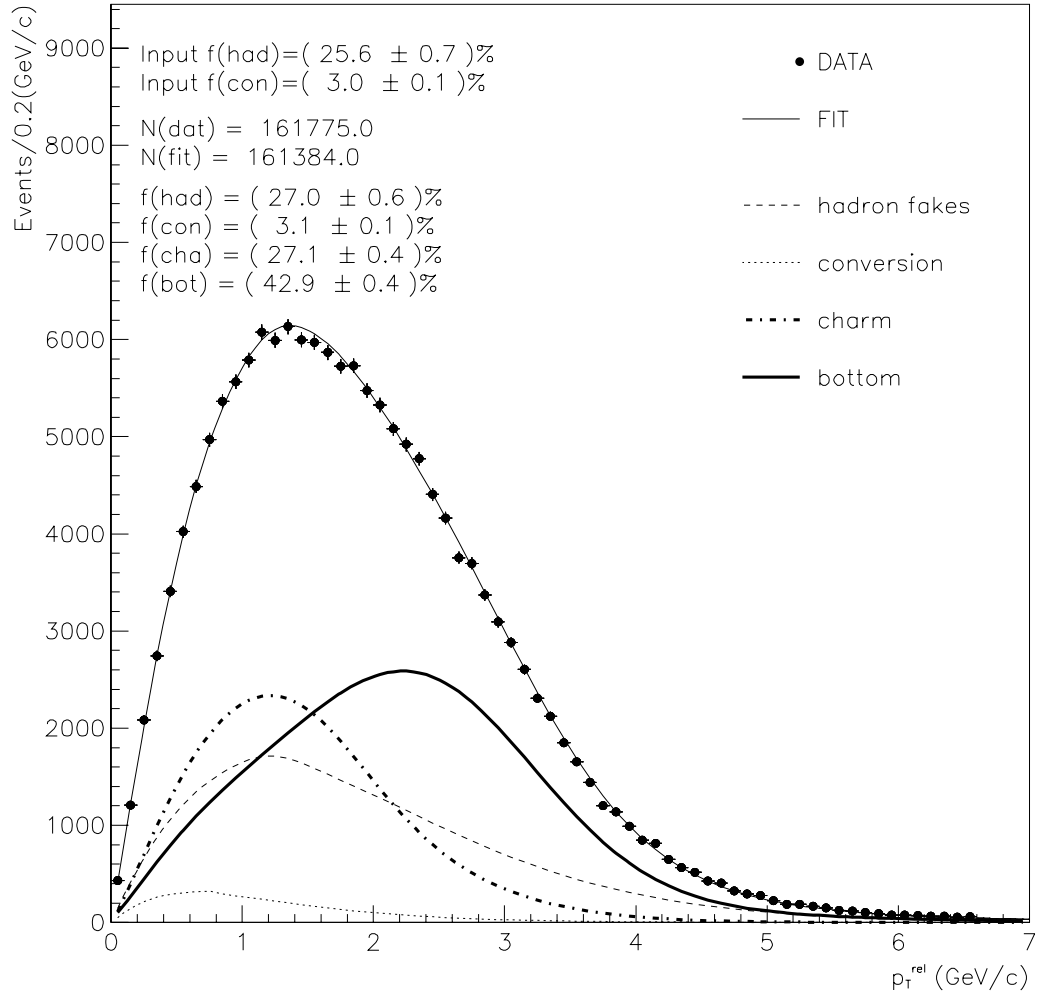


Figure 5.4: The p_T^{rel} distribution for the whole electron sample. The results of the four-component fit are also shown. Dashed curve shows hadron faking electrons, dotted curve shows conversions, thick dashed curve shows $c\bar{c}$ and thick solid curve shows $b\bar{b}$.

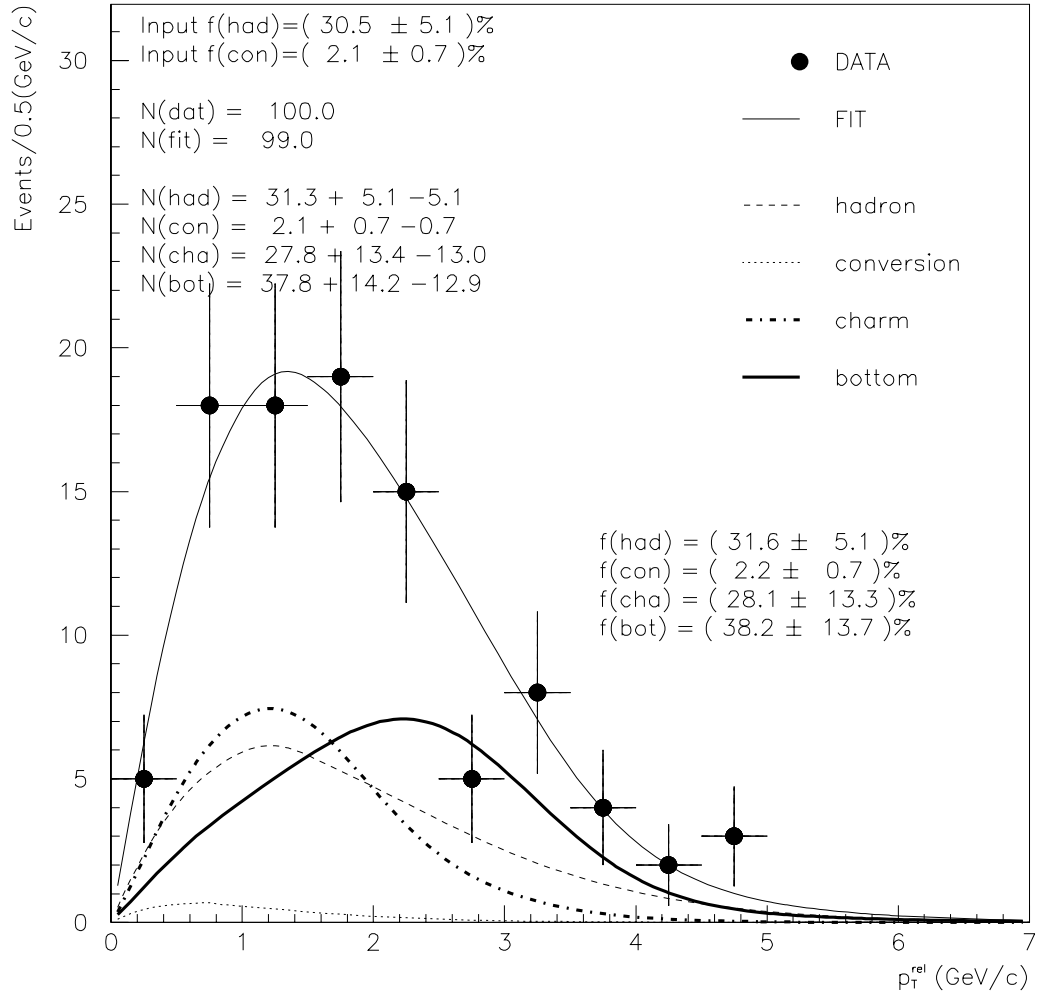


Figure 5.5: The p_T^{rel} distribution of the diffractive candidates. The results of the four-component fit are also shown. Dashed curve shows hadron faking electrons, dotted curve shows conversions, thick dashed curve shows $c\bar{c}$ and thick solid curve shows $b\bar{b}$.

	hadron	conversion	$c\bar{c}$	$b\bar{b}$
inputs from CPR and ε_{conv}	30.5 ± 5.1 (30.5 ± 5.1)%	2.1 ± 0.7 (2.1 ± 0.7)%	— —	— —
outputs	$31.3\pm 5.1^*$ (31.6 ± 5.1)%*	$2.1\pm 0.7^*$ (2.2 ± 0.7)%*	27.8 ± 13.2 (28.1 ± 13.3)%	37.8 ± 13.6 (38.2 ± 13.7)%

Table 5.3: The number of hadron, conversion, $c\bar{c}$ and $b\bar{b}$ events in the **diffractive candidates** obtained with the p_T^{rel} distribution fit. *Fit is constrained to the inputs.

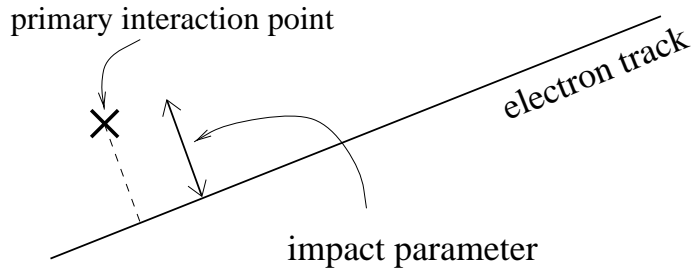


Figure 5.6: Definition of the impact parameter.

5.3 Results of impact parameter fit

The impact parameter is defined as a minimum distance between a primary vertex and the electron track in a r - ϕ plane as shown in Fig. 5.6.

The impact parameter reflects the mass and the lifetime of the parent particle according to the following expression [34];

$$\delta = \frac{c\tau_b}{k}, \quad k \equiv \frac{1 + \beta \cos \theta^*}{\beta \sin \theta^*}$$

where $c\tau_b$ is a proper decay length of the parent particle, β is a velocity of the parent particle and θ^* is an angle in space between the direction of the parent particle and the electron track in the rest frame of the parent particle.

The impact parameter distribution for each control sample is shown in Figs. 5.7(a)-(d).

The template for the hadrons faking electrons is obtained by fitting the impact parameter distribution for the hadron sample to a sum of two func-

tions, Gaussian and exponential.

$$f(x) = P_1 \frac{2}{\sqrt{2\pi}P_2} \exp \left[-\frac{1}{2} \left(\frac{x}{P_2} \right)^2 \right] + P_3 e^{P_4 x}$$

Since most hadrons are produced directly at a primary interaction point, the impact parameter distribution for the hadrons can be fit to a Gaussian function which represents a detector resolution for the measurement. The exponential function represents a small contamination of electrons from heavy flavor decay in the hadron sample. Only the Gaussian term is used for a template for hadrons. We also use this Gaussian as a resolution function to make templates for the $b\bar{b}$ and $c\bar{c}$ events as described below.

The impact parameter distribution for the conversion sample is parameterized by

$$f(x) = P_1 \frac{1}{\sqrt{2\pi}P_2} \exp \left[-\frac{1}{2} \left(\frac{x}{P_2} \right)^2 \right] + P_3 e^{P_4 x} + P_5 e^{P_6 x}.$$

The Gaussian term is a resolution function for the electrons from π^0 Dalitz decay. The exponential terms comes from the conversion electrons produced in the material inside the detector.

In order to obtain the templates for electrons from heavy flavor decay, we perform the following steps. At first we parameterize the impact parameter distribution for the sample at a generator level. Next we smear the fit function according to the resolution function measured for the hadron sample.

Figures 5.8(a)-(c) show the impact parameter distributions for the Monte Carlo sample of the direct $b \rightarrow e$ decays, the sequential $b \rightarrow c \rightarrow e$ decays and the $c\bar{c}$ events at a generator level. These distributions are parameterized by

$$f(x)_{gen} = P_1 e^{P_2 x} + P_3 e^{P_4 x} (+P_5 e^{P_6 x})$$

where the last term is only used for the $b \rightarrow e$ sample. The $b\bar{b}$ template is made by adding the direct and sequential decay samples with a ratio of 95.5:4.5. Final templates for the $c\bar{c}$ and $b\bar{b}$ events are made by smearing the parameterized functions using the resolution function.

We fit the impact parameter distribution for the whole electron sample to a sum of the above templates with a maximum binned likelihood method described in Appendix D.1. In the likelihood function, Gaussian terms are introduced to constrain the contribution of the conversions and hadron faking electrons in the same way as in the p_T^{rel} fit. The impact parameter distribution for the whole electron sample is shown in Fig. 5.9 together with a fitted curve. The fit yields the $b\bar{b}$ fraction of $47.7 \pm 0.4\%$ in the whole electron sample.

The impact parameter distribution for the diffractive candidates is fitted to a sum of above templates with a maximum likelihood method described in Appendix D.2. The contributions of conversions and hadrons are also constrained to the results described in Chapter 4. The fit yields $50.7 \pm 14.9(\text{stat})$ $b\bar{b}$ events in 100 diffractive candidates.

The fit results of the impact parameter distribution are summarized in Tables 5.4 and 5.5.

	hadron	conversion	$c\bar{c}$	$b\bar{b}$
inputs from CPR and ε_{conv}	41489 ± 1063 ($25.6 \pm 0.7\%$)	4924 ± 172 ($3.0 \pm 0.1\%$)	— —	— —
outputs	$48398 \pm 852^*$ ($30.1 \pm 0.5\%^*$)	$5160 \pm 171^*$ ($3.2 \pm 0.1\%^*$)	30538 ± 1306 ($19.0 \pm 0.8\%$)	76792 ± 653 ($47.7 \pm 0.4\%$)

Table 5.4: The number of hadron faking electron, conversion, $c\bar{c}$ and $b\bar{b}$ in the **whole electron sample** obtained with the impact parameter fit. *Fit is constrained to the inputs.

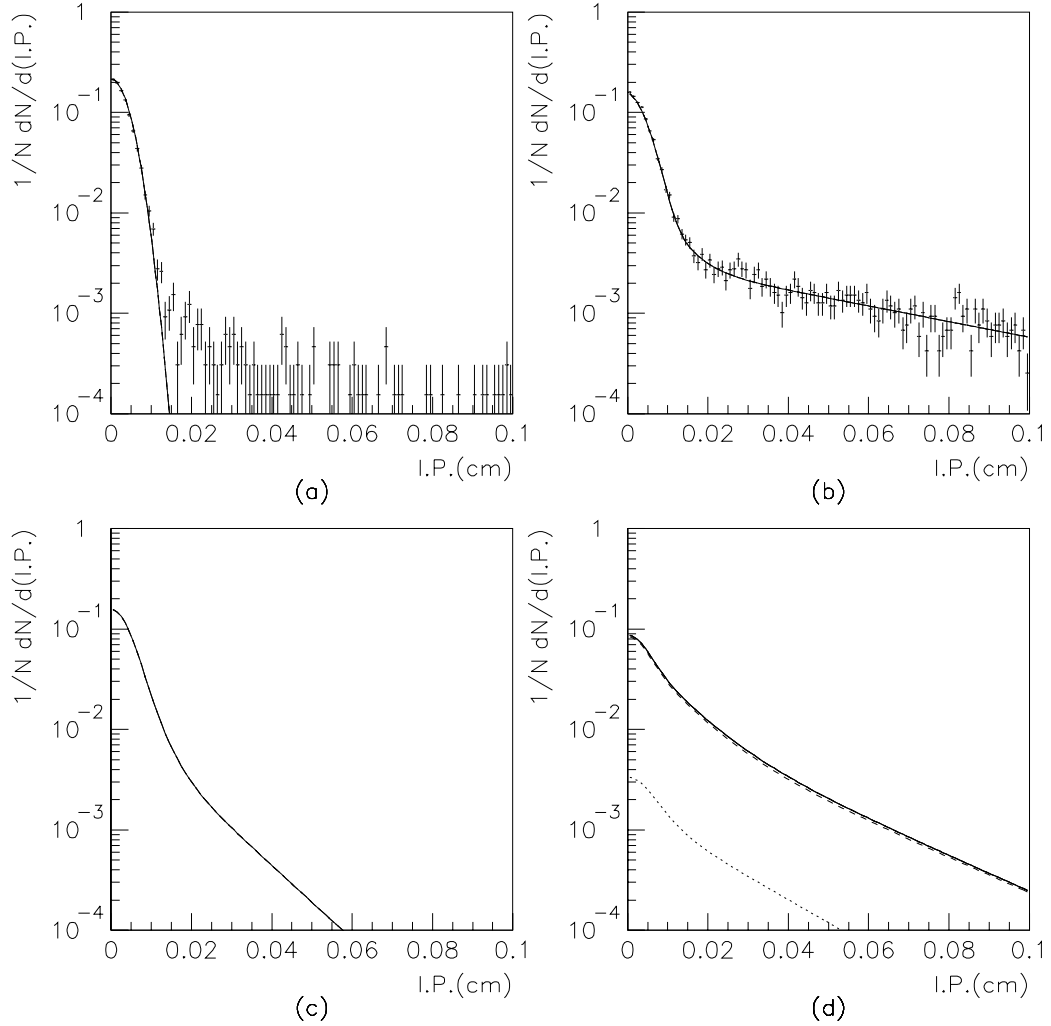


Figure 5.7: The impact parameter distributions for (a) hadron faking electrons, (b) photon conversions, (c) $c\bar{c}$ Monte Carlo, and (d) $b\bar{b}$ Monte Carlo (dashed curve: direct $b \rightarrow e$ decays, dotted curve: sequential $b \rightarrow c \rightarrow e$ decays).

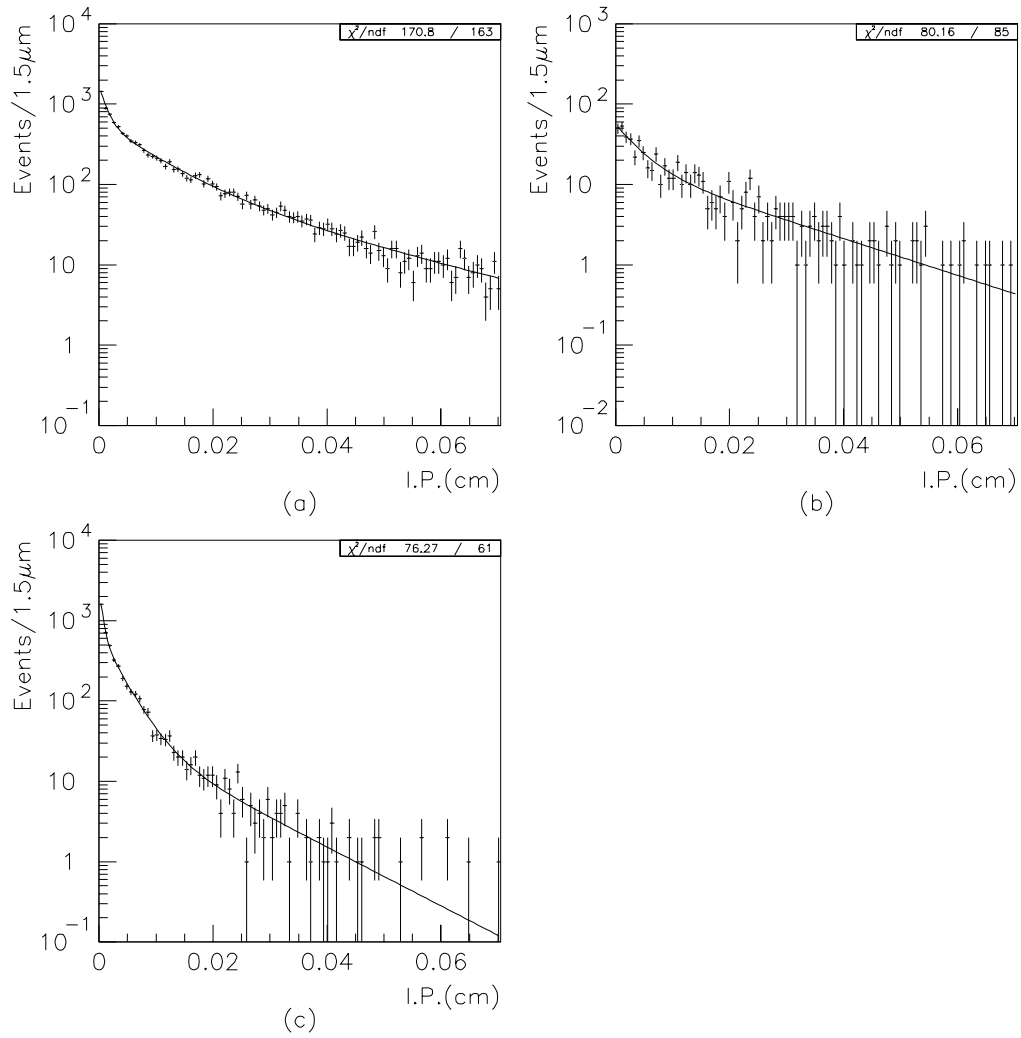


Figure 5.8: The impact parameter distributions without detector resolution.
 (a) Direct $b \rightarrow e$ decays (b) Sequential $b \rightarrow c \rightarrow e$ decays (c) $c \rightarrow e$ decays

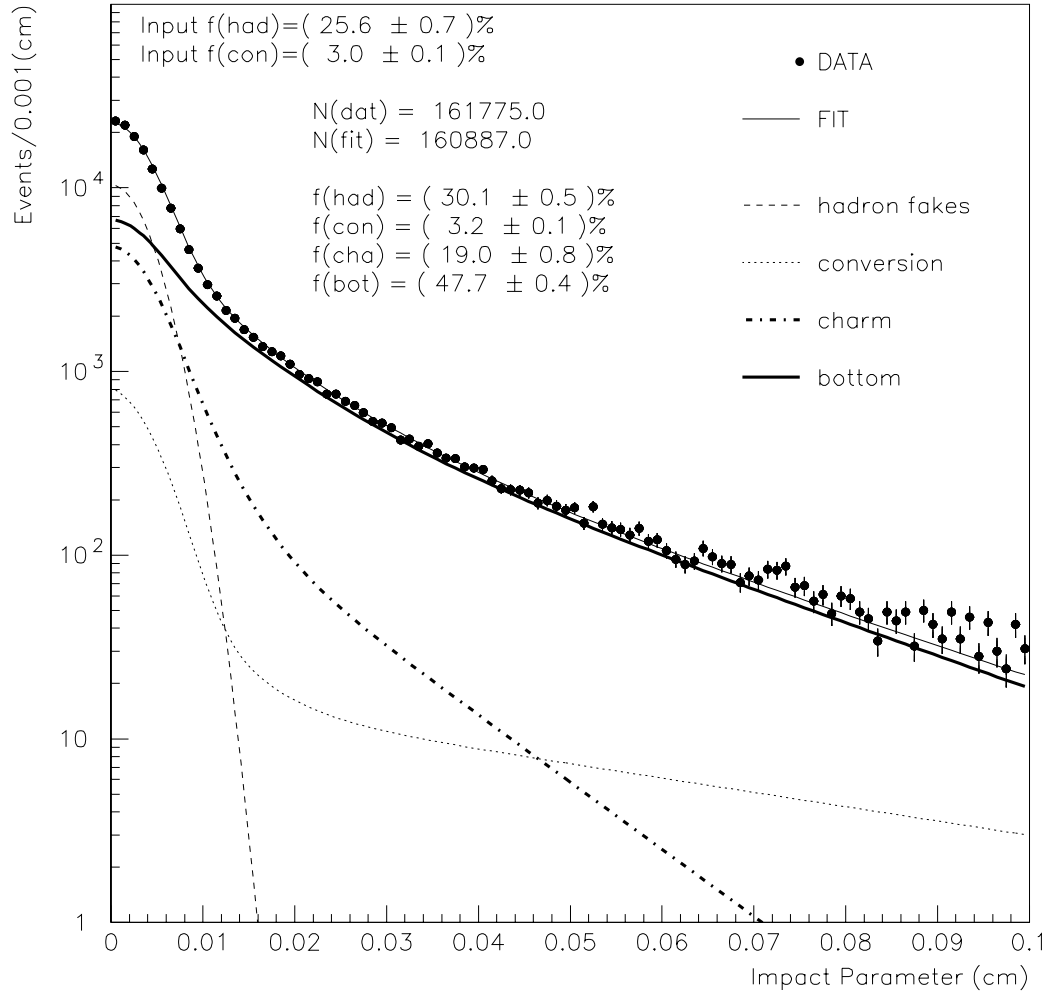


Figure 5.9: The impact parameter distribution for the whole electron sample. Results of the four-component fit are also shown. Dashed curve shows hadron faking electrons, dotted curve shows conversions, thick dashed curve shows $c\bar{c}$ and thick solid curve shows $b\bar{b}$.

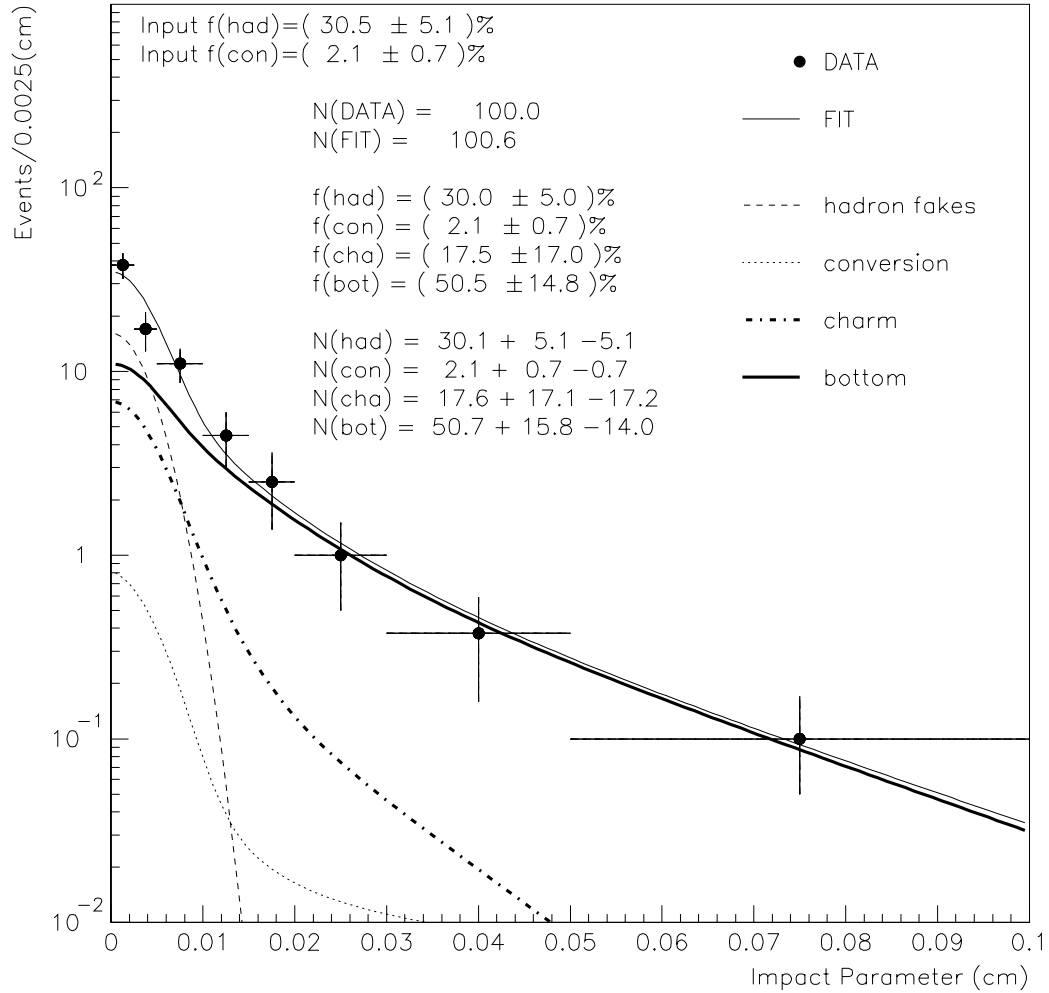


Figure 5.10: The impact parameter distribution for the diffractive candidates. Results of the four-component fit are also shown. Dashed curve shows hadron faking electrons, dotted curve shows conversions, thick dashed curve shows $c\bar{c}$ and thick solid curve shows $b\bar{b}$.

	hadron	conversion	$c\bar{c}$	$b\bar{b}$
inputs from CPR and ε_{conv}	30.5 ± 5.1 (30.5 ± 5.1)%	5.4 ± 1.8 (2.1 ± 0.7)%	— —	— —
outputs	$30.1\pm 5.1^*$ (30.0 ± 5.0)%*	$2.1\pm 0.7^*$ (2.1 ± 0.7)%*	17.6 ± 17.1 (17.5 ± 17.0)%	50.7 ± 14.9 (50.5 ± 14.8)%

Table 5.5: The number of hadron faking electron, conversion, $c\bar{c}$ and $b\bar{b}$ in the **diffractive candidates** obtained with the impact parameter fit. *Fit is constrained to the inputs.

5.4 Combined results

For the whole electron sample, the number of $b\bar{b}$ events is estimated to be $69165 \pm 931(\text{stat})$ and $76792 \pm 653(\text{stat})$ by the p_T^{rel} and the impact parameter fits, respectively. We combine two results by taking a weighted mean and obtain $73371 \pm 485(\text{stat})$ $b\bar{b}$ events in the whole electron sample. The corresponding $b\bar{b}$ fraction is $45.4\pm 0.3(\text{stat})\%$.

For the diffractive candidates, we fit both p_T^{rel} and impact parameter distribution simultaneously with a maximum likelihood method. The fit results are shown in Fig. 5.11. We estimate that the number of $b\bar{b}$ events in diffractive candidates to be $44.4\pm 10.2(\text{stat})$.

The fit results are summarized in Tables 5.6 and 5.7.

	hadron	conversion	$c\bar{c}$	$b\bar{b}$
input from CPR and ε_{conv}	41489 ± 1063 (25.6 ± 0.7)%	4924 ± 172 (3.0 ± 0.1)%	— —	— —
output by p_T^{rel} fit	$43554\pm 931^*$ (27.0 ± 0.6)%*	$5000\pm 168^*$ (3.1 ± 0.1)%*	43668 ± 726 (27.1 ± 0.4)%	69165 ± 742 (42.9 ± 0.4)%
output by impact parameter fit	$48398\pm 852^*$ (30.1 ± 0.5)%*	$5160\pm 171^*$ (3.2 ± 0.1)%*	30538 ± 1306 (19.0 ± 0.8)%	76792 ± 653 (47.7 ± 0.4)%

Table 5.6: The number of hadron faking electrons, conversion, $c\bar{c}$ and $b\bar{b}$ in the **whole electron sample** by the p_T^{rel} and impact parameter fit. *Fit is constrained to the inputs.

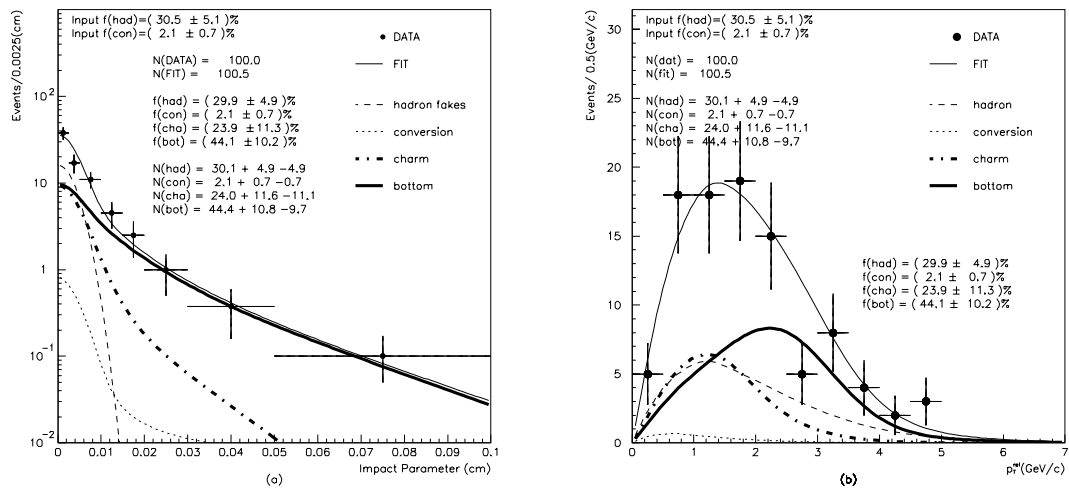


Figure 5.11: The impact parameter distribution and the p_T^{rel} distribution of the diffractive candidates. The results of the four-component fit to the combined two distributions are also shown. Dashed curve shows hadron faking electrons, dotted curve shows conversions, thick dashed curve shows $c\bar{c}$ and thick solid curve shows $b\bar{b}$.

	hadron	conversion	$c\bar{c}$	$b\bar{b}$
inputs from CPR and ε	30.5 ± 5.1 (30.5 ± 5.1)%	2.1 ± 0.7 (2.1 ± 0.7)%	— —	— —
output by p_T^{rel} fit	$31.3\pm 5.1^*$ (31.6 ± 5.1)%*	$2.1\pm 0.7^*$ (2.2 ± 0.7)%*	27.8 ± 13.2 (28.1 ± 13.3)%	37.8 ± 13.6 (38.2 ± 13.7)%
output by impact parameter fit	$30.1\pm 5.1^*$ (30.0 ± 5.0)%*	$2.1\pm 0.7^*$ (2.1 ± 0.7)%*	17.6 ± 17.1 (17.5 ± 17.0)%	50.7 ± 14.9 (50.5 ± 14.8)%
output from combined i.p.+ p_T^{rel}	$30.1\pm 4.9^*$ (29.9 ± 4.9)%*	$2.2\pm 0.7^*$ (2.1 ± 0.7)%*	24.0 ± 11.3 (23.9 ± 11.3)%	44.4 ± 10.2 (44.1 ± 10.2)%

Table 5.7: The number of hadron faking electrons, conversion, $c\bar{c}$ and $b\bar{b}$ in the **diffractive candidates** by the p_T^{rel} and impact parameter fit. *Fit is constrained to the inputs.

Chapter 6

Ratio of the diffractive to the non-diffractive $b\bar{b}$ production

The number of $b\bar{b}$ events in both the whole electron sample and the diffractive candidates are estimated in the previous chapter. In this chapter, we calculate the ratio of the diffractive to the non-diffractive $b\bar{b}$ production $R_{b\bar{b}}$ using these results. At first we describe the correction factors due to the limited acceptance of the rapidity gap method which is used to select the diffractive candidates from the whole electron sample. The ratio $R_{b\bar{b}}$ is then calculated. The systematic uncertainties on $R_{b\bar{b}}$ are estimated in the final section.

6.1 Acceptance for the rapidity gap tagging

6.1.1 Acceptance for single interaction events

The efficiency of the rapidity gap tagging is limited to the events with only one $p\bar{p}$ interaction in a single bunch crossing although we allow the events to have multiple reconstructed vertex in the VTX. The reason for this inefficiency is the following: when the extra $p\bar{p}$ interactions occur in a single bunch crossing, generated particles from these interactions always kill the rapidity gap signal. The acceptance for the single interaction is evaluated as a function of the luminosity.

The mean luminosity for a single bunch crossing $\langle L_{bunch} \rangle$ is calculated with an instantaneous luminosity L_{inst} measured by the BBC hit rate,

$$\begin{aligned} \langle L_{bunch} \rangle &= \frac{C_{acc} \times \langle L_{inst} \rangle}{f} \\ &= \frac{0.9772 \times 8.415}{286.278} \\ &= 0.02872 (mb^{-1}) \\ &\left(C_{acc} = 1 - 0.002704 \times \langle L_{inst} \rangle \right) \end{aligned}$$

where C_{acc} is the accidental correction factor [35] for L_{inst} and f is the frequency of a bunch crossing in the Tevatron.

Using the above $\langle L_{bunch} \rangle$, the average number of inelastic $p\bar{p}$ interactions in a single bunch crossing is given by,

$$\begin{aligned} \langle n \rangle &= \sigma_{BBC} \times \langle L_{bunch} \rangle \\ &= 51.15 \times 0.02872 \\ &= 1.469 \end{aligned}$$

where σ_{BBC} is the cross section of an inelastic $p\bar{p}$ interaction which hits the BBC [35, 40]. Finally, the acceptance for events without extra visible interactions is given by the Poisson statistics,

$$\begin{aligned} A_{1vx} &= e^{-\langle n \rangle} \\ &= 0.230. \end{aligned}$$

6.1.2 Livetime efficiency of the BBC and the forward calorimeter

Any noises in the BBC or the forward calorimeters kill the rapidity gap signal. The no-noise probability of the BBC and the forward calorimeters is estimated by studying a rate of noise hits in those detectors for events with no reconstructed vertex in the VTX. Although our analysis is done for RUN1B data, we use RUN1A clock trigger data to study this efficiency

because there are no such unbiased triggers in RUN1B. Figure 6.1 shows a probability of no-noise in the forward detectors plotted as a function of an instantaneous luminosity. The noise associated with the luminosity is observed in the plot. We parameterize the luminosity dependence of the noise using a linear function and then estimate the probability of no-noise in our RUN1B electron sample. The probability of no-noise is 0.805 and 0.739 for $-\eta$ side and $+\eta$ side, respectively. Since the number of observed rapidity gap signals are the same in each sides (see Sec. 3.2), we take the mean of two numbers for the probability of no-noise in our sample,

$$A_{live} = 0.772.$$

6.1.3 Gap acceptance for diffractive events

The acceptance for the rapidity gap tagging for the diffractive $b\bar{b}$ event is evaluated using POMPYT 2.6 Monte Carlo simulator [36]. POMPYT 2.6 is an add-on program of the PYTHIA 5.7. The simulation is based on the Ingelman-Shelin model as described in Chapter 1. The POMPYT 2.6 employs the following steps for the event generation. At first, “pomeron” having the momentum of $900 \xi \text{ GeV}/c$ is emitted from the beam particle. The kinematical parameters of the pomeron (t, ξ) are randomly determined according to the Donnachie-Landshoff flux, where ξ is the fractional momentum of the pomeron carrying to the proton and t is a momentum transfer squared. We use the following parameters in the DL flux model,

$$\begin{array}{ll}
 \beta_0^2 = 3.202 \text{ GeV}^{-2} & \text{effective quark – pomeron coupling} \\
 \epsilon' = 0.115 & \text{intercept of the pomeron trajectory} \\
 \alpha' = 0.26 \text{ GeV}^{-2} & \text{slope of the pomeron trajectory} \\
 \sigma_T^{pP} = 2.3 \text{ mb} & \text{pomeron – proton total cross section}
 \end{array}$$

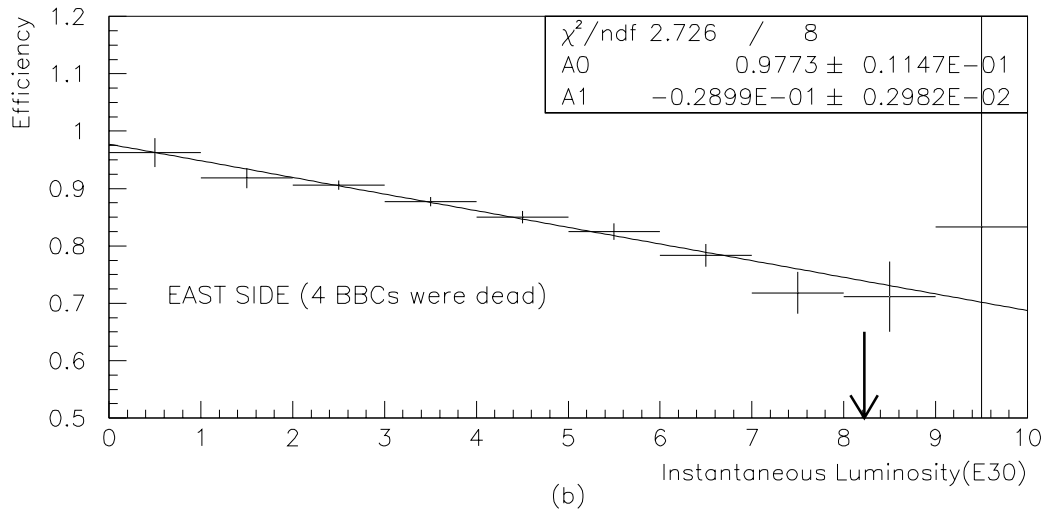
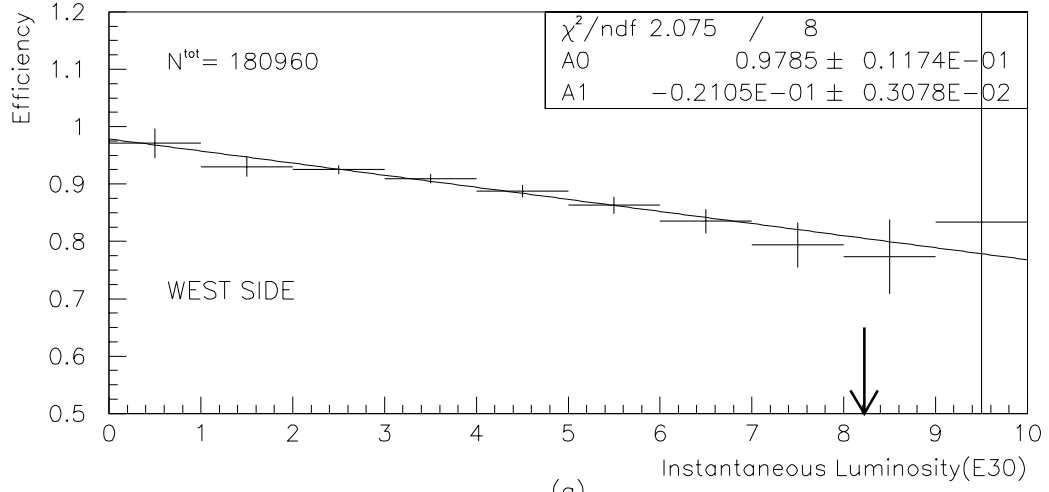


Figure 6.1: The probability of no-noise in both BBC and forward calorimeters as a function of instantaneous luminosity ($\times 10^{30}$). The arrow points to the mean instantaneous luminosity of the whole electron sample (RUN1B). (a) The probability of no-noise in west side ($\eta < 0$) detectors. (b) The probability of no-noise in east side ($\eta > 0$) detectors.

Next the hard collision between the partons in the pomeron and the target particle is simulated using the leading order perturbative QCD calculation with the PYTHIA 5.7. We use the EHLQ set-1 structure function to simulate the parton density in the proton as used in the previous CDF studies for the diffractive W [11] and the diffractive dijet production [10]. The fragmentation process of the outgoing partons are simulated with the JETSET 7.4.

We use the two kinds of the structure function, “flat” distribution ($z f_{g,q/\mathbb{P}}(z) \sim 1$) and “hard” distribution ($z f_{g,q/\mathbb{P}}(z) \sim z(1-z)$) for the pomeron. The kinematical ranges of the event generation is limited for ξ below 0.1 and $|t|$ below $5.0 \text{ GeV}^2/c^2$. The b -quarks are generated with p_T above $12 \text{ GeV}/c$. The restriction to the semi-leptonic decay and the simulation of the CDF detector including the Level-2 trigger are made as described in Sec. 5.1. The simulated events are filtered using the same selection cuts as described in Chapter 3 except for the CPR charge requirement.

Using the filtered sample, the particle multiplicity at the location of the forward detectors is further simulated using the full detector simulation program CDFSIM which simulates the interactions in the detector material. The output signal from the detector for the low energy particles is not correctly modeled in the CDFSIM and QFL. Instead of these simulators, we simply model the response of the forward calorimeter by the following equation,

$$E_i^{obs} = S_i \times p^{gen} + C_i$$

where p^{gen} is a momentum of the particle, S_i and C_i are energy correction factors determined as a function of each η of the tower. The detail of this model is described in Appendix C.

The final results of the multiplicity simulations are shown in Figs. 6.2(a)-(d) for the four kinds of pomeron model, flat-gluon, flat-quark, hard-gluon, and hard-quark, respectively. The acceptance for the rapidity gap tagging,

$N_{BBC}=0$ and $N_{clust}=0$, is found to be,

$$A_{gap}^{FG}=0.406, \quad (\text{Flat Gluon pomeron})$$

$$A_{gap}^{FQ}=0.273, \quad (\text{Flat Quark pomeron})$$

$$A_{gap}^{HG}=0.359, \quad (\text{Hard Gluon pomeron})$$

$$A_{gap}^{HQ}=0.217. \quad (\text{Hard Quark pomeron})$$

The kinematic variable $\xi(< 1)$ is related to the size of rapidity gap $\Delta\eta$ by the following equation,

$$\Delta\eta \sim -\ln \xi.$$

The size of the rapidity gap increases as the pomeron ξ decrease. Figures 6.3(a)-(d) show the ξ distributions of the simulated events. The events tagged by a rapidity gap is populated in the ξ range below 0.1.

6.2 Ratio of the diffractive to the non-diffractive $b\bar{b}$ production

The number of $b\bar{b}$ events found in the diffractive signal region is $N_{b\bar{b}}(0,0) = 44.4 \pm 10.2$ events as described in Sec. 3.2.

Since this number contains the contribution of the non-diffractive $b\bar{b}$ events, we have to remove this contribution at first. The non-diffractive events in the diffractive signal region is $N^{ND}(0,0) = 24.4$ events as described in Sec. 3.2. Assuming that the fraction of $b\bar{b}$ events in the non-diffractive sample does not depend on the forward multiplicity, we obtain the number of the $b\bar{b}$ events in the above backgrounds,

$$\begin{aligned} N_{b\bar{b}}^{ND}(0,0) &= N^{ND}(0,0) \times f_{b\bar{b}}^{ND} \\ &= 24.4 \times (0.454 \pm 0.003) \\ &= 11.1 \pm 0.08(stat) \text{ events.} \end{aligned}$$

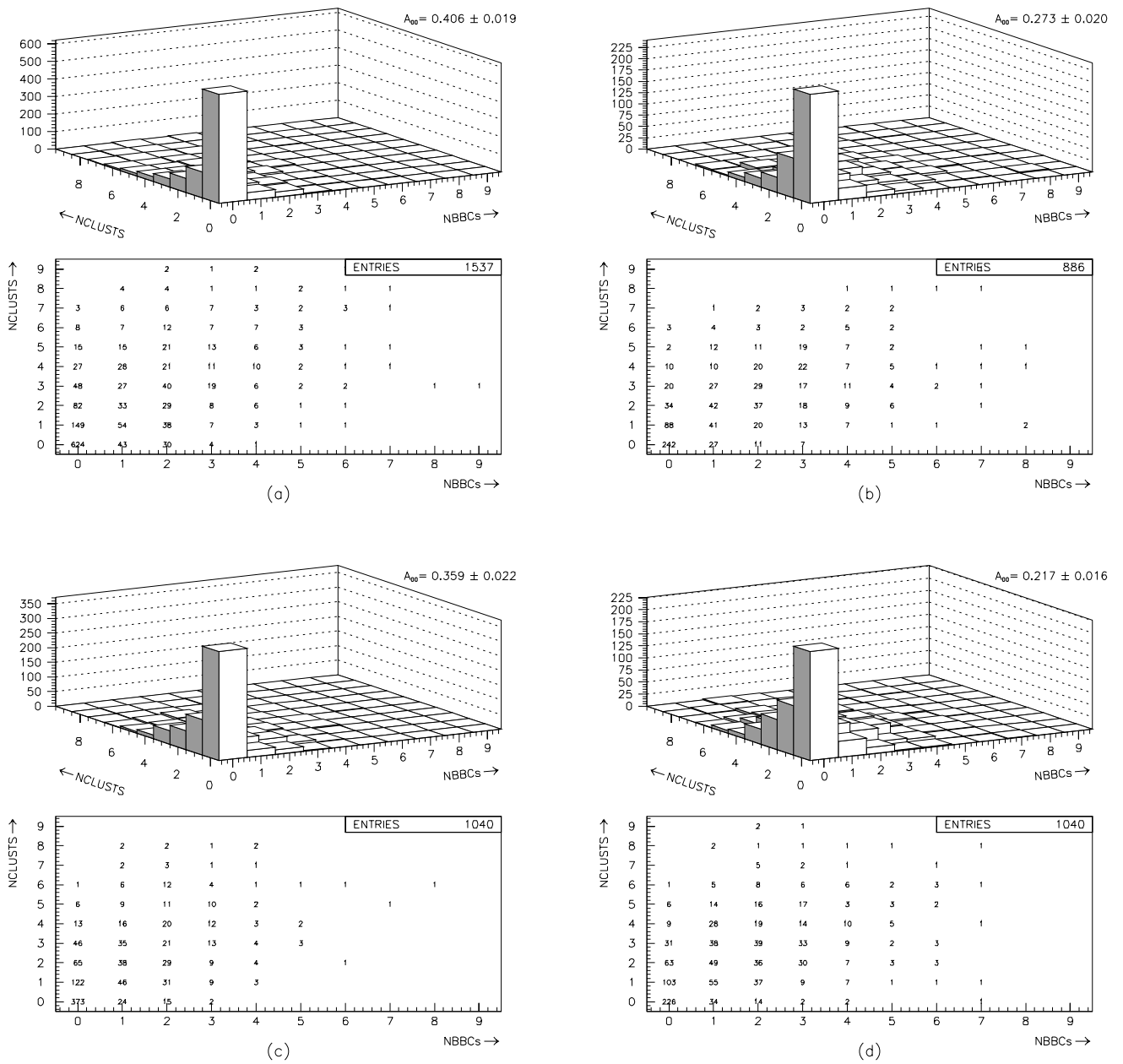


Figure 6.2: Simulated multiplicity distribution for the diffractive $b\bar{b}$ events with (a) flat-gluon pomeron, (b) flat-quark pomeron, (c) hard-gluon pomeron, and (d) hard-quark pomeron.

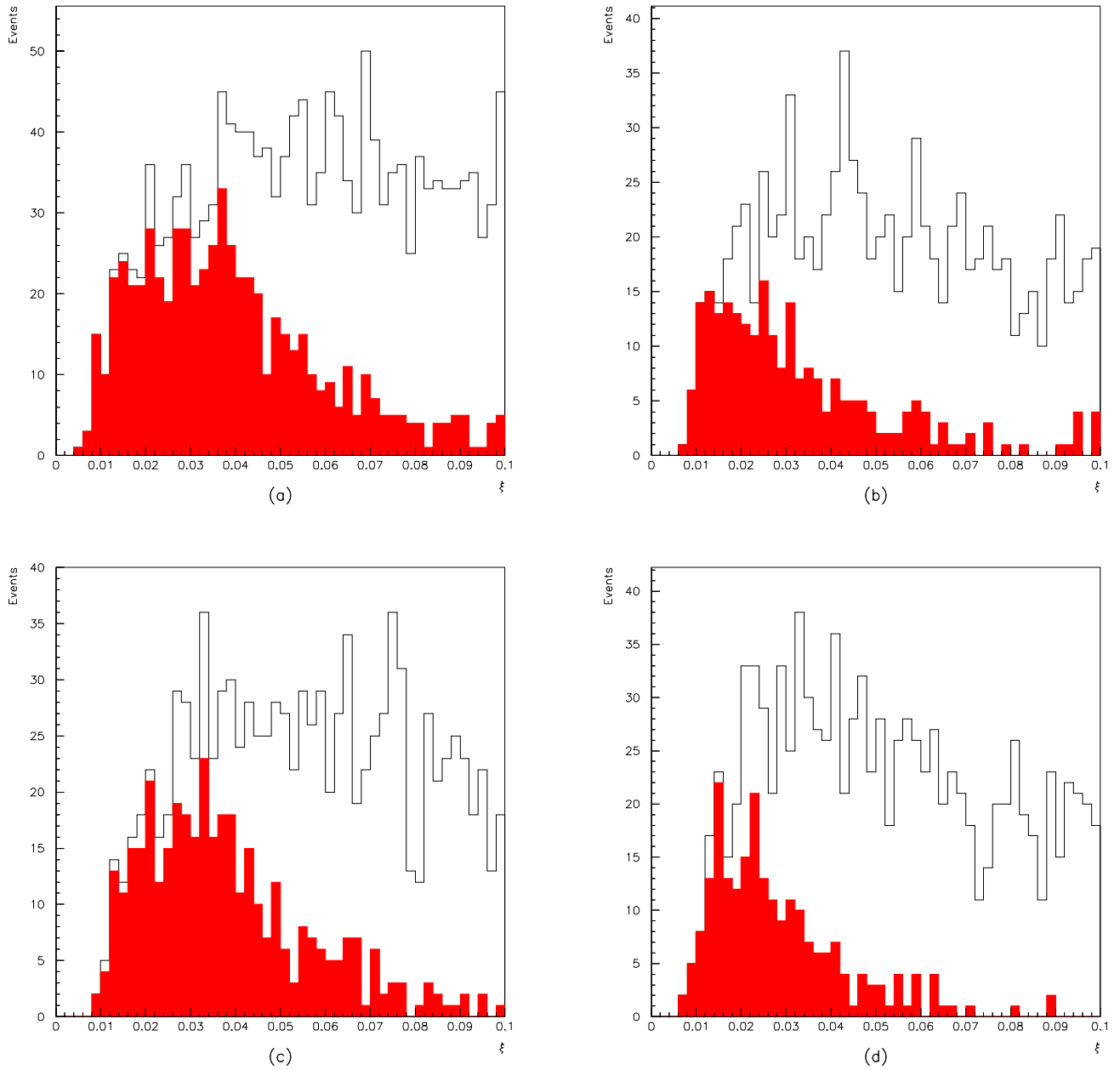


Figure 6.3: Simulated ξ distribution for the diffractive $b\bar{b}$ events. Shaded area shows the events tagged by a rapidity gap in the forward detectors with (a) flat-gluon pomeron, (b) flat-quark pomeron, (c) hard-gluon pomeron, and (d) hard-quark pomeron.

The number of diffractive $b\bar{b}$ events in the signal region is found to be $33.3 \pm 10.2(\text{stat})$.

The total number of diffractive $b\bar{b}$ events in the whole electron sample is calculated by correcting the acceptances,

$$\begin{aligned} N_{b\bar{b}}^{DIF}(\xi < 0.1; \text{FG}) &= \{N_{b\bar{b}}(0, 0) - N_{b\bar{b}}^{ND}(0, 0)\} \times \frac{1}{A_{1vx}} \times \frac{1}{A_{live}} \times \frac{1}{A_{gap}^{FG}} \\ &= (33.3 \pm 10.2) \times \frac{1}{0.230} \times \frac{1}{0.772} \times \frac{1}{0.406} \\ &= 461 \pm 142(\text{stat}) \text{ events.} \end{aligned}$$

The total number of $b\bar{b}$ events in the whole electron sample is $73371 \pm 485(\text{stat})$ events. The ratio of the diffractive to the non-diffractive $b\bar{b}$ production is obtained,

$$\begin{aligned} R_{b\bar{b}}(\xi < 0.1; \text{FG}) &= \frac{N_{b\bar{b}}^{DIF}(\xi < 0.1; \text{FG})}{N_{b\bar{b}}^{ND}} = \frac{461 \pm 142}{73371 \pm 485} \\ &= 0.63 \pm 0.19(\text{stat})\% \end{aligned}$$

Since the gap acceptance is a model dependent quantity, we show here the result without correcting the gap acceptance,

$$R_{b\bar{b}}(\text{GAP}) = 0.255 \pm 0.078(\text{stat})\%$$

where ‘‘GAP’’ means no energy deposition above 1.5 GeV in the forward calorimeter ($2.4 < |\eta| < 4.2$) and no charged particle hit in the BBC ($3.2 < |\eta| < 5.9$).

The ratio of the diffractive to the non-diffractive $b\bar{b}$ events after the gap acceptance correction is listed for each pomeron models below,

$$\text{Flat} - \text{Gluon} : R_{b\bar{b}}(\xi < 0.1; \text{FG}) = 0.63 \pm 0.19(\text{stat})\%$$

$$\text{Flat} - \text{Quark} : R_{b\bar{b}}(\xi < 0.1; \text{FQ}) = 0.93 \pm 0.29(\text{stat})\%$$

$$\text{Hard} - \text{Gluon} : R_{b\bar{b}}(\xi < 0.1; \text{HG}) = 0.71 \pm 0.22(\text{stat})\%$$

$$\text{Hard} - \text{Quark} : R_{b\bar{b}}(\xi < 0.1; \text{HQ}) = 1.18 \pm 0.36(\text{stat})\%.$$

6.3 Systematic uncertainties

We have measured the $b\bar{b}$ fraction in the whole electron sample using two independent methods, the p_T^{rel} fit and the impact parameter fit. The difference in the $b\bar{b}$ fractions between the two methods is 10.6% relative to the combined result of the measurements. We assign this difference as a systematic uncertainty on the $b\bar{b}$ fraction for the whole electron sample.

$$\left. \frac{\delta R_{b\bar{b}}}{R_{b\bar{b}}} \right|_{b\bar{b}(ND)} = \frac{\delta N_{b\bar{b}}^{ND}}{N_{b\bar{b}}^{ND}} = 0.106$$

We also assign this relative uncertainty of 10.6% as the systematic uncertainty on the $b\bar{b}$ fraction in the diffractive candidates.

$$\begin{aligned} \left. \frac{\delta R_{b\bar{b}}}{R_{b\bar{b}}} \right|_{b\bar{b}(0,0)} &= \frac{\delta N_{b\bar{b}}(0,0)}{N_{b\bar{b}}^{DIF}(0,0)} = \frac{0.106 \times 44.4}{33.3} \\ &= 0.141 \end{aligned}$$

The method to estimate the non-diffractive background in the diffractive candidates was described in Sec. 3.2. We use the uncertainty in the background fitting as a systematic uncertainty.

$$\begin{aligned} \left. \frac{\delta R_{b\bar{b}}}{R_{b\bar{b}}} \right|_{BG} &= \frac{\delta N_{b\bar{b}}^{ND}(0,0)}{N_{b\bar{b}}^{DIF}(0,0)} = \frac{5.55 \times 0.454}{33.3} \\ &= 0.076 \end{aligned}$$

The systematic uncertainty due to the single interaction acceptance is calculated using the σ_{BBC} uncertainty of 1.7mb [40].

$$\begin{aligned} \left. \frac{\delta R_{b\bar{b}}}{R_{b\bar{b}}} \right|_{1vx} &= \frac{\delta A_{1vx}}{A_{1vx}} = \langle L_{bunch} \rangle \times \delta(\sigma_{BBC}) \\ &= 0.049 \end{aligned}$$

We measure the livetime efficiency of the BBC and the forward calorimeter using RUN1A “empty” events, but the BBC condition in RUN1A is not identical to that in RUN1B since four BBC modules are dead in RUN1A while they are alive in RUN1B. On the other hand, the BBC in the west side

is kept in the same condition through RUN1A and RUN1B. The difference in measured efficiencies between the east side and the west side is 0.066. We assign this difference as a systematic uncertainty on the live time efficiency of the BBC and the forward calorimeter.

$$\begin{aligned} \left. \frac{\delta R_{b\bar{b}}}{R_{b\bar{b}}} \right|_{live} &= \frac{\delta A_{live}}{A_{live}} = \frac{0.066}{0.772} \\ &= 0.086 \end{aligned}$$

The systematic uncertainty due to the gap acceptance for the diffractive events depends on the model of the Monte Carlo program and the forward detector simulation. We restrict our study in the models where the pomeron has a flat structure function, $z f_{g,q/\mathbb{P}}(z) \sim 1$ or a hard structure function, $z f_{g,q/\mathbb{P}}(z) \sim z(1-z)$. We estimate the uncertainty due to the detector simulation by changing the energy correction factors and offsets according to the fitting errors. We found this uncertainty to be $\pm 1.5\%$. Taking a quadratic sum of the statistical uncertainty for the Monte Carlo events and this uncertainty, we obtain the systematic uncertainty on the Monte Carlo gap acceptance as:

$$\begin{aligned} \left. \frac{\delta R_{b\bar{b}}}{R_{b\bar{b}}} \right|_{gap(FG)} &= \frac{\delta A_{gap(FG)}}{A_{gap(FG)}} = \frac{\sqrt{0.015^2 + 0.019^2}}{0.406} = 0.059 \\ \left. \frac{\delta R_{b\bar{b}}}{R_{b\bar{b}}} \right|_{gap(FQ)} &= 0.082 \\ \left. \frac{\delta R_{b\bar{b}}}{R_{b\bar{b}}} \right|_{gap(HG)} &= 0.078 \\ \left. \frac{\delta R_{b\bar{b}}}{R_{b\bar{b}}} \right|_{gap(HQ)} &= 0.090 \end{aligned}$$

Including all systematic uncertainties, the ratio of the diffractive to the

non-diffractive $b\bar{b}$ production is measured as:

$$R_{b\bar{b}}(\xi < 0.1; \text{FG}) = 0.63 \pm 0.19(\text{stat}) \pm 0.14(\text{syst})\%$$

$$R_{b\bar{b}}(\xi < 0.1; \text{FQ}) = 0.93 \pm 0.29(\text{stat}) \pm 0.22(\text{syst})\%$$

$$R_{b\bar{b}}(\xi < 0.1; \text{HG}) = 0.71 \pm 0.22(\text{stat}) \pm 0.16(\text{syst})\%$$

$$R_{b\bar{b}}(\xi < 0.1; \text{HQ}) = 1.18 \pm 0.36(\text{stat}) \pm 0.27(\text{syst})\%$$

All systematic uncertainties discussed in this section are listed in Table 6.1.

The number of $b\bar{b}$ events in the whole electron sample	10.6%
The number of $b\bar{b}$ events in (0,0)	14.1%
The number of non-diffractive $b\bar{b}$ events in (0,0)	7.6%
Acceptance for single interaction	4.9%
Live time efficiency for the forward detectors	8.6%
Monte Carlo gap acceptance	5.9%
Total systematic uncertainty	22.3%

Table 6.1: Systematic uncertainties relative to the $R_{b\bar{b}}$ for the flat-gluon pomeron model.

Chapter 7

Comparison with the theoretical prediction

The theoretical prediction for the $R_{b\bar{b}}$ is obtained using the Monte Carlo simulator with the DL pomeron flux. POMPYPY 2.6 and PYTHIA 5.7(non-tuned) are used for the diffractive and the non-diffractive processes, respectively. We use EHLQ set-1 structure function [37] which has been confirmed [11] to give the correct underlying multiplicity in minimum bias $p\bar{p}$ scattering in a wide range of \sqrt{s} including the typical \sqrt{s} of the pomeron-proton scattering in the diffractive $b\bar{b}$ production, $\sqrt{s} \sim 300$ GeV. The results of the simulation are summarized in Table 7.1.

	$\sigma_{b\bar{b}}$ (μb)	$N_{passed}/N_{gen}(\%)$	$R_{b\bar{b}}(\%)$
non-diffractive	9.45×10^{-1}	0.26	-
Flat-Gluon	1.22×10^{-1}	0.21	10.4
Flat-Quark	1.35×10^{-2}	0.17	0.92
Hard-Gluon	1.26×10^{-1}	0.23	11.6
Hard-Quark	1.29×10^{-2}	0.19	1.02

Table 7.1: Theoretical Model prediction for the diffractive $b\bar{b}$ production

For the flat-gluon structure function of the pomeron we obtain $R_{b\bar{b}}^{\text{MC}}(\text{FG}) = 10.4\%$, and for the flat-quark pomeron we obtain $R_{b\bar{b}}^{\text{MC}}(\text{FQ}) = 0.92\%$. The CDF data yields $R_{b\bar{b}}^{\text{DAT}}(\text{FG}) = 0.63 \pm 0.24$ (stat+syst)% for the flat-gluon pomeron, and $R_{b\bar{b}}^{\text{DAT}}(\text{FQ}) = 0.93 \pm 0.36$ (stat+syst)% for the flat-quark

pomeron. This result favors the flat-quark pomeron, but the magnitude of $R_{b\bar{b}}$ depends on the model of the pomeron flux factor, which cannot be uniquely determined by the Regge theory.

The discrepancy of the flux factor between the data and the theory can be evaluated as a function of the gluon fraction, f_g , of the flat(or hard) component of the pomeron by comparing the experimental value of $R_{b\bar{b}}$ with the Monte Carlo predictions [10, 11, 41]. The discrepancy factor D is defined as,

$$D = \frac{R^{\text{DAT}}}{R_{\text{FG}}^{\text{MC}} f_g + R_{\text{FQ}}^{\text{MC}} (1 - f_g)}. \quad (7.1)$$

$D=1$ means the DL flux is correct, i.e. the factorization of the pomeron flux is right. Figure 7.1(7.2) shows the measured D for various experiments as a function of the flat-gluon (hard-gluon) fraction f_g . The band in the plot shows the $\pm 1 \sigma$ values of the measurements. The thick solid curve shows the $\pm 1 \sigma$ limit of the diffractive b -quark measurements. In the calculation of the $R_{b\bar{b}}^{\text{DAT}}$, we take account of the change in the gap acceptance according to the quark to gluon ratio. The measured curve of the D vs f_g for the “flat” structure pomeron (Fig. 7.1) is almost the same as for the “hard” structure pomeron as shown in Fig. 7.2. In other measurements, CDF diffractive- W production [11], CDF diffractive-dijet production [10] and ZEUS measurements (DIS + photo-jet production) [8], the “hard” structure function is used to calculate the discrepancy factor D . The diffractive W -boson production is observed using the electron from $W \rightarrow e\nu$ decay in the central rapidity region ($|\eta| < 1.1$), and the ratio of the diffractive to the non-diffractive W -boson production is measured as $R_W = 1.15 \pm 0.55\%$ assuming the gap acceptance of the hard-quark pomeron. The diffractive dijet production is measured using the forward dijets with $E_T > 20$ GeV in the rapidity region of $3.5 > |\eta| > 1.8$ and the ratio of the diffractive to non-diffractive dijet-production is measured as $R_{jj} = 0.75 \pm 0.05(\text{stat}) \pm 0.09(\text{syst}) \%$ assuming the gap acceptance of

the hard gluon pomeron.

The overlap of the bands from the three CDF results shows the allowed range of the D and f_g at the 68% confidence level corresponding to 1σ . The bands slightly meet at their edges of $f_g \sim 0.5$ and $D \sim 0.2$. This result of the gluon fraction is consistent with the results from the ZEUS measurements, $0.3 < f_g < 0.8$. However, the discrepancy factor $D \sim 0.2$ is significantly smaller than the ZEUS results. The discrepancy of the pomeron flux between the CDF and the ZEUS (or DL flux) has already been seen for the diffractive W production and the diffractive dijet production. The CDF results suggest that there is a problem in the hypothesis of the factorization of the pomeron flux described in Chapter 1 [42].

There is a phenomenological model which predicts the break down of the factorization using the “renormalized” pomeron flux [42]. The renormalized flux is defined as the DL flux normalized, if its integral exceeds unity, to one pomeron per nucleon. The discrepancy factor predicted by the renormalized flux is $D_R = 1/(9\beta^{2\epsilon'}) \sim 0.13$, where we used $\beta = 0.5$ [42, 43]. Assuming the gluon fraction of the 70% measured for the diffractive W and the diffractive dijet productions, the discrepancy factor of the diffractive $b\bar{b}$ production is measured to be $D = 0.09 \pm 0.04$, which agrees with the prediction from the renormalized flux.

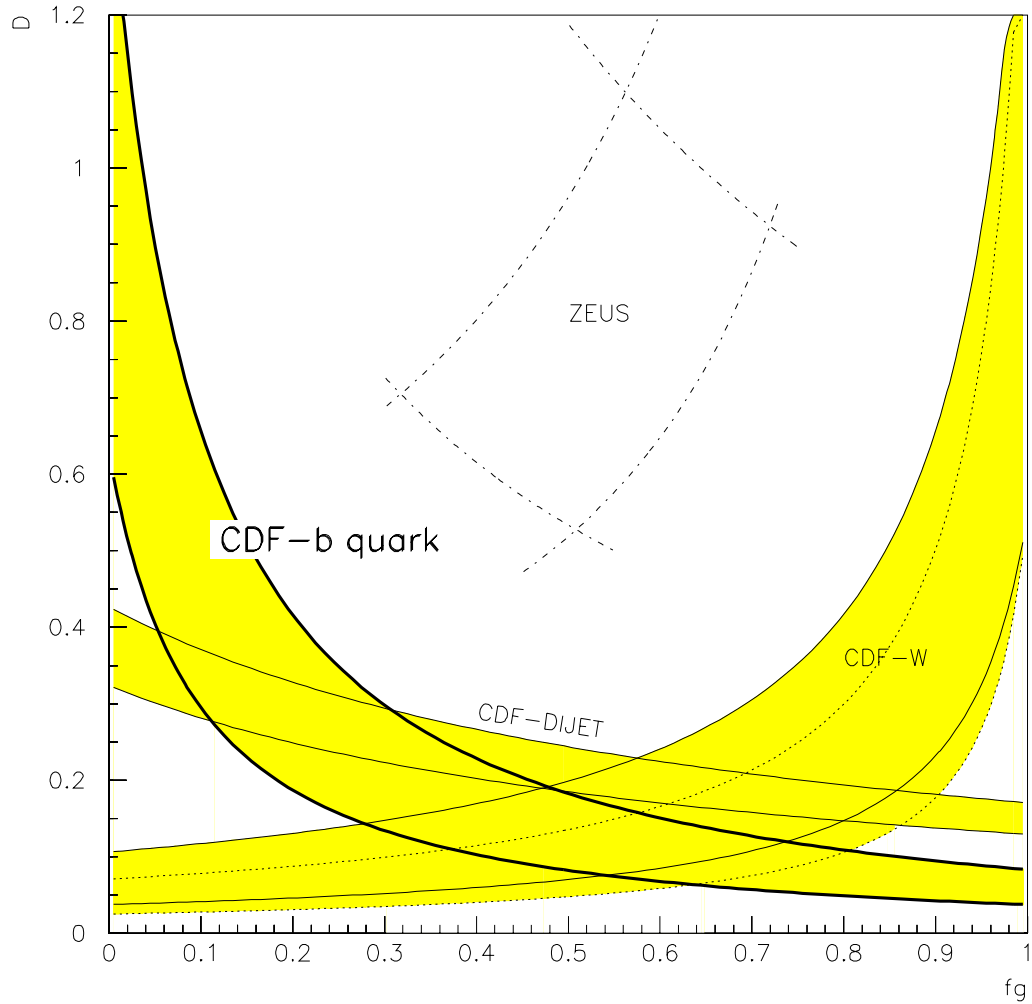


Figure 7.1: The flux discrepancy factor D versus gluon fraction f_g (see text). Results are shown for ZEUS (dashed-dotted), CDF-dijets, CDF- W and CDF- b quark measurements. **The “flat” structure function is used for the CDF- b quark measurement.** The “hard” structure function is used for all the other measurements. The CDF- W result is shown for two (dotted) or three (solid) light quark flavors in the pomeron. The shaded band shows the $\pm 1\sigma$ bounds of the measurements.

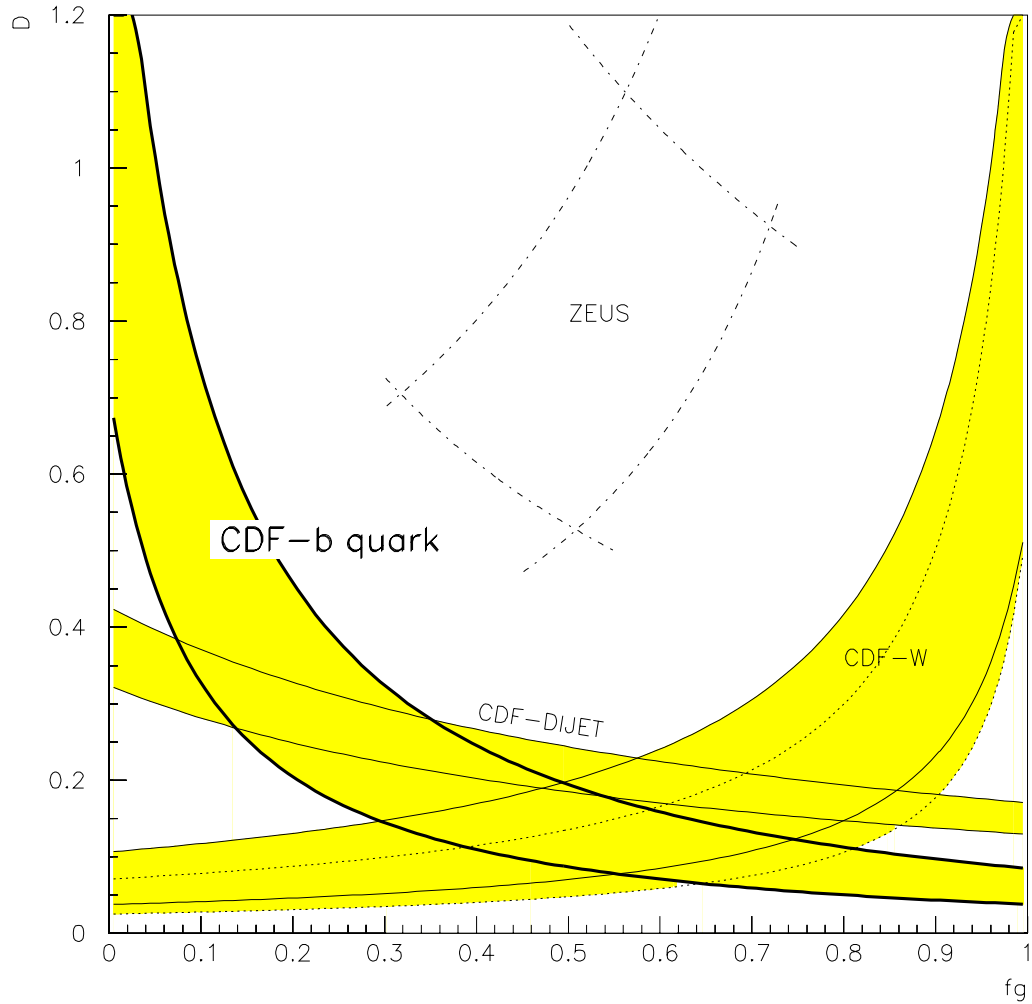


Figure 7.2: The flux discrepancy factor D versus gluon fraction f_g (see text). Results are shown for ZEUS (dashed-dotted), CDF-dijets, CDF- W and CDF- b quark measurements. **The “hard” structure function is used for the CDF- b quark measurement.** The “hard” structure function is used for all the other measurements. The CDF- W result is shown for two (dotted) or three (solid) light quark flavors in the pomeron. The shaded band shows the $\pm 1\sigma$ bounds of the measurements.

Chapter 8

Conclusion

The bottom quark production in the single diffraction has been first observed in $p\bar{p}$ collisions at $\sqrt{s}=1.8$ TeV using the forward rapidity gap method. The high- p_T electron in the central rapidity region ($|\eta| < 1.1$) is used to identify the decay of the produced bottom quark. The ratio of the diffractive to the non-diffractive bottom quark production is obtained using the model dependent acceptance for the rapidity gap signal. For the four kinds of the pomeron model, the ratio is measured to be;

$$R_{b\bar{b}}(\xi < 0.1; \text{FG}) = 0.62 \pm 0.19(\text{stat}) \pm 0.14(\text{syst})\%$$

for the flat – gluon pomeron model,

$$R_{b\bar{b}}(\xi < 0.1; \text{FQ}) = 0.93 \pm 0.29(\text{stat}) \pm 0.22(\text{syst})\%$$

for the flat – quark pomeron model,

$$R_{b\bar{b}}(\xi < 0.1; \text{HG}) = 0.71 \pm 0.22(\text{stat}) \pm 0.16(\text{syst})\%$$

for the hard – gluon pomeron model,

$$R_{b\bar{b}}(\xi < 0.1; \text{HQ}) = 1.18 \pm 0.36(\text{stat}) \pm 0.27(\text{syst})\%$$

for the hard – quark pomeron,

where electron from bottom quark is observed in the kinematic region of $9.5 < E_T^{ele} < 20$ GeV and $|\eta^{ele}| < 1.1$.

The measured ratio is compared to the results of the diffractive W and

the diffractive dijet productions. Results of the three measurements are consistent with each other. The results yields the gluon fraction of $f_g \sim 0.5$, and the flux discrepancy factor of $D \sim 0.2$. The large deviation of D from 1 suggests that there is a problem in the hypothesis of the factorization of the pomeron flux [42].

Appendix A

Regge pole phenomenology

A.1 Regge pole

Aside from the theory of quarks and gluons, there have been an old phenomenological approach to explain the asymptotic behavior of the hadron-hadron collisions. This phenomenology is called *Regge pole phenomenology* or Regge theory in short. In the framework of the Regge theory, a soft hadron-hadron collision is described by the exchange of bunch of mesons which have adequate quantum numbers for the exchange process. Those exchanged objects are called *Regge poles*.

Outline of the Regge theory is briefly described here using $2 \rightarrow 2$ scattering of spin less particles [2, 3]. The Mandelstam variables s and t are used. The s is a center of mass energy squared and the t is a momentum transfer squared. The Lorentz invariant amplitude of the $2 \rightarrow 2$ scattering process can be expressed by the partial wave expansion,

$$A_{a\bar{c} \rightarrow \bar{b}d}(s, t) = \sum_{l=0}^{\infty} (2l+1) a_l(s) P_l(1 + 2t/s), \quad (\text{A.1})$$

where l is a quantum number of orbital angular momentum and P_l is a Legendre polynomial. This expression can be transformed into the following form using the crossing symmetry,

$$A_{ab \rightarrow cd}(s, t) = \sum_{l=0}^{\infty} (2l+1) a_l(t) P_l(1 + 2s/t). \quad (\text{A.2})$$

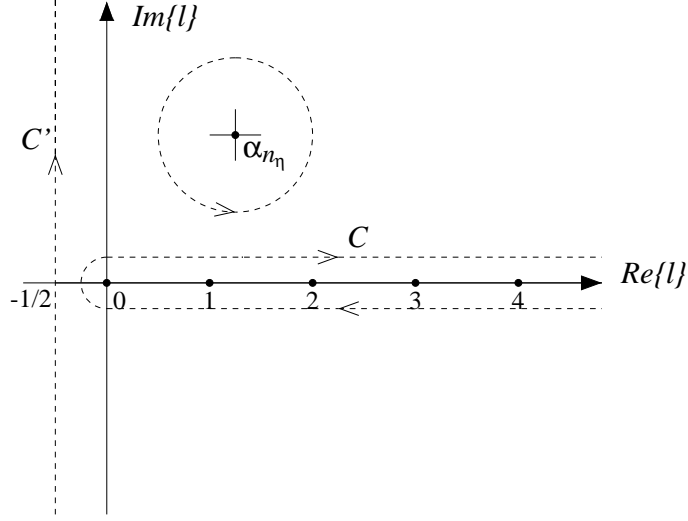


Figure A.1: Complex angular momentum plane.

The summation about l can be rewritten into the integral form in the complex angular momentum plane using the analytic property of the amplitude,

$$A(s, t) = \frac{1}{2i} \oint_C dl \frac{(2l+1)}{\sin \pi l} \sum_{\eta=\pm 1} \frac{(\eta + e^{-i\pi l})}{2} a^{(\eta)}(l, t) P(l, 1 + 2t/s), \quad (\text{A.3})$$

where the contour C surrounds the positive real axis as shown in Fig. A.1. $a^{(+)}$ and $a^{(-)}$ are the analytic continuations of the even and odd partial wave amplitude. The η takes the values ± 1 and is called the signature of the partial wave. The signature is introduced to separate two alternating signed amplitudes owing to the term of $(-1)^l$. Let us suppose for simplicity that the system has just isolated poles at $l = \alpha_{n_\eta}(t)$ of the form $a^{(\eta)}(l, t) = \beta_{n_\eta}(t)(l - \alpha_{n_\eta}(t))^{-1}$. The above integral can be reduced into the sum of the residuals by deforming the contour C into the contour C' as shown in Fig. A.1. For this particular case we arrive at

$$A(s, t) = \sum_{\eta=\pm 1} \sum_{n_\eta} \frac{(2\alpha_{n_\eta}(t) + 1)}{\sin \pi \alpha_{n_\eta}(t)} \frac{(\eta + e^{-i\pi \alpha_{n_\eta}(t)})}{2} \beta_{n_\eta}(t) P(\alpha_{n_\eta}(t), 1 + 2s/t) + (\text{integral on } C'). \quad (\text{A.4})$$

The simple poles $\alpha_{n_\eta}(t)$ are called *Regge poles*. When we take a limit of $s/|t| \rightarrow \infty$, the integral term along the contour C' behaves as $\sim s^{-1/2}$ and so

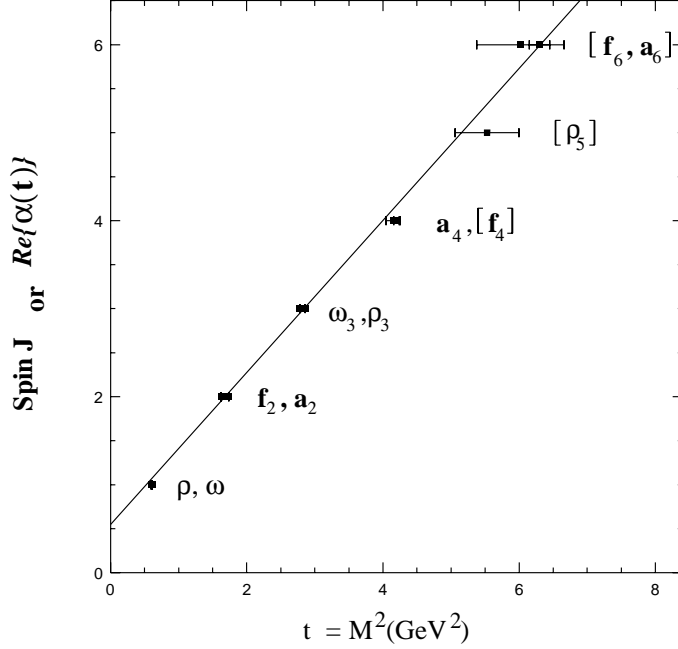


Figure A.2: The Chew-Frautschi plot.

it vanishes. In general, the existence of a single particle state in a theory is appeared as a pole in the transition amplitude. Thus Eq.A.4 shows that the Regge pole with a physical integer value of $l = \Re\{\alpha_{n\eta}(t)\}$ corresponds to a particle with spin- l . In this picture, the scattering process can be interpreted as exchange of the Regge pole (or *Reggeon*) with adequate quantum numbers in the exchange process.

In the high energy limit, the dominant term among the residuals in Eq.A.4 comes from the Regge pole with the largest value of $\Re\{\alpha_{n\eta}(t)\}$ (leading Regge trajectory). Eq.A.4 can be then approximated to,

$$A(s, t) \sim s^{\alpha(t)}, \quad (\text{A.5})$$

where we used asymptotic behavior of the Legendre polynomial,

$$P_l(1 + 2s/t) \xrightarrow{s \gg |t|} \frac{\Gamma(2l + 1)}{\Gamma^2(l + 1)} \left(\frac{s}{t}\right)^l.$$

The function shape of the $\Re\{\alpha(t)\}$ can be investigated by plotting the spin against the square of the mass for existing particles. Figure A.2 shows the

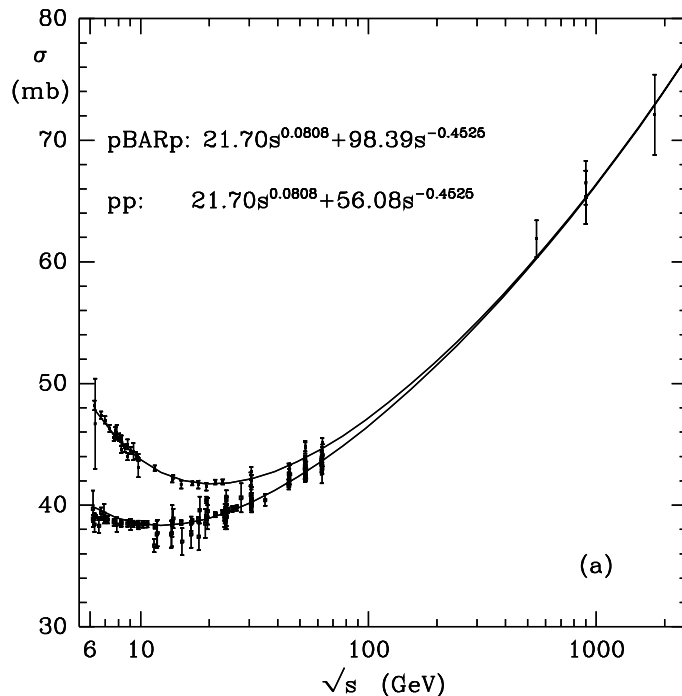


Figure A.4: Total cross-sections for p - p and p - \bar{p} scattering.

Figure A.4 shows the experimental data of the total cross sections for pp and $p\bar{p}$ scattering [14]. It is evident that the total cross section is not simply falling but is slowly rising as s increases. The behavior of rising total cross section is also observed in various kind of hadron-hadron collisions. These data can be beautifully explained [14] if we accept an existence of a new Regge trajectory having the intercept of $\alpha(0)=1+\epsilon(> 0)$ and it carry the quantum number of the vacuum. This new trajectory is called *pomeron trajectory* or *pomeron*. The pomeron trajectory is originally defined with the intercept of $\alpha_P(0)=1$ to satisfy the Pomeranchuk theorem¹ and the Froissart bound², but the later experiments with much higher energy revealed that the situation is more complicated. The fit of the data for the total cross section and elastic

¹A theorem which state that the total cross section against the same target become the same for particle or anti-particle in the high energy limit.

²It is proved that the total cross section for the two hadron scattering cannot increase faster than $(\ln s)^2$ in the limit of $s \rightarrow \infty$ in order to satisfy the unitarity of the S -matrix. This upper bound is called Froissart bound.

cross section tells us that the pomeron trajectory can be parameterized as;

$$\alpha_P(t) = 1 + \epsilon + \alpha' t$$

where $\epsilon=0.0808$ and $\alpha'\sim 0.25\text{GeV}^{-2}$ [14]. So far now no particle has been observed on the pomeron trajectory. However, as one can see in Fig. A.4, the contribution from the pomeron trajectory become dominant in the high energy scattering.

Appendix B

CPR charge correction

The amount of charge deposition in the CPR depends on the momentum of the incident electron. The path length of the incident particle also affects the amount of charge deposition. These dependence must be corrected when one try to compare the CPR charge distributions among various samples. In the thesis, we use the *corrected CPR charge* which do not depend on neither the momentum nor the path-length. In this section, we describe how to obtain the corrected CPR charge using the track information.

As a raw CPR charge, we use a sum of outputs from three CPR-wires around an electron hit position ¹. The hit position is obtained by extrapolating the CTC track to the detector radius at the CPR layer.

The momentum and path-length dependence are studied using control samples. Conversion electrons and electrons from W decays are used for the lower and higher momentum regions, respectively.

At first we parameterize the dependence of the CPR charge on the path length by fixing the momentum range. Since the path length is related to the angle of the track, we plot the average of CPR charge as a function of $\sin\theta$ in the fixed momentum ranges in Figs. B.1 and B.2. Each of these plot shows that the mean CPR charge increases as the incident angle decrease. The CPR charge increasing rate changes at $\sin\theta=0.81$. These two angle regions

¹CDF off-line routine: `get_soft_electron` is used

with $\sin \theta$ above and below 0.81 correspond to the two different segments. We parameterize this angle dependence by fitting the CPR charge distribution to the two straight lines meeting at $\sin \theta = 0.81$.

$$\langle Q_{CPR}^{raw} \rangle(\theta, p^i) = \begin{cases} A_1(p^i)(\sin \theta - 1) + S(p^i) & (\sin \theta > 0.81) \\ A_2(p^i)(\sin \theta - 1) + c_2(p^i) & (\sin \theta < 0.81) \end{cases} \quad (\text{B.1})$$

where,

$$c_2(p^i) = (0.81 - 1)(A_1(p^i) - A_2(p^i)) + S(p^i) \quad (\text{B.2})$$

The free parameters in the above fit are $S(p^i)$, $A_1(p^i)$ and $A_2(p^i)$. We call $S(p^i)$ a scale parameter since it represents the magnitude of the CPR charge at $\sin \theta = 1$. We call $A_1(p^i)$ and $A_2(p^i)$ angle parameters.

Next, we study the momentum dependence of the scale parameter $S(p^i)$. We plot $S(p^i)$ as a function of momentum in Fig. B.3. This plot is fitted to the power of the momentum;

$$S(p) = 2.8519 \times p^{0.2704} + 0.5359.$$

The first parameterizations (B.1) are divided by this and then multiplied by 10.0 to have a constant CPR charge(=10.0) at $\sin \theta = 1$. New parameters are denoted with the prime(').

We then study the momentum dependence of the angle-parameters A_1' and A_2' . We plot A_1' and A_2' as a function of momentum in Fig. B.4. We fit these distribution to a straight line.

$$A_1(p)' \equiv A_1(p) \frac{10}{S(p)} = -27.486 - 0.254p$$

$$A_2(p)' \equiv A_2(p) \frac{10}{S(p)} = -61.652 - 1.731p$$

Finally, the correction function which removes all momentum and angle dependence is given by;

$$Q_{CPR}^{cor} = 10.0 \times Q_{CPR}^{raw} \times F(p, \theta)$$

where,

$$F(p, \theta)^{-1} = \begin{cases} A_1(p)(\sin\theta - 1) + S(p) & (\sin\theta < 0.81) \\ A_2(p)(\sin\theta - 1) + (0.81 - 1)(A_1(p) - A_2(p)) + S(p) & (\sin\theta > 0.81) \end{cases}$$

where,

$$\begin{aligned} S(p) &= 2.8519 \times p^{0.2704} + 0.5359 \\ A_1(p) &= \frac{S(p)}{10}(-27.486 - 0.254p) \\ A_2(p) &= \frac{S(p)}{10}(-61.652 - 1.731p). \end{aligned}$$

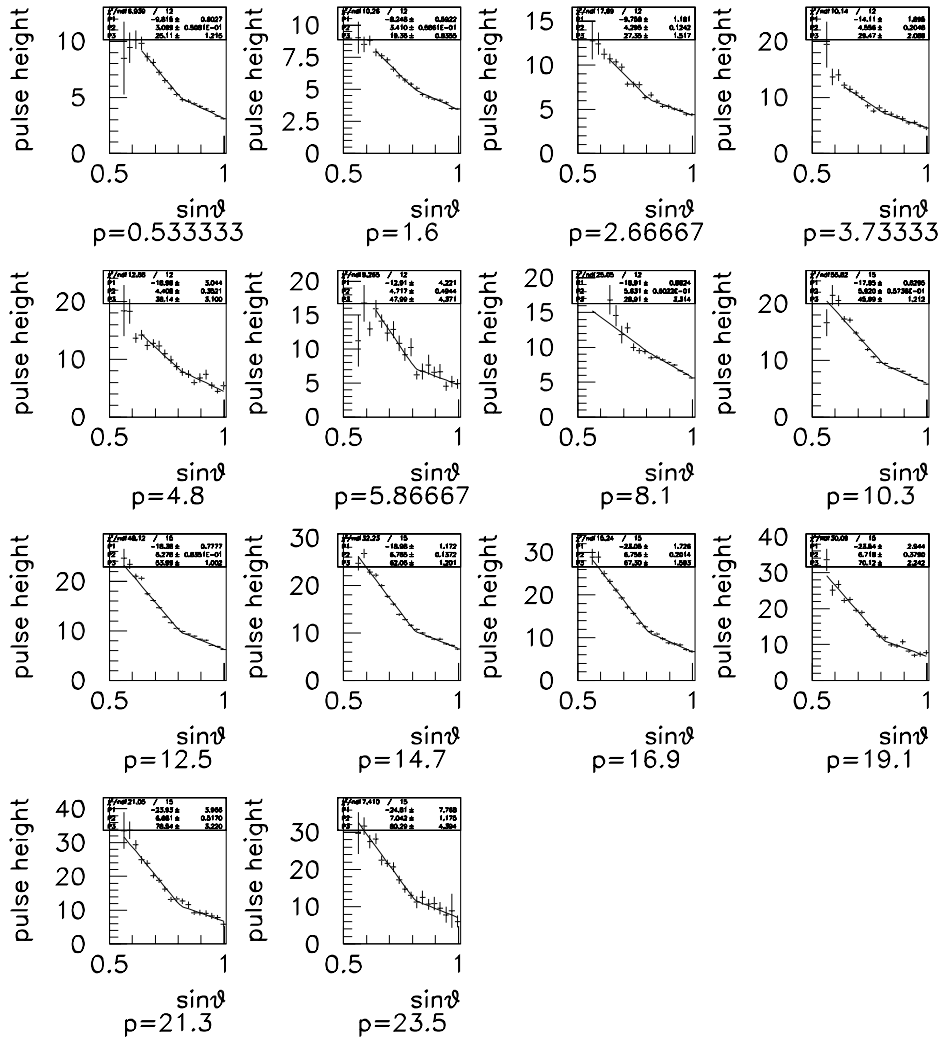


Figure B.1: The mean CPR charge versus incident angle of the electron in the fixed momentum ranges.

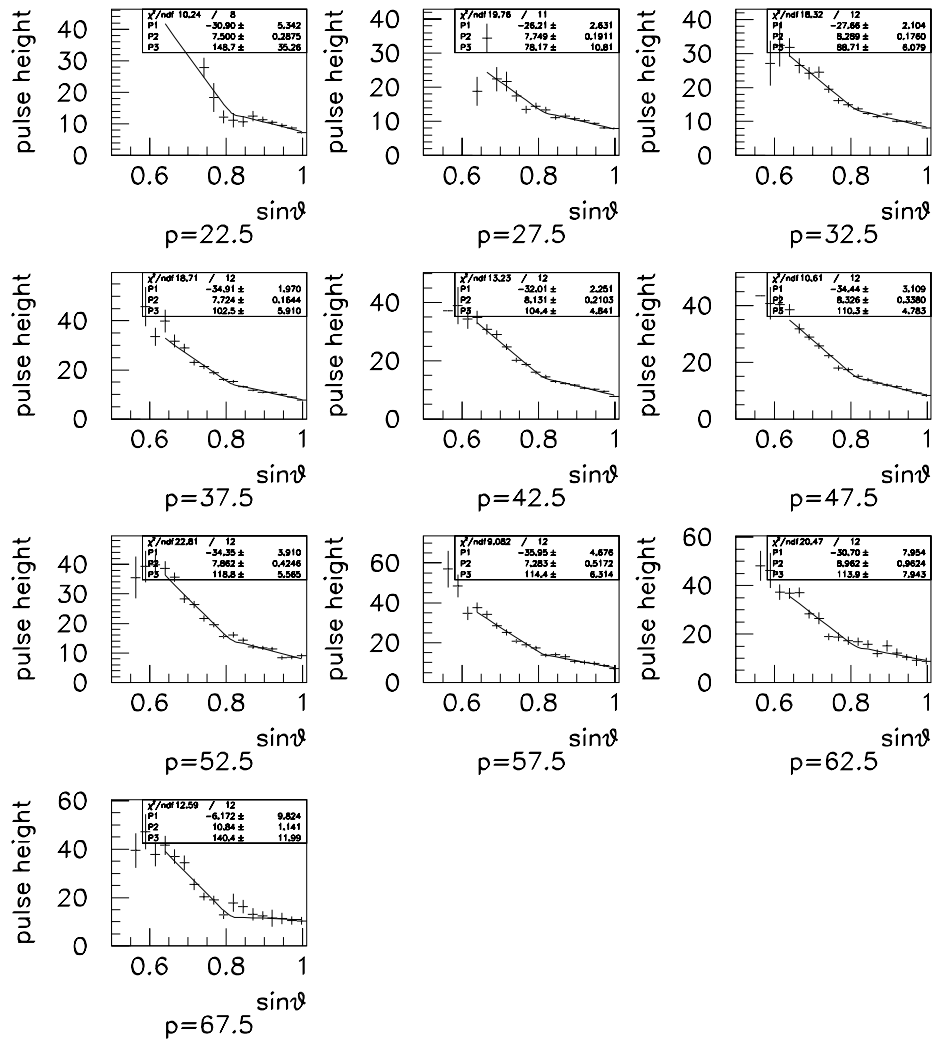


Figure B.2: The mean CPR charge versus incident angle of the electron in the fixed momentum ranges.

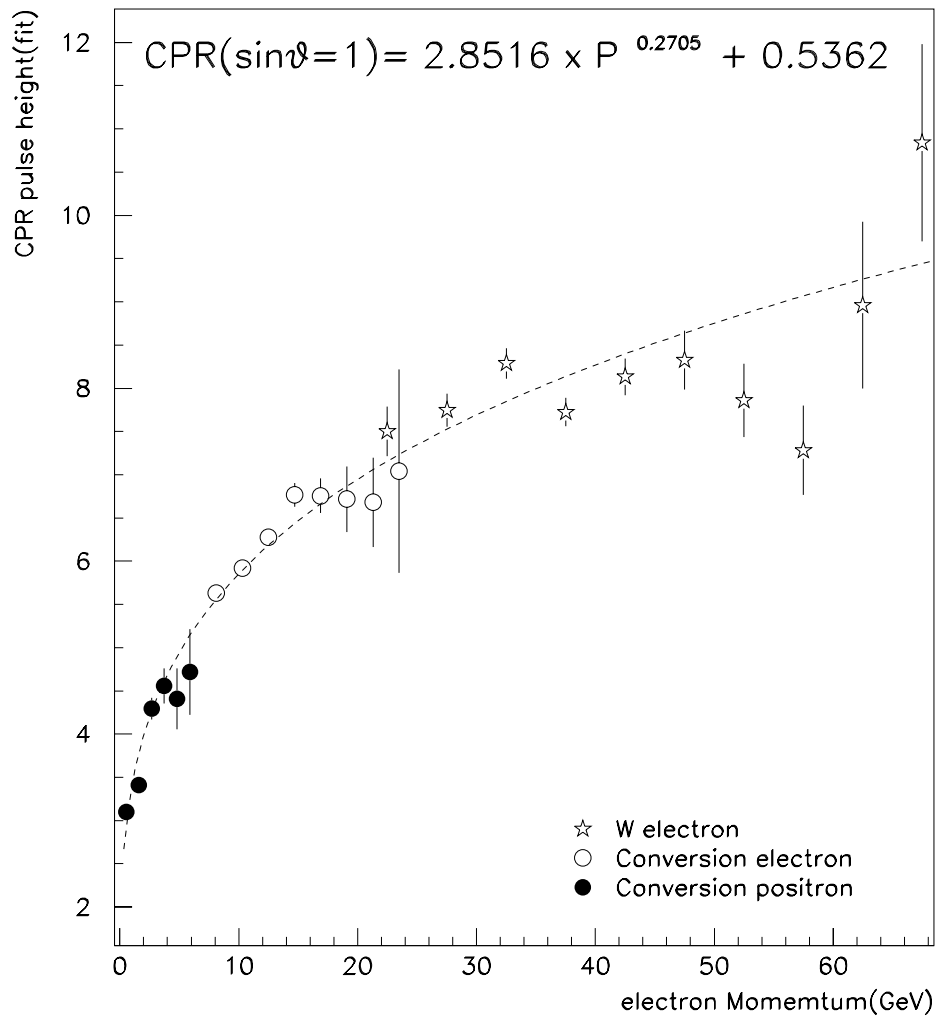


Figure B.3: The mean CPR charge versus electron momentum at $\sin\theta = 1$. The star represents for the W electron, the open circle represents for the conversion electron and the solid circle represents for the partner track of the conversion electron.

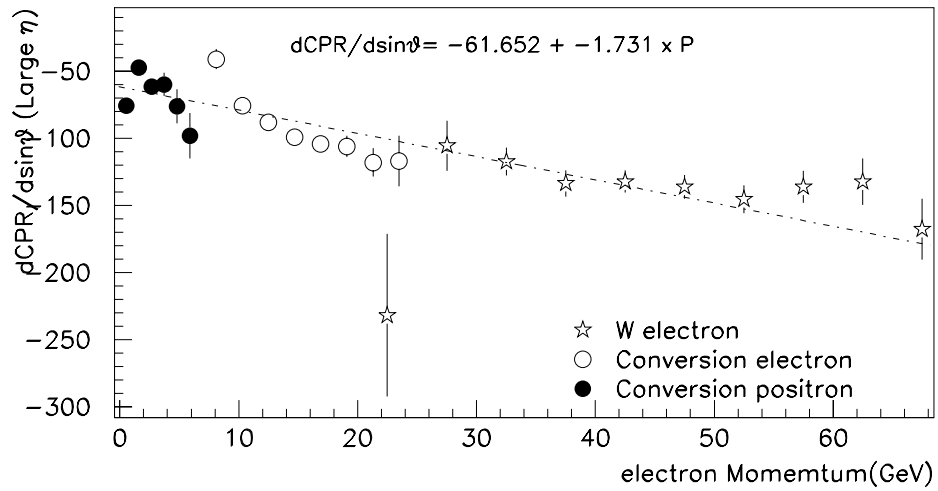
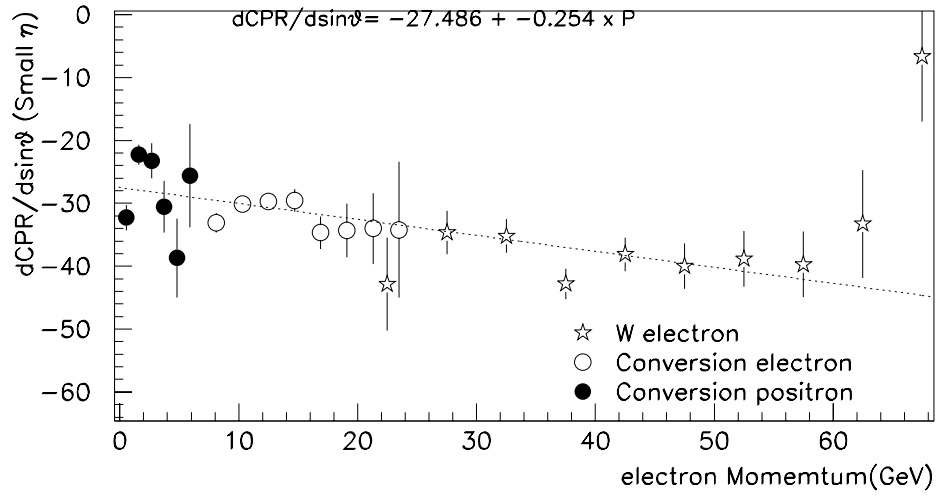


Figure B.4: $d\langle Q_{CPR} \rangle / d\sin\theta$ versus electron momentum. The star represents for the W electron, the open circle represents for the conversion electron and the solid circle represents for the partner track of the conversion electron.

Appendix C

Simulation of the forward calorimeter

We have used an established technique to simulate the detector response against the low p_T particles according to the reference [38]. The simulated energy flow in a FCAL tower is corrected by the following expression,

$$E_i^{mes} = S_i \times p^{gen} + C_i$$

where p^{gen} is a momentum of the particle in the generator-level, S_i and C_i are energy correction factors tuned in the i th η segment of the tower.

We determine the energy correction factors in order to reproduce the energies measured in the real $b\bar{b}$ sample. The selected sample of *electron* + D^0 events [39] are used as the real $b\bar{b}$ data. The D^0 mass peak of the data sets is shown in Fig. C.1. We obtained 1899 D^0 candidates during the same run as we used for the diffractive $b\bar{b}$ analysis. We then look at the exponential slopes of the energy spectra in each η segment of the forward calorimeter. Slopes of energy spectra in the D^0 mass region and the side-bands regions are shown in Fig. C.2. Since no differences are seen in the forward energy spectra between the two regions, we do not need subtract the combinatorial background from the 1899 D^0 candidates. These forward energy spectra, however, the contain contributions of energies from extra minimum bias events aside from a $b\bar{b}$ event vertex. The contribution of those pile-up events can be calculated

using the luminosity of the sample as we described in Sec. 6.1.1. We subtract the contribution of minimum bias spectra using a real data sample which is taken by the clock trigger during RUN1A period. The forward energy spectra purely coming from the $b\bar{b}$ vertex are shown in Fig. C.3.

We then look at the Monte Carlo $b\bar{b}$ sample described in the Sec. 5.1. The trajectories of all generated particles are simulated by the full detector simulation program (CDFSIM) and the energy flow traversing the front plane of the forward calorimeter are recorded. The real tower segmentation are used for the forward calorimeter and the energy flow in each tower are clustered as described in Sec. 3.2. The energy spectrum in each eta segment is shown in Fig. C.4. These Monte Carlo energy spectrum is much harder than the observed one. In order to match this Monte Carlo energy spectra to the observed data, we use a linear correction function as shown in the top of this section.

$$E_i^{mes} = S_i \times p^{gen} + C_i$$

The coefficients S_i and C_i are determined by comparing two spectra, the Monte Carlo and the data. Obtained energy scale factors and offset energies are shown in Fig. C.5. The error in each factors are result of the exponential fits to the energy spectra.

Matching of the forward detector simulation to the data are demonstrated in Fig. C.6 where we apply the single vertex requirement to the data so as to avoid multi-vertex effects. Since we use the energy offset around 1 GeV, our model is valid only for the energies above 1.5 GeV.

The BBC response is also simulated using the real segmentation. Only charged particles are accounted in the simulation. We do not use any energy thresholds for charged particles.

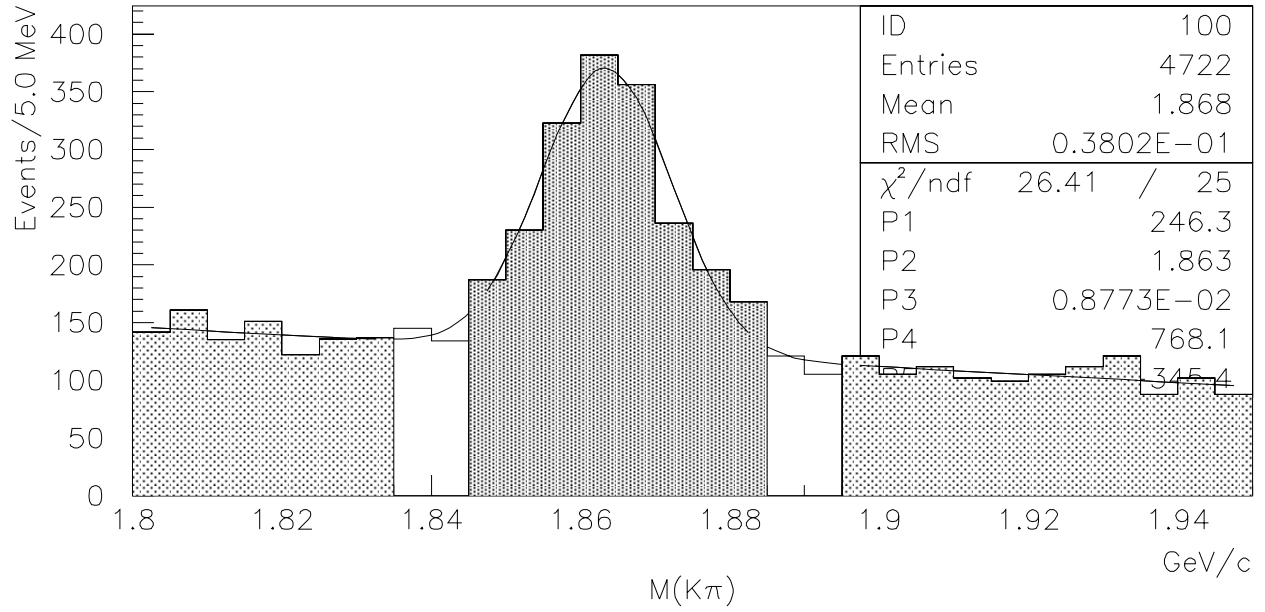


Figure C.1: The invariant mass distribution of $D^0 \rightarrow K\pi$ candidates.

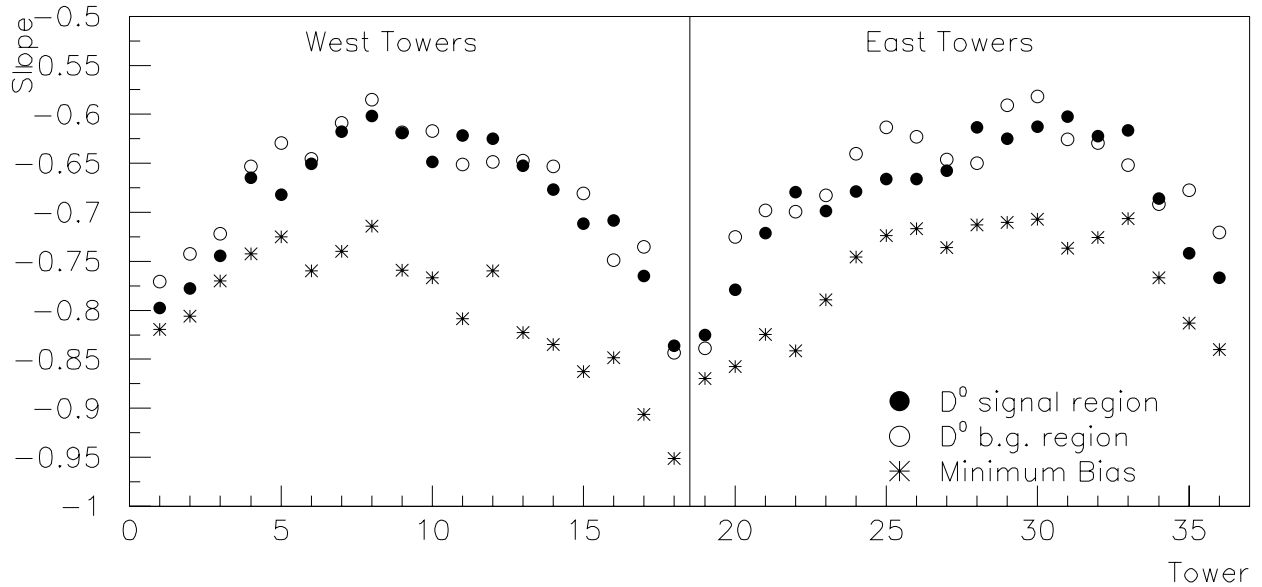


Figure C.2: The exponential slopes of the energy spectrum in each eta segments.

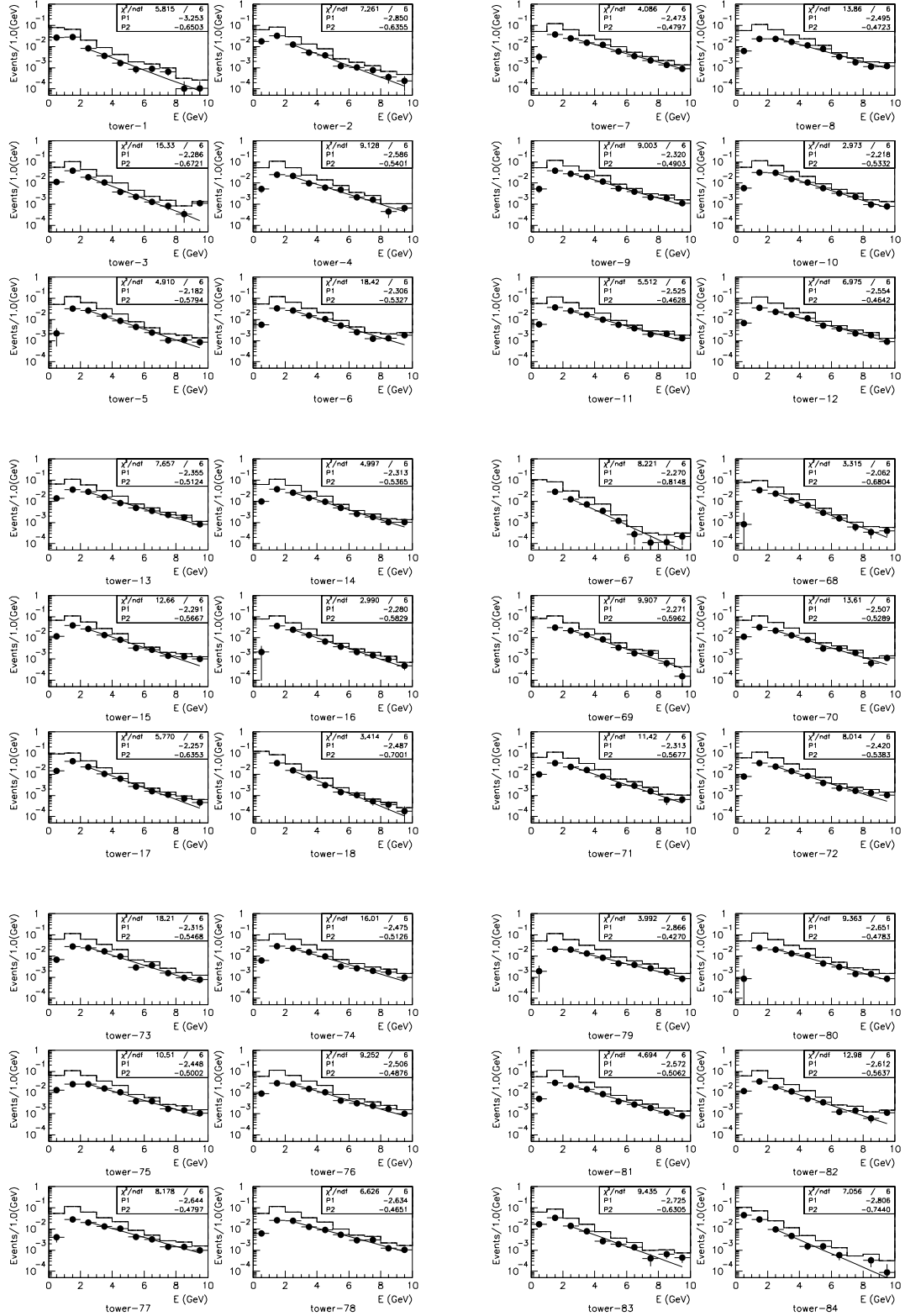


Figure C.3: The energy spectrum in each eta segments for the $e+D^0$ sample. The black circle shows spectra after subtracting Minimum bias contribution.

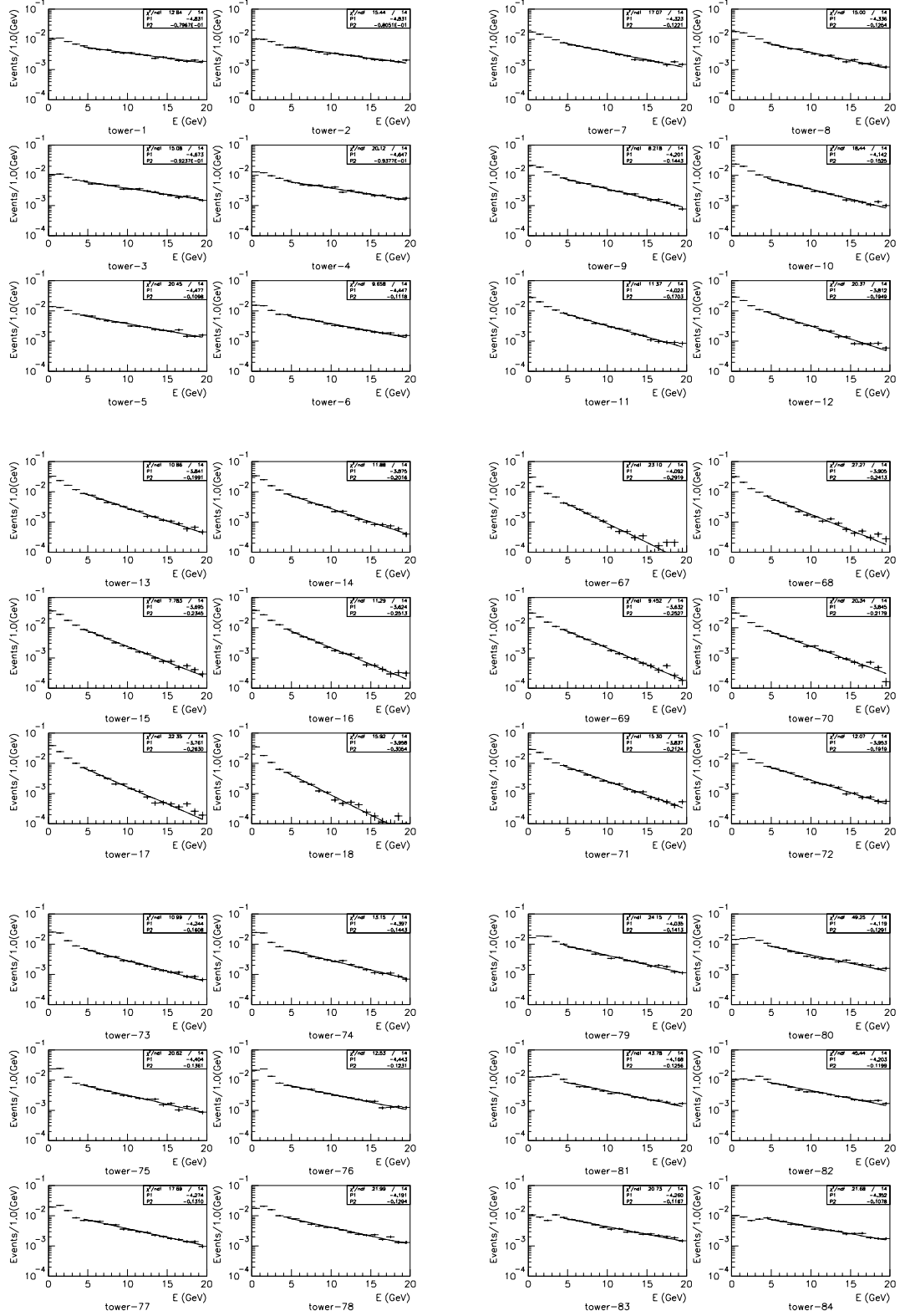
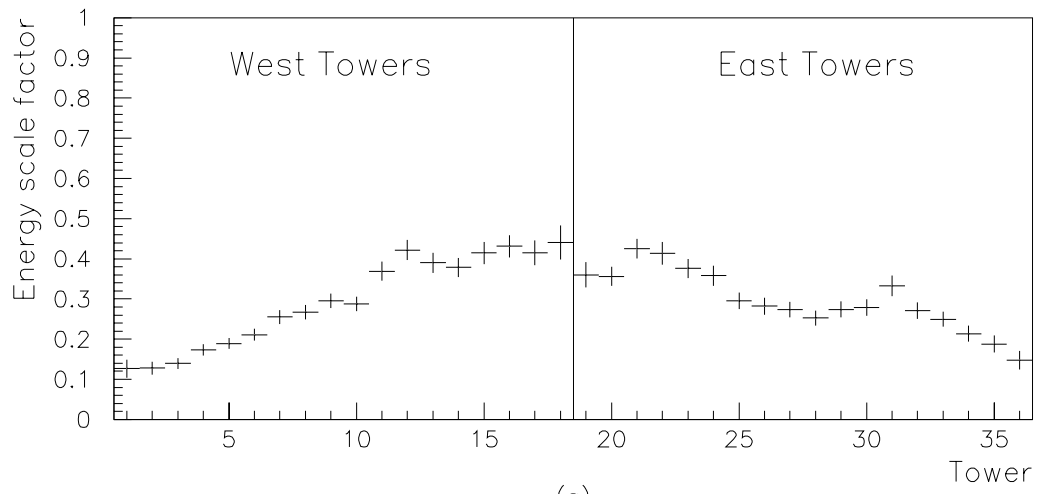
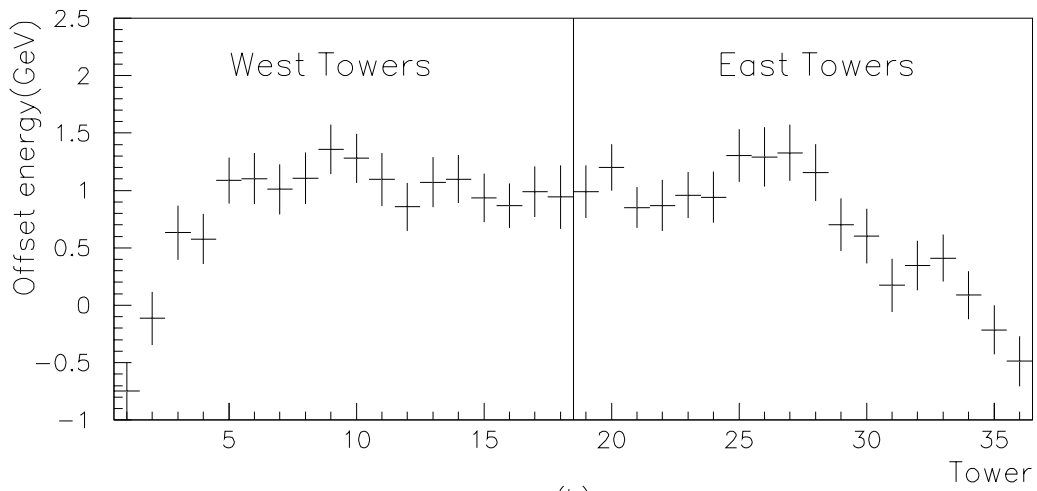


Figure C.4: The energy spectrum in each eta segments for Monte Carlo sample without any energy correction.



(a)



(b)

Figure C.5: The energy correction factors for Monte Carlo generated low p_T particle. (a) the energy scale factors (b) the offset energy factors

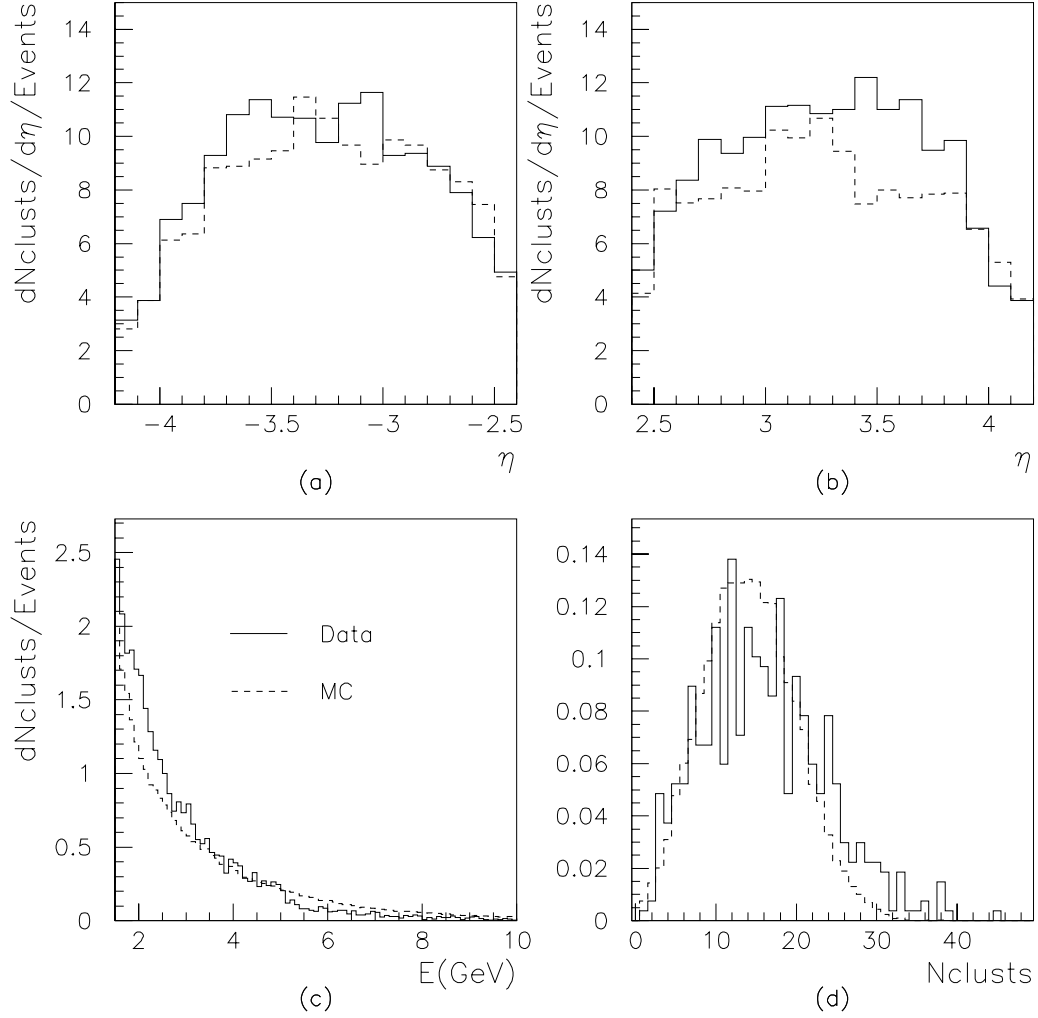


Figure C.6: Simulated response of the forward calorimeter for $b\bar{b}$ events compared to the $e+D^0$ sample with single vertex requirement. (a) the hit tower occupancy in the west calorimeter (b) the hit tower occupancy in the east calorimeter (c) the cluster energy spectrum (d) the number of hit clusters per events

Appendix D

Likelihood function

D.1 Likelihood function for binned fit

$$L = \frac{e^{-\mu} \mu^{N^{obs}}}{N^{obs}!} \times \frac{1}{\sqrt{2\pi}\sigma_{had}} \exp \left[-\frac{1}{2} \left(\frac{n_{had} - N_{had}}{\sigma_{had}} \right)^2 \right] \\ \times \frac{1}{\sqrt{2\pi}\sigma_{con}} \exp \left[-\frac{1}{2} \left(\frac{n_{con} - N_{con}}{\sigma_{con}} \right)^2 \right] \times \prod_{i=1}^m \frac{e^{-\mu_i} \mu_i^{N_i^{obs}}}{N_i^{obs}!}$$

$$\mu = n_{had} + n_{con} + n_{b\bar{b}} + n_{c\bar{c}}$$

$$\mu_i = n_{had} f_i^{had} + n_{con} f_i^{con} + n_{b\bar{b}} f_i^{b\bar{b}} + n_{c\bar{c}} f_i^{c\bar{c}}$$

parameters for fit

n_{had} = number of hadron faking electrons

n_{con} = number of conversions

$n_{b\bar{b}}$ = number of $b\bar{b}$ events

$n_{c\bar{c}}$ = number of $c\bar{c}$ events

Constants

N^{obs} = total number of observed events

N_i^{obs} = number of observed events in the i th bin

N_{had} = number of hadron faking electrons estimated by CPR fit

σ_{had} = error of N_{had}

N_{con} = number of conversions estimated by conversion finding efficiency

σ_{con} = error of N_{con}

Probability functions

f_i^{had} = probability of a hadron having the observable inside i th bin

f_i^{con} = probability of a conversion having the observable inside i th bin

$f_i^{b\bar{b}}$ = probability of c – electron having the observable inside i th bin

$f_i^{c\bar{c}}$ = probability of b – electron having the observable inside i th bin

D.2 Likelihood function for unbinned fit

$$L = \frac{e^{-\mu} \mu^{N^{obs}}}{N^{obs}!} \times \frac{1}{\sqrt{2\pi}\sigma_{had}} \exp \left[-\frac{1}{2} \left(\frac{n_{had} - N_{had}}{\sigma_{had}} \right)^2 \right]$$
$$\times \frac{1}{\sqrt{2\pi}\sigma_{con}} \exp \left[-\frac{1}{2} \left(\frac{n_{con} - N_{con}}{\sigma_{con}} \right)^2 \right]$$
$$\times \prod_{j=1}^k \frac{n_{had} f^{had}(x_j) + n_{con} f^{con}(x_j) + n_{b\bar{b}} f^{b\bar{b}}(x_j) + n_{c\bar{c}} f^{c\bar{c}}(x_j)}{n_{had} + n_{con} + n_{b\bar{b}} + n_{c\bar{c}}}$$
$$\mu = n_{had} + n_{con} + n_{b\bar{b}} + n_{c\bar{c}}$$

parameters for fit

n_{had} = number of hadron faking electron

n_{con} = number of conversions

$n_{b\bar{b}}$ = number of $b\bar{b}$ events

$n_{c\bar{c}}$ = number of $c\bar{c}$ events

Constants

N^{obs} = total number of observed events

N_{had} = number of hadron faking electrons estimated by CPR fit

σ_{had} = error of N_{had}

N_{con} = number of conversions estimated by conversion finding efficiency

σ_{con} = error of N_{con}

Probability functions

$f^{had}(x)$ = probability of a hadron having the observable as x

$f^{con}(x)$ = probability of a conversion having the observable as x

$f^{b\bar{b}}(x)$ = probability of c – electron having the observable as x

$f^{c\bar{c}}(x)$ = probability of b – electron having the observable as x

Appendix E

The CDF Collaboration

F. Abe,¹⁷ H. Akimoto,³⁹ A. Akopian,³¹ M. G. Albrow,⁷ A. Amadon,⁵
S. R. Amendolia,²⁷ D. Amidei,²⁰ J. Antos,³³ S. Aota,³⁷ G. Apollinari,³¹
T. Arisawa,³⁹ T. Asakawa,³⁷ W. Ashmanskas,⁵ M. Atac,⁷ P. Azzi-Bacchetta,²⁵
N. Bacchetta,²⁵ S. Bagdasarov,³¹ M. W. Bailey,²² P. de Barbaro,³⁰
A. Barbaro-Galtieri,¹⁸ V. E. Barnes,²⁹ B. A. Barnett,¹⁵ M. Barone,⁹
G. Bauer,¹⁹ T. Baumann,¹¹ F. Bedeschi,²⁷ S. Behrends,³ S. Belforte,²⁷
G. Bellettini,²⁷ J. Bellinger,⁴⁰ D. Benjamin,³⁵ J. Bensinger,³ A. Beretvas,⁷
J. P. Berge,⁷ J. Berryhill,⁵ S. Bertolucci,⁹ S. Bettelli,²⁷ B. Bevensee,²⁶
A. Bhatti,³¹ K. Biery,⁷ C. Bigongiari,²⁷ M. Binkley,⁷ D. Bisello,²⁵ R. E. Blair,¹
C. Blocker,³ K. Bloom,²⁰ S. Blusk,³⁰ A. Bodek,³⁰ W. Bokhari,²⁶ G. Bolla,²⁹
Y. Bonushkin,⁴ D. Bortoletto,²⁹ J. Boudreau,²⁸ L. Breccia,² C. Bromberg,²¹
N. Bruner,²² R. Brunetti,² E. Buckley-Geer,⁷ H. S. Budd,³⁰ K. Burkett,¹¹
G. Busetto,²⁵ A. Byon-Wagner,⁷ K. L. Byrum,¹ M. Campbell,²⁰ A. Caner,²⁷
W. Carithers,¹⁸ D. Carlsmith,⁴⁰ J. Cassada,³⁰ A. Castro,²⁵ D. Cauz,³⁶
A. Cerri,²⁷ P. S. Chang,³³ P. T. Chang,³³ H. Y. Chao,³³ J. Chapman,²⁰
M. -T. Cheng,³³ M. Chertok,³⁴ G. Chiarelli,²⁷ C. N. Chiou,³³ F. Chlebana,⁷
L. Christofek,¹³ R. Cropp,¹⁴ M. L. Chu,³³ S. Cihangir,⁷ A. G. Clark,¹⁰
M. Cobal,²⁷ E. Cocca,²⁷ M. Contreras,⁵ J. Conway,³² J. Cooper,⁷ M. Cordelli,⁹
D. Costanzo,²⁷ C. Couyoumtzelis,¹⁰ D. Cronin-Hennessy,⁶ R. Culbertson,⁵

D. Dagenhart,³⁸ T. Daniels,¹⁹ F. DeJongh,⁷ S. Dell'Agnello,⁹ M. Dell'Orso,²⁷
 R. Demina,⁷ L. Demortier,³¹ M. Deninno,² P. F. Derwent,⁷ T. Devlin,³²
 J. R. Dittmann,⁶ S. Donati,²⁷ J. Done,³⁴ T. Dorigo,²⁵ N. Eddy,¹³
 K. Einsweiler,¹⁸ J. E. Elias,⁷ R. Ely,¹⁸ E. Engels, Jr.,²⁸ W. Erdmann,⁷
 D. Errede,¹³ S. Errede,¹³ Q. Fan,³⁰ R. G. Feild,⁴¹ Z. Feng,¹⁵ C. Ferretti,²⁷
 I. Fiori,² B. Flaughner,⁷ G. W. Foster,⁷ M. Franklin,¹¹ J. Freeman,⁷
 J. Friedman,¹⁹ H. Frisch,⁵ Y. Fukui,¹⁷ S. Gadomski,¹⁴ S. Galeotti,²⁷
 M. Gallinaro,²⁶ O. Ganel,³⁵ M. Garcia-Sciveres,¹⁸ A. F. Garfinkel,²⁹ C. Gay,⁴¹
 S. Geer,⁷ D. W. Gerdes,²⁰ P. Giannetti,²⁷ N. Giokaris,³¹ P. Giromini,⁹
 G. Giusti,²⁷ M. Gold,²² A. Gordon,¹¹ A. T. Goshaw,⁶ Y. Gotra,²⁸
 K. Goulianos,³¹ H. Grassmann,³⁶ C. Green,²⁹ L. Groer,³² C. Grosso-
 Pilcher,⁵ G. Guillian,²⁰ J. Guimaraes da Costa,¹⁵ R. S. Guo,³³ C. Haber,¹⁸
 E. Hafen,¹⁹ S. R. Hahn,⁷ R. Hamilton,¹¹ T. Handa,¹² R. Handler,⁴⁰
 W. Hao,³⁵ F. Happacher,⁹ K. Hara,³⁷ A. D. Hardman,²⁹ R. M. Harris,⁷
 F. Hartmann,¹⁶ J. Hauser,⁴ E. Hayashi,³⁷ J. Heinrich,²⁶ A. Heiss,¹⁶
 B. Hinrichsen,¹⁴ K. D. Hoffman,²⁹ C. Holck,²⁶ R. Hollebeek,²⁶ L. Holloway,¹³
 Z. Huang,²⁰ B. T. Huffman,²⁸ R. Hughes,²³ J. Huston,²¹ J. Huth,¹¹
 H. Ikeda,³⁷ M. Incagli,²⁷ J. Incandela,⁷ G. Introzzi,²⁷ J. Iwai,³⁹ Y. Iwata,¹²
 E. James,²⁰ H. Jensen,⁷ U. Joshi,⁷ E. Kajfasz,²⁵ H. Kambara,¹⁰ T. Kamon,³⁴
 T. Kaneko,³⁷ K. Karr,³⁸ H. Kasha,⁴¹ Y. Kato,²⁴ T. A. Keaffaber,²⁹
 K. Kelley,¹⁹ R. D. Kennedy,⁷ R. Kephart,⁷ D. Kestenbaum,¹¹ D. Khazins,⁶
 T. Kikuchi,³⁷ M. Kirk,³ B. J. Kim,²⁷ H. S. Kim,¹⁴ S. H. Kim,³⁷ Y. K. Kim,¹⁸
 L. Kirsch,³ S. Klimenko,⁸ D. Knoblauch,¹⁶ P. Koehn,²³ A. Königeter,¹⁶
 K. Kondo,³⁷ J. Konigsberg,⁸ K. Kordas,¹⁴ A. Korytov,⁸ E. Kovacs,¹
 W. Kowald,⁶ J. Kroll,²⁶ M. Kruse,³⁰ S. E. Kuhlmann,¹ E. Kuns,³²
 K. Kurino,¹² T. Kuwabara,³⁷ A. T. Laasanen,²⁹ S. Lami,²⁷ S. Lammel,⁷
 J. I. Lamoureux,³ M. Lancaster,¹⁸ M. Lanzoni,²⁷ G. Latino,²⁷ T. LeCompte,¹
 S. Leone,²⁷ J. D. Lewis,⁷ M. Lindgren,⁴ T. M. Liss,¹³ J. B. Liu,³⁰ Y. C. Liu,³³

N. Lockyer,²⁶ O. Long,²⁶ M. Loreti,²⁵ D. Lucchesi,²⁷ P. Lukens,⁷ S. Lusin,⁴⁰
 J. Lys,¹⁸ K. Maeshima,⁷ P. Maksimovic,¹¹ M. Mangano,²⁷ M. Mariotti,²⁵
 J. P. Marriner,⁷ G. Martignon,²⁵ A. Martin,⁴¹ J. A. J. Matthews,²²
 P. Mazzanti,² K. McFarland,³⁰ P. McIntyre,³⁴ P. Melese,³¹ M. Menguzzato,²⁵
 A. Menzione,²⁷ E. Meschi,²⁷ S. Metzler,²⁶ C. Miao,²⁰ T. Miao,⁷ G. Michail,¹¹
 R. Miller,²¹ H. Minato,³⁷ S. Miscetti,⁹ M. Mishina,¹⁷ S. Miyashita,³⁷
 N. Moggi,²⁷ E. Moore,²² Y. Morita,¹⁷ A. Mukherjee,⁷ T. Muller,¹⁶
 A. Munar,²⁷ P. Murat,²⁷ S. Murgia,²¹ M. Musy,³⁶ H. Nakada,³⁷ T. Nakaya,⁵
 I. Nakano,¹² C. Nelson,⁷ D. Neuberger,¹⁶ C. Newman-Holmes,⁷ C.-
 Y. P. Ngan,¹⁹ H. Niu,³ L. Nodulman,¹ A. Nomerotski,⁸ S. H. Oh,⁶
 T. Ohmoto,¹² T. Ohsugi,¹² R. Oishi,³⁷ M. Okabe,³⁷ T. Okusawa,²⁴
 J. Olsen,⁴⁰ C. Pagliarone,²⁷ R. Paoletti,²⁷ V. Papadimitriou,³⁵ S. P. Pappas,⁴¹
 N. Parashar,²⁷ A. Parri,⁹ D. Partos,³ J. Patrick,⁷ G. Pauletta,³⁶ M. Paulini,¹⁸
 A. Perazzo,²⁷ L. Pescara,²⁵ M. D. Peters,¹⁸ T. J. Phillips,⁶ G. Piacentino,²⁷
 M. Pillai,³⁰ K. T. Pitts,⁷ R. Plunkett,⁷ A. Pompos,²⁹ L. Pondrom,⁴⁰
 J. Proudfoot,¹ F. Ptohos,¹¹ G. Punzi,²⁷ K. Ragan,¹⁴ D. Reher,¹⁸
 M. Reischl,¹⁶ A. Ribon,²⁵ F. Rimondi,² L. Ristori,²⁷ W. J. Robertson,⁶
 A. Robinson,¹⁴ T. Rodrigo,²⁷ S. Rolli,³⁸ L. Rosenson,¹⁹ R. Roser,¹³
 T. Saab,¹⁴ W. K. Sakumoto,³⁰ D. Saltzberg,⁴ A. Sansoni,⁹ L. Santi,³⁶
 H. Sato,³⁷ P. Schlabach,⁷ E. E. Schmidt,⁷ M. P. Schmidt,⁴¹ A. Scott,⁴
 A. Scribano,²⁷ S. Segler,⁷ S. Seidel,²² Y. Seiya,³⁷ F. Semeria,² T. Shah,¹⁹
 M. D. Shapiro,¹⁸ N. M. Shaw,²⁹ P. F. Shepard,²⁸ T. Shibayama,³⁷
 M. Shimojima,³⁷ M. Shochet,⁵ J. Siegrist,¹⁸ A. Sill,³⁵ P. Sinervo,¹⁴
 P. Singh,¹³ K. Sliwa,³⁸ C. Smith,¹⁵ F. D. Snider,¹⁵ J. Spalding,⁷
 T. Speer,¹⁰ P. Sphicas,¹⁹ F. Spinella,²⁷ M. Spiropulu,¹¹ L. Spiegel,⁷
 L. Stanco,²⁵ J. Steele,⁴⁰ A. Stefanini,²⁷ R. Ströhmer,^{7a} J. Strologas,¹³
 F. Strumia,¹⁰ D. Stuart,⁷ K. Sumorok,¹⁹ J. Suzuki,³⁷ T. Suzuki,³⁷
 T. Takahashi,²⁴ T. Takano,²⁴ R. Takashima,¹² K. Takikawa,³⁷ M. Tanaka,³⁷

B. Tannenbaum,⁴ F. Tartarelli,²⁷ W. Taylor,¹⁴ M. Tecchio,²⁰ P. K. Teng,³³
 Y. Teramoto,²⁴ K. Terashi,³⁷ S. Tether,¹⁹ D. Theriot,⁷ T. L. Thomas,²²
 R. Thurman-Keup,¹ M. Timko,³⁸ P. Tipton,³⁰ A. Titov,³¹ S. Tkaczyk,⁷
 D. Toback,⁵ K. Tollefson,³⁰ A. Tollestrup,⁷ H. Toyoda,²⁴ W. Trischuk,¹⁴
 J. F. de Troconiz,¹¹ S. Truitt,²⁰ J. Tseng,¹⁹ N. Turini,²⁷ T. Uchida,³⁷
 F. Ukegawa,²⁶ J. Valls,³² S. C. van den Brink,¹⁵ S. Vejcik, III,²⁰ G. Velev,²⁷
 I. Volobouev,¹⁸ R. Vidal,⁷ R. Vilar,^{7a} D. Vucinic,¹⁹ R. G. Wagner,¹
 R. L. Wagner,⁷ J. Wahl,⁵ N. B. Wallace,²⁷ A. M. Walsh,³² C. Wang,⁶
 C. H. Wang,³³ M. J. Wang,³³ A. Warburton,¹⁴ T. Watanabe,³⁷ T. Watts,³²
 R. Webb,³⁴ C. Wei,⁶ H. Wenzel,¹⁶ W. C. Wester, III,⁷ A. B. Wicklund,¹
 E. Wicklund,⁷ R. Wilkinson,²⁶ H. H. Williams,²⁶ P. Wilson,⁷ B. L. Winer,²³
 D. Winn,²⁰ D. Wolinski,²⁰ J. Wolinski,²¹ S. Worm,²² X. Wu,¹⁰ J. Wyss,²⁷
 A. Yagil,⁷ W. Yao,¹⁸ K. Yasuoka,³⁷ G. P. Yeh,⁷ P. Yeh,³³ J. Yoh,⁷ C. Yosef,²¹
 T. Yoshida,²⁴ I. Yu,⁷ A. Zanetti,³⁶ F. Zetti,²⁷ and S. Zucchelli²

(CDF Collaboration)

¹ *Argonne National Laboratory, Argonne, Illinois 60439*

² *Istituto Nazionale di Fisica Nucleare, University of Bologna, I-40127 Bologna, Italy*

³ *Brandeis University, Waltham, Massachusetts 02254*

⁴ *University of California at Los Angeles, Los Angeles, California 90024*

⁵ *University of Chicago, Chicago, Illinois 60637*

⁶ *Duke University, Durham, North Carolina 27708*

⁷ *Fermi National Accelerator Laboratory, Batavia, Illinois 60510*

⁸ *University of Florida, Gainesville, Florida 32611*

⁹ *Laboratori Nazionali di Frascati, Istituto Nazionale di Fisica Nucleare, I-00044 Frascati, Italy*

¹⁰ *University of Geneva, CH-1211 Geneva 4, Switzerland*

¹¹ *Harvard University, Cambridge, Massachusetts 02138*

¹² *Hiroshima University, Higashi-Hiroshima 724, Japan*

- ¹³ *University of Illinois, Urbana, Illinois 61801*
- ¹⁴ *Institute of Particle Physics, McGill University, Montreal H3A 2T8, and University of Toronto,
Toronto M5S 1A7, Canada*
- ¹⁵ *The Johns Hopkins University, Baltimore, Maryland 21218*
- ¹⁶ *Institut für Experimentelle Kernphysik, Universität Karlsruhe, 76128 Karlsruhe, Germany*
- ¹⁷ *National Laboratory for High Energy Physics (KEK), Tsukuba, Ibaraki 305, Japan*
- ¹⁸ *Ernest Orlando Lawrence Berkeley National Laboratory, Berkeley, California 94720*
- ¹⁹ *Massachusetts Institute of Technology, Cambridge, Massachusetts 02139*
- ²⁰ *University of Michigan, Ann Arbor, Michigan 48109*
- ²¹ *Michigan State University, East Lansing, Michigan 48824*
- ²² *University of New Mexico, Albuquerque, New Mexico 87131*
- ²³ *The Ohio State University, Columbus, Ohio 43210*
- ²⁴ *Osaka City University, Osaka 588, Japan*
- ²⁵ *Universita di Padova, Istituto Nazionale di Fisica Nucleare, Sezione di Padova, I-35131 Padova,
Italy*
- ²⁶ *University of Pennsylvania, Philadelphia, Pennsylvania 19104*
- ²⁷ *Istituto Nazionale di Fisica Nucleare, University and Scuola Normale Superiore of Pisa, I-56100
Pisa, Italy*
- ²⁸ *University of Pittsburgh, Pittsburgh, Pennsylvania 15260*
- ²⁹ *Purdue University, West Lafayette, Indiana 47907*
- ³⁰ *University of Rochester, Rochester, New York 14627*
- ³¹ *Rockefeller University, New York, New York 10021*
- ³² *Rutgers University, Piscataway, New Jersey 08855*
- ³³ *Academia Sinica, Taipei, Taiwan 11530, Republic of China*
- ³⁴ *Texas A&M University, College Station, Texas 77843*
- ³⁵ *Texas Tech University, Lubbock, Texas 79409*
- ³⁶ *Istituto Nazionale di Fisica Nucleare, University of Trieste/ Udine, Italy*
- ³⁷ *University of Tsukuba, Tsukuba, Ibaraki 305, Japan*

³⁸ *Tufts University, Medford, Massachusetts 02155*

³⁹ *Waseda University, Tokyo 169, Japan*

⁴⁰ *University of Wisconsin, Madison, Wisconsin 53706*

⁴¹ *Yale University, New Haven, Connecticut 06520*

Bibliography

- [1] K. Goulianos, Phys. Rep. **101** (1983) 169.
- [2] P.D.B Collins “An introduction to Regge theory and high energy physics” Cambridge University Press (1977).
- [3] J.R.Forshaw, D.A. Ross, “Quantum chromodynamics and the pomeron” Cambridge University Press (1997).
- [4] G. Ingelman and P.Schlein, Phys. Lett. **B152** (1985) 256.
- [5] R.Bonino *et al.* (UA8), Phys.Lett.**B211** (1988) 239.
- [6] R.Brandt *et al.* (UA8), Phys.Lett.**B297** (1992) 417.
- [7] C. Adloff *et al.*, H1 Collab., *Zeit. Phys.* **C76** (1997) 613.
- [8] j. Breitweg *et al.*, ZEUS Collab., *Europ. Phys. J.* **C6** (1998) 43-66.
- [9] R.Brock *et al.*, CTEQ Collab., Rev. Mod. Phys. 67 (1995) 157.
- [10] F. Abe *et al.*, CDF Collab., Phys. Rev. Lett. **79** (1997) 2636.
- [11] F. Abe *et al.*, CDF Collab., Phys. Rev. Lett. **78** (1997) 2698. Suren Bagdasarov, PhD Thesis, The Rockefeller University, (1997).
- [12] H. Fritzsche, K. H. Streng, Phys. Lett. **B164** (1997) 391.
- [13] Klaus Wacker, “Diffractive heavy flavor production in UA1” Proceedings of the 7th Topical workshop on proton-antiproton collider physics,

Edited by Rajendran Raja, Alvin Tollestrup, John Yoh, World Scientific, (1989).

K. Eggert, "Search for diffractive heavy flavor production at the CERN proton-antiproton-collider" Proceedings of the 2nd International Conference on Elastic and Diffractive Scattering, Rockefeller University, New York (1987).

- [14] A. Donnachie, P.V.Landshoff, *Phys. Lett.* **B296** (1992) 227.
- [15] CDF Collaboration, F. Abe *et al.*, Nucl. Instrum. Methods Phys. Res. A **271** (1988) 387.
- [16] Hans Wenzel, *CDF internal note*,
CDF/DOC/SEC_VTX/CDFR/1790 (1992).
- [17] D. Ameidei *et al.*, Nucl. Instrum. Methods. Phys. Res. A **350** (1994) 73.
- [18] P. Azzi *et al.*, Nucl. Instrum. Methods. Phys. Res. A **360** (1995) 137.
- [19] F. Bedeschi *et al.*, Nucl. Instrum. Methods. Phys. Res. A **268** (1988) 50.
- [20] L. Balka *et al.*, Nucl. Instrum. Methods. Phys. Res. A **267** (1988) 272.
- [21] S. BERTOLUCCI *et al.*, Nucl. Instrum. Methods. Phys. Res. A **267** (1988) 301.
- [22] G. Brandenburg *et al.*, Nucl. Instrum. Methods. Phys. Res. A **267** (1988) 257.
- [23] David Brown, *CDF internal Note*,
CDF/ANAL/CALORIMETRY/GROUP/0713 (1988).
- [24] S. Cihangir *et al.*, Nucl. Instrum. Methods. Phys. Res. A **267** (1988) 249.

- [25] D. Ameidei *et al.*, Nucl. Instrum. Methods. Phys. Res. A **269** (1988) 51.
- [26] G. Drake *et al.*, Nucl. Instrum. Methods. Phys. Res. A **269** (1988) 68.
- [27] G. W. Foster *et al.*, Nucl. Instrum. Methods. Phys. Res. A **269** (1988) 93.
- [28] K. Byrum, *et al.*, *CDF internal Note*,
CDF/PUB/TRIGGER/PUBLIC/2795 (1988).
K. Byrum, *et al.*, Nucl. Instrum. Methods. Phys. Res. A **364** (1995) 144.
- [29] R. E. Blair, J. Proudfoot and A. B. Wicklund, *CDF internal Note*,
CDF/PUB/TRIGGER/PUBLIC/634 (1988).
J. Proudfoot, in *Calorimetry for the Superconducting Supercollider*, proceedings, Alabama, 1989, edited by R. Donaldson and M. Gilchrese (World Scientific, Singapore, 1989).
- [30] R. Mattingly, P. Sphicas, *CDF internal Note*,
CDF/ANAL/BOTTOM/CDFR/2190 (1988).
K. Byrum, *et al.*, Nucl. Instrum. Methods.
Phys. Res. A **364** (1995) 144.
- [31] Paris Sphicas, Dejan Vucinic, *CDF internal note*,
CDF/ANAL/BOTTOM/CDFR/4097 (1997).
- [32] Paul Avery, Ken Read, Garry Trahern, *CLEO Software Note CSN-212*
“QQ:A Monte Carlo Generator” (1985).
Jonathan Lewis, Paul Avery, *CDF internal note*,
CDF/DOC/MONTECARLO/PUBLIC/2724 (1994).
- [33] M. Paulini, M.D. Peters, M.D. Shapiro, I.J. Kroll, O. Long, *CDF internal note*,
CDF/ANAL/BOTTOM/CDFR/3757 (1996).

- [34] The ALEPH Collaboration Phys.Lett.**B369** (1996) 151-162.
- [35] Daniel P. Cronin-Hennessy, Andy Beretvas, Sam Segler *CDF internal note*,
CDF/DOC/CDFR/4317 (1997).
- [36] P.Bruni, A.Edin and G.Ingelman
"POMPYT version 2.6 - A Monte Carlo to Simulate Diffractive Hard Scattering Processes ", DRAFT, DESY, (1996)
<http://www3.tsl.uu.se/theop/pompyt/>.
- [37] E.Eichten, I.Hinchliffe, K.Lane and C.Quigg, Rev.Mod.Phys.**56** (1984) 579.
- [38] S. Bagdasarov and K. Goulios, *CDF internal note*,
CDF/ANAL/JET/CDFR/4564 (1998).
- [39] F. DeJongh, *CDF internal note*,
CDF/ANAL/BOTTOM/CDFR/2935 (1995).
- [40] Stefano Belforte, Paul Derwent, Jhn Marriner, Carla Grosso-Pilcher,
CDF internal note,
CDF/PHYS/CDF/CDFR/2535 (1994).
- [41] M.Derrick *et al.*, ZEUS Collab., Phys.Lett.**B356** (1995) 129.
- [42] K. Goulios, Phys. Lett. **B358** (1995) 379.
- [43] K. Goulios, the talk at DIS'97, hep-ph/9708217 (1997).